Type Ia Supernovae: Rates and Progenitors

by

Epson Thiago Masikiv Heringer
B.Sc., University of São Paulo, 2012

A Thesis Submitted in Partial Fulfillment of the
Requirements for the Degree of

MASTER OF SCIENCE

in the Department of Physics & Astronomy

Type Ia Supernovae: Rates and Progenitors

by

Epson Thiago Masikiv Heringer
B.Sc., University of São Paulo, 2012

Supervisory Committee

Dr. Chris Pritchet, Supervisor
(Department of Physics & Astronomy)

Dr. Falk Herwig, Departmental Member
(Department of Physics & Astronomy)

Supervisory Committee

_____

Dr. Chris Pritchet, Supervisor
(Department of Physics & Astronomy)

_____

Dr. Falk Herwig, Departmental Member
(Department of Physics & Astronomy)

ABSTRACT

Thermonuclear (Type Ia) supernovae are excellent distance indicators, due to their uniform peak brightness. They are also important contributors to the chemical evolution of galaxies since their explosions supply large amounts of iron peak elements to the interstellar medium. However, there is no consensus on the progenitor systems of these supernovae. As a result, different delay times from the formation of the binary system to the supernova have been proposed. Whether the observed rate of supernova Type Ia in early-type galaxies supports a progenitor channel with one or two degenerate objects has been disputed. While the predominant old population found in early-type galaxies supports longer delay times, the presence of recent star formation might indicate the opposite. In this work, we employ a double-burst model to account for the relative contribution of both populations. We show that for a DTD $\propto t^{-1}$, convolved with star formation histories that are relevant for early-type galaxies, the supernova rate is independent of a host galaxy's colour. Our results indicate that a DTD with no cutoff is preferred, thus favoring the double-degenerate scenario.

Contents

List of Tables

List of Figures

Acknowledgements

I would like to thank:

My mother, Rose, my father, Edson, and brother, Rodson, who provide me unconditional love. The fruits of this work is also theirs.

My friends, who helped me to become the person I am today.

My supervisor, for providing me the opportunity to research fascinating explosions.

Dedication

To my family and friends, who have shared both the hardship and joy that came across my journey.

"We fear death, we shudder at life's instability, we grieve to see the flowers wilt again and again, and the leaves fall, and in our hearts we know that we, too, are transitory and will soon disappear. When artists create pictures and thinkers search for laws and formulate thoughts, it is in order to salvage something from the great dance of death, to make something last longer than we do." - Hermann Hesse - from *Narcissus and Goldmund.*

Chapter 1

Introduction

1.1 Overview

Supernovae (SNe) are violent explosions that can outshine an entire galaxy. They are the end point of the life of particular stars and they contribute to the chemical evolution of their host galaxies. In the past, the observation of these transient objects helped to deconstruct the once prevailing idea of a static, immutable universe. In the years 1572 and 1604, our own galaxy hosted supernovae that were investigated by and named after Tycho Brahe and Johannes Kepler, respectively. These two events were visible to the naked eye and were among the brightest objects in the sky at peak luminosity. Coincidentally, both events belong to the same class of supernovae, Type Ia; this class of supernovae is used in modern astronomy to probe the accelerated expansion of the universe, further corroborating the changing nature of the cosmos.

Supernovae are classified according to their spectra and can be subdivided in two major groups: the first group (core-collapse objects) includes supernovae of types II, Ib and Ic, whose spectra lack Si lines, but usually show H or He lines. The second group (thermonuclear explosions) covers the supernovae of type Ia, which lack H and He lines, but present strong Si and Fe lines. A classification scheme is provided in Fig. 1.1, from Turatto (2003), and representative spectra of these types of supernovae are given in Fig. 1.2, from Filippenko (1997).

1.1.1 Core-Collapse Supernova

Each SN group is associated with an explosion mechanism. SNe type II, Ib and Ic are thought to originate from the core-collapse of massive stars ($M \gtrsim 8M_\odot$; Heger et al.
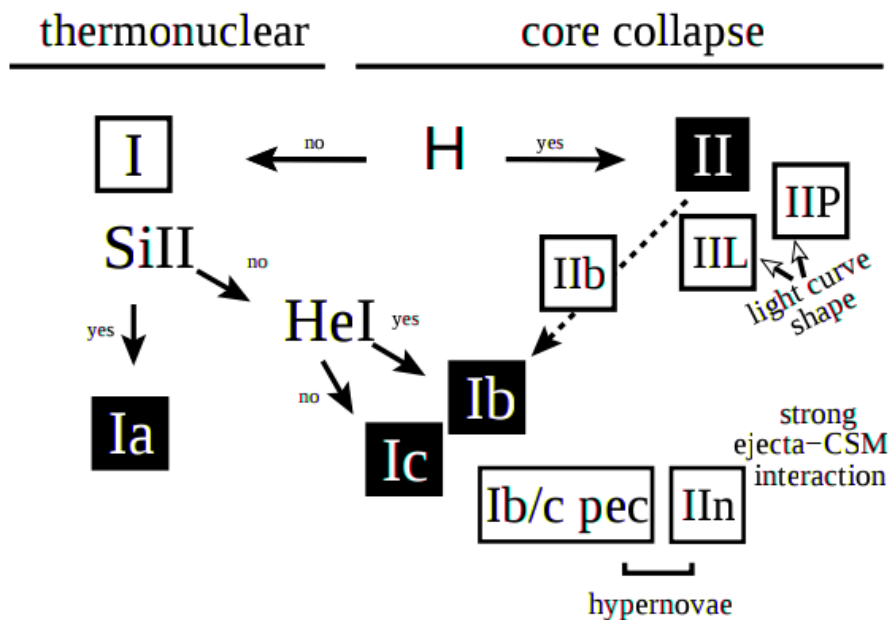
Figure 1.1 Supernova classification scheme from Turatto (2003).
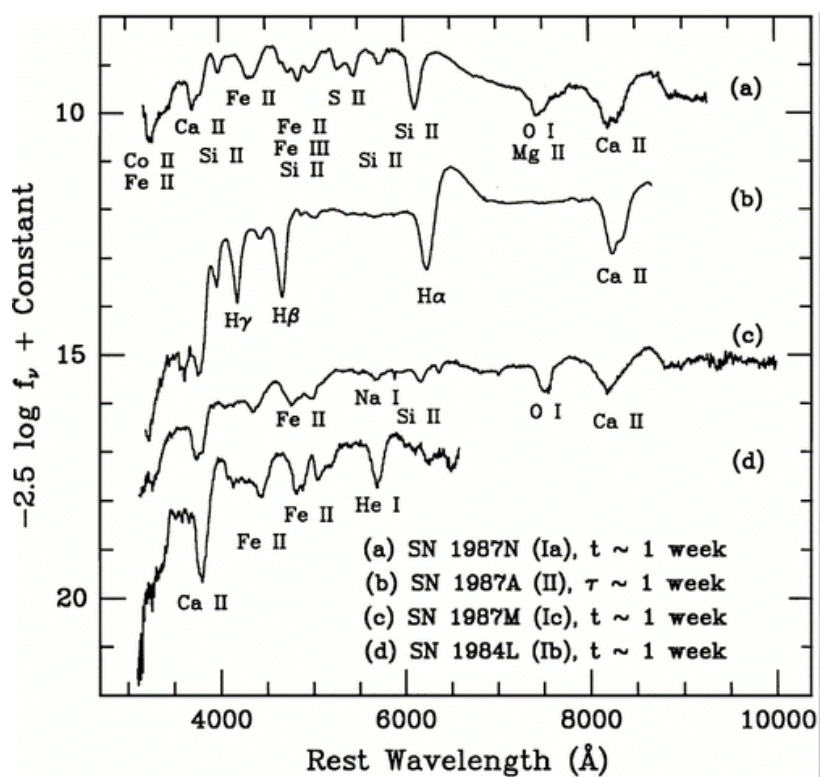
Figure 1.2 Representative spectra of diverse types of supernovae. From Filippenko (1997).

2003). The presence (type II) or lack (types Ib, Ic) of H and He lines in a core-collapse SN spectrum is determined by how much of the outer hydrogen and helium envelopes were stripped off or ejected prior to the explosion (Weiler & Sramek, 1988; Filippenko, 1997).

Massive stars undergo nuclear burning to form elements as heavy as iron, after which nuclear fusion reactions cease, since it is energetically unfavorable to form heavier elements. At this point, the star no longer has the pressure necessary to counterbalance its self-gravity, and a contraction phase starts, ultimately causing the temperature in the core to increase, and the previously formed iron to dissociate into protons and neutrons. Electron capture reactions transform the protons into even more neutrons.

The contraction of the star accelerates into free-fall collapse that stops only when the core's density increases enough for the strong force interaction between neutrons to become relevant; this causes the over-compressed core to bounce back and generate an outward shock-wave. This shock-wave is not energetic enough on its own to cause the supernova. The most accepted theory proposes that the energy necessary to drive an explosion would come from a small fraction, $\sim 1\%$, of the binding energy of the compacted core (typically $\sim \times 10^{46}$ J). This energy is in the form of neutrinos, which transfer their energy to the shock-wave and cause the disruption of the outer layers of the star. The core survives as either a neutron star or black hole (Podsiadlowski, 2013).

1.1.2   Thermonuclear Supernova

The core-collapse mechanism is ruled out as an explanation of SNe of type Ia due to the presence of strong Si lines (which also differentiate this type from type Ic), and, more importantly, the lack of H and He in the spectra. This suggests that the progenitor star was a carbon-oxygen (CO) white dwarf (WD), which is the final evolutionary phase of intermediate and low mass stars (Hoyle & Fowler, 1960). Further circumstantial evidence that SNe Ia are the result of the explosion of CO-WD's is provided by the energy output of burning C and O up to Fe-peak elements. The energy release matches that seen in SNe Ia; furthermore the observed shape of the light curves is in agreement with that expected from the radioactive decay of the Fe-peak elements (Bloom et al., 2012). Direct evidence based on the early observation of SN 2011fe, at a distance of 6.4 Mpc, indicates that the radius of the progenitor

was $\lesssim 0.1 R_\odot$, consistent with a WD radius (Nugent et al., 2011; Bloom et al., 2012).

White Dwarfs are the cores of stars that have burned all of their H and He, but are not massive enough to have synthesized elements heavier than C and O (or in more massive cases O and Ne). The self-gravity of a white dwarf is opposed by electron degeneracy pressure; an isolated WD will simply cool through thermal radiation as time progresses.

In order for a WD to explode, it is necessary to increase its mass to a critical limit, after which the degeneracy pressure can no longer counterbalance gravity. Upon reaching the critical mass, the WD starts to contract, the temperature rises and C burning is ignited. Because the WD is in a degenerate regime, this leads to a runaway process that causes the supernova to explode, leaving no remnant[1].

The critical mass is thought to be the Chandrasekhar mass ($\sim$1.37 $M_\odot$; Chandrasekhar 1931), which is the maximum mass of a (non-rotating) star supported by degenerate electron pressure. However, sub-Chandrasekhar models have also been proposed (e.g. van Kerkwijk et al. 2010, Fink et al. 2010).

Similar to a core-collapse supernova, the total energy released in the ejecta is $\sim 10^{44}$ J, which comes from the burning of C and O into heavier elements. The inner parts of the WD ($\sim$0.6-0.7 $M_\odot$) are expected to completely burn up to iron peak elements, mainly ^{56}Ni, while the outer layers are burnt into intermediate mass elements, such as ^{28}Si and ^{32}S (Maoz et al., 2014; Podsiadlowski, 2013).

The shape of the light curve of a SN Ia (see Fig. 1.3) can be explained by two competing factors: the opacity of the ejecta and the input of radiation energy. The radiation energy is powered by radioactive decay of ^{56}Ni and ^{56}Co to ^{56}Fe with an exponentially declining rate. At first, the radiation energy is trapped in the optically thick ejecta. This regime is characterized by an increase in brightness; it lasts $\sim$ 19 days. The peak brightness occurs when the optical depth of the ejecta has decreased enough to allow the produced photons to be radiated. The light curve dims after this stage because the number of photons produced is quickly declining due to radioactive decay. There is, however, a large amount of energy still trapped in the ejecta at the time of peak brightness, t_{peak}. Therefore, the luminosity of the light curve exceeds the energy input from radioactive decay for a period after t_{peak}. In the final regime, after the excess energy has escaped, the observed luminosity follows the input energy, now primarily provided by the decay of ^{56}Co to ^{56}Fe (Pinto & Eastman, 1996).

---

[1]However it is common usage to also refer to the expanding cloud of gas left after the explosion as a SN Ia "remnant".
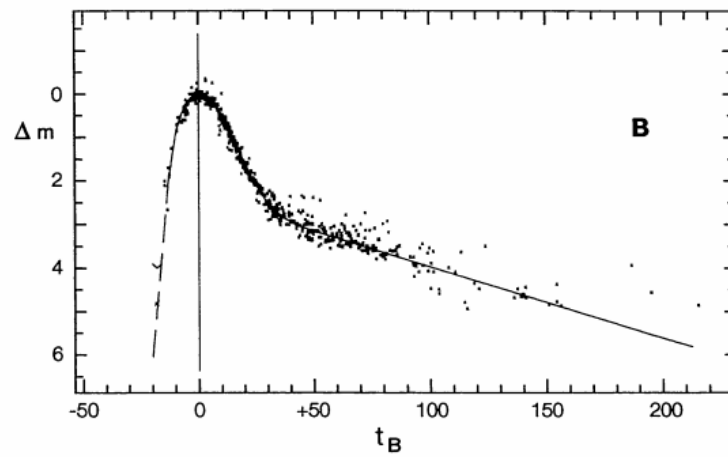
Figure 1.3 Representative light curve of supernovae type Ia in the B band, from Branch & Tammann (1992) (adapted from Cadonau 1986). Both the brightness, Δm, and the time t_B in days, are shifted and plotted with respect to the peak brightness. The data points are based on observations of 22 SNe.

Although the picture of a WD that reaches a critical mass limit and explodes as a result of a runaway thermonuclear process is well accepted in the literature, there are important problems that remain unresolved. First, to reach the critical mass, the WD is expected to accrete from (or merge with) a companion, whose nature is still in doubt. The two most accepted scenarios (channels) are: *(i)* the companion is another CO WD star. The binary system loses angular momentum via gravitational waves and a merger follows. The combined mass surpasses the critical mass. This scenario is known as double degenerate (DD), because of the requirement of two degenerate stars (Tutukov & Yungelson, 1981). *(ii)* The companion is a main sequence star, subgiant, or red giant; it transfers mass to the WD via Roche-lobe accretion. The fresh accreted material (H/He) is burned on the surface of the WD, steadily increasing the net CO mass, until it reaches the critical mass. This scenario is referred as single degenerate (SD), since only one degenerate object is needed (Whelan & Iben, 1973).

Second, simulations of SNe Ia can only produce the observed abundance of elements if the explosion is finely tuned to transition from a subsonic deflagration to a supersonic detonation (van Kerkwijk et al., 2010).

The goal of the research in this thesis is to constrain the nature of the progenitors of type Ia supernovae (see Fig. 1.4).

In addition to classification by progenitor model, supernovae of type Ia are often observationally sub-classified into three major groups: normal, 1991bg-like (Branch & Miller, 1993) and 1991T-like (Filippenko et al., 1992). 1991bg-like SNe are subluminous and present strong Si II (Hsiao, 2009); these supernovae are rarely used in cosmological surveys (e.g. Perlmutter et al. 1999, but see also Riess et al. 1996), although it is possible to "standardize" their light curves (González-Gaitán et al., 2014). On the other hand, 1991T-like SNe are overluminous and exhibit weak Ca II, Si II and S II absorption lines in their early spectra (Hsiao, 2009); these supernovae are usually considered as distance indicators (Guy et al., 2007). In particular, Phillips et al. (1992) remark that SN 1991T is similar to a normal Type Ia supernova, except for low abundances of Si, Ca and S in the outer ejecta.

One particular atypical type of supernova Type Ia is designated 2002cx-like. These supernovae present SN1991T-like pre-maximum spectra, SN1991bg-like luminosity, low expansion velocities, and weak, or absent, intermediate-mass element spectral features (Li et al., 2003).

Some SNe Type Ia have been reported to show an extremely high peak brightness (e.g. Maeda et al. 2009). These events are classified as superluminous and the amount
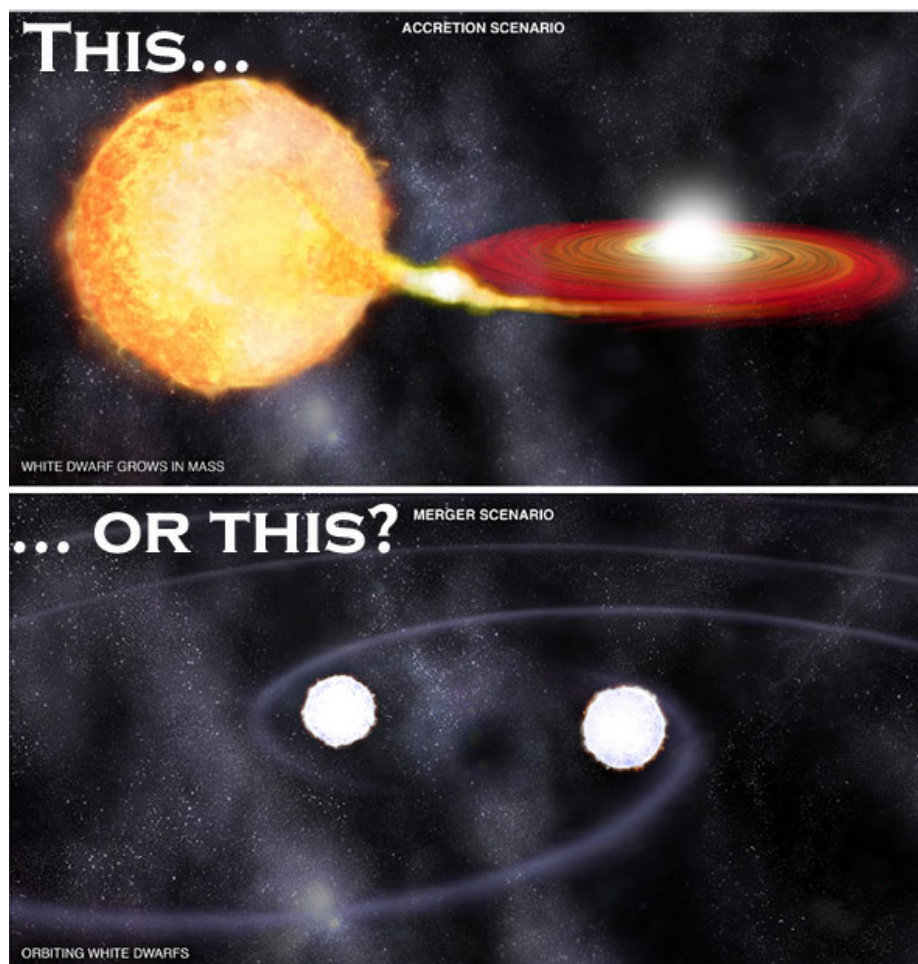
Figure 1.4 Artistic representation of the two most accepted progenitor channels of SNe Ia. Credit: Bad Astronomy Discovery.

of ^{56}Ni required to power the light curve indicates that the progenitor star had a super-Chandrasekhar mass (Howell et al., 2006). The spectra of this class of supernova often show carbon lines, suggesting the presence of unburned material in the ejecta. This unprocessed material further supports the super-Chandrasekhar mass progenitor, in which case the explosion is not expected to fully burn the CO-WD (Tanaka et al., 2010).

Table 1.1 shows a comparison of the energy output of core-collapse and Type Ia supernovae. The typical mass range of ejected Ni is included. Note that core-collapse supernovae are roughly two orders of magnitudes more energetic than Type Ia SNe. However, most of the energy released from CC SNe is in form of neutrinos, which do not add to the brightness of the explosion. Conversely, less than 10% of the total energy of Type Ia SNe escape as neutrinos. While the kinetic energy of the ejecta is comparable for both groups, only the brightest core-collapse SNe are as luminous as typical Type Ia SNe.

Table 1.1 Comparison between the characteristics of core collapse and Type Ia supernovae.

Supernova	Total E [10^{44} J]	Neutrino E [10^{44} J]	Kinetic E [10^{44} J]	Radiation E [10^{44} J]	Ejected Ni [$M_\odot$]
Type Ia	$\sim$1.5	0.1	1.3–1.4	$\sim$0.01	0.4–0.8
Core collapse	$\sim$100	100	1	0.001–0.01	0.01–1

From *Wikipedia*; see references therein (Mazzali et al., 2001; Iwamoto & Kunugise, 2006; Hayden et al., 2010b; Janka, 2012; Smartt, 2009)

The rest of this chapter is devoted to a further description of supernovae Ia. In §1.2 we provide examples of important applications of SNe Ia in both physics and astronomy. §1.3 further contrasts the two SN Ia channels and explains how the SN Ia rate is expected to differ in each scenario. §1.4 briefly describes how to employ colours of early type galaxies to probe different SN Ia channels. Finally, §1.5 reviews past works in this field, and explains the objectives of this thesis.

1.2   Motivation

1.2.1   Cosmological Application

The importance of Type Ia supernovae has grown since the pioneering work of Riess et al. (1998) and Perlmutter et al. (1999), who used SNe Ia as standard candles to probe the expansion rate of universe. These authors discovered that the universe is accelerating, implying that a non-zero dark energy component is required to explain the observed relation between redshift and effective peak brightness for a sample of SNe Ia (see Fig. 1.5).

Supernovae Ia are not true standard candles, since their peak brightness can vary by almost one magnitude (see top plot in Fig. 1.6). However, Phillips (1993) has shown that there is a correlation between the width of the light curve and its peak brightness; it is therefore possible to "standardize" SNe Ia light curves using a stretch factor to compute an effective peak brightness (see bottom plot in Fig. 1.6). Further studies have also found a colour–luminosity relation, indicating both that fainter supernovae are intrinsically redder, and that dust absorption is important (Tripp, 1998; Howell, 2011).

Non-normal SNe Ia are not rare ($\sim 30\%$ according to Li et al. 2011; see Fig. 1.7). However, as mentioned earlier, 1991bg-like and 1991T-like SNe light curves can also be standardized to some degree and, in particular, 1991T-like SNe are often used as distance indicators (Perlmutter et al., 1999; Guy et al., 2007). Therefore it is not impossible that a single channel is responsible for most SNe Ia.

Understanding possible sources of bias and systematic errors is paramount and can influence the measurements of the Hubble constant (Rigault et al., 2015) and dark energy properties (Conley et al., 2011; Foley et al., 2012). Also, the physical cause of the Phillips relation remains elusive. Similarly, understanding the contribution of each SN Ia channel is important if we are to understand the evolution of SN Ia properties at high redshift.

1.2.2   Galactic and Chemical Evolution

While the amount of Ni produced by a core-collapse supernova can vary by a few orders of magnitude ($0.01 \lesssim {}^{56}\text{Ni} \lesssim 1 M_{\odot}$, depending on the mass of the progenitor (Nomoto, 2014)), each SN Ia ejects $\sim$0.6-0.7 $M_{\odot}$ ^{56}Ni on average (Maoz et al., 2014). Ni radioactively decays to Fe, which is an important tracer of chemical evolution.
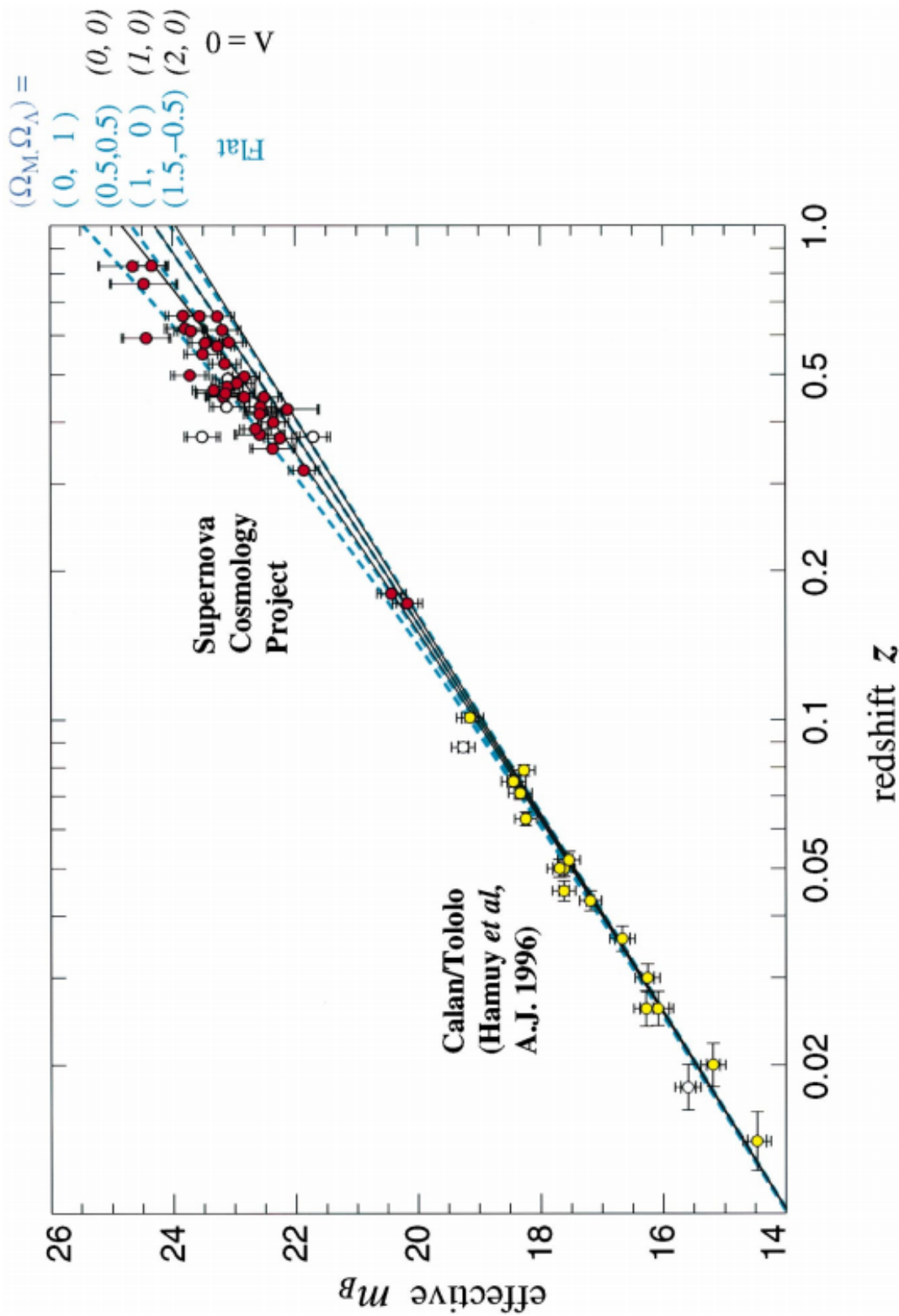
Figure 1.5 Hubble diagram for 60 SNe Ia from Perlmutter et al. (1999). The circles are SNe Ia measurements. The full black lines are expansion models with no dark energy contribution, while the dashed blue lines are flat universe models with different amounts of dark energy.
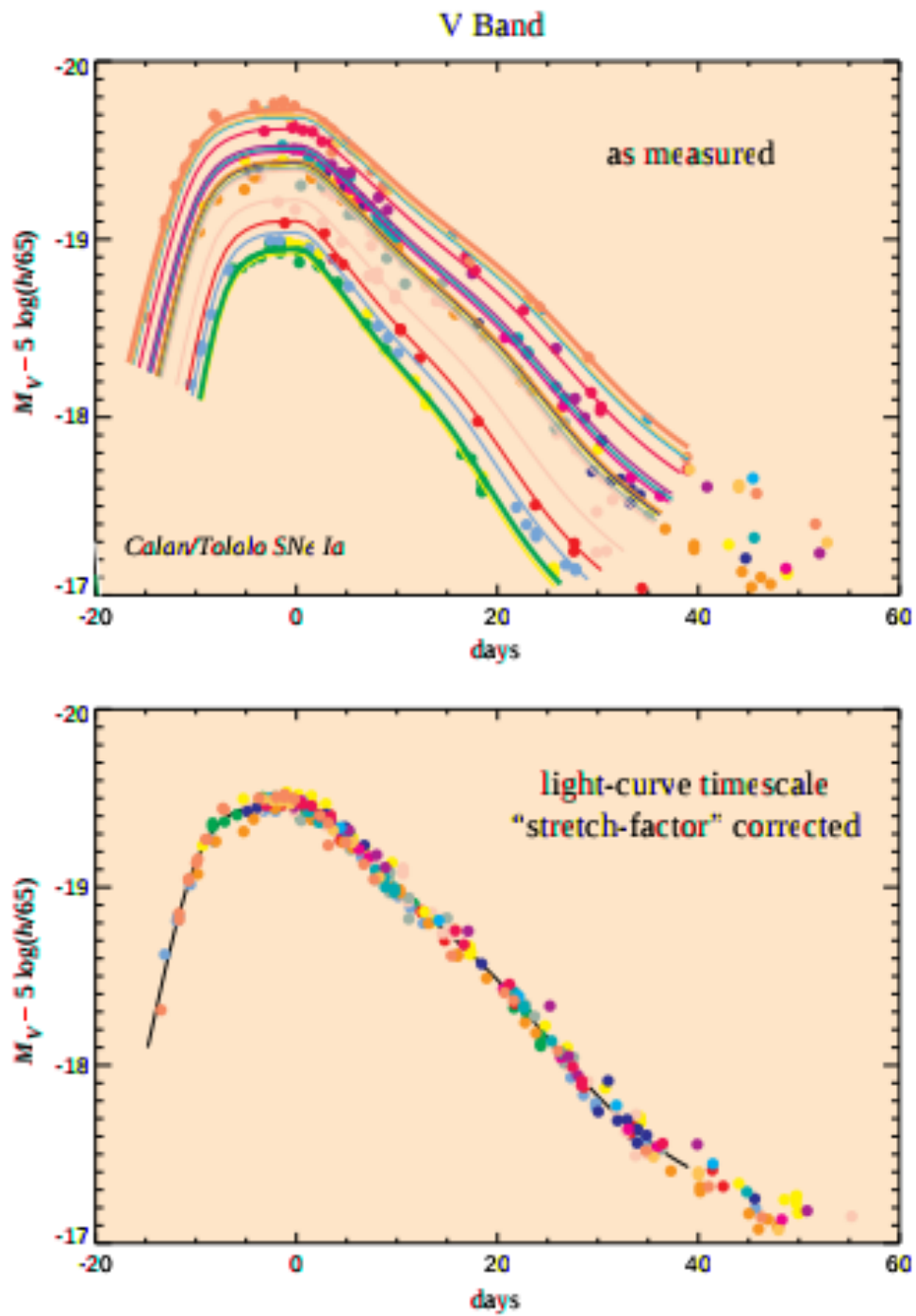
Figure 1.6 Relation between width and peak magnitude of the V band light curve of a sample of SNe Ia. From Perlmutter et al. (1997).
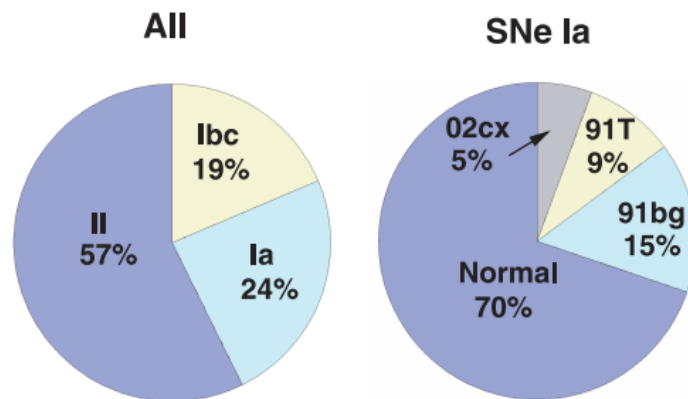
Figure 1.7 Supernova occurrence in a volume-limited sample. The identification of 1991T-like SNe is dependent upon spectra taken at early stages of the light curve. Thus the fraction of SN 1991T-like objects is a lower limit. From Li et al. (2011).

Core-collapse supernovae are estimated to be ~ 3 times more frequent than Type Ia supernovae. For instance, Smartt et al. (2009) find that $\sim 27\%$ of the observed SNe are Type Ia, while Li et al. (2011) find a fraction of 24%. Both groups used volume-limited samples to reach this conclusion, thus avoiding bias towards brighter objects. (For a magnitude-limited sample, the fraction of SNe Ia would increase to 79%). It should be noted, however, that volume-limited surveys are also subjected to selection effects. For instance, relatively low luminosity CC SNe could go undetected.

Therefore, CC SNe occur more often, but each event ejects less Fe than a SN Ia; this causes their relative contributions to galactic chemical enrichment to be comparable (at least for iron-peak elements).

It is important to note, however, that the occurrence rate of SNe Ia as a function of time is expected to be dependent on the progenitor system, and thus understanding the contributions of each SN Ia channel is also important for building reliable chemical evolution models (Wiersma et al., 2011).

1.3 The Progenitors of Supernovae Ia

The single and double degenerate scenarios are the two most widely-mentioned channels leading to SNe Ia. However, alternate scenarios and variants of the SD and DD cases have also been proposed. White dwarfs (and their companions) are faint; this makes the direct observation of progenitor systems (either pre- or post-explosion) extremely difficult. We therefore rely on indirect methods to test which channel is responsible for the majority of the observed SNe Ia.

In this work we probe the time between the formation of a simple population and the occurrence of SNe Ia. The so-called "delay time distribution" (DTD) is representative of an ideal case where a coeval set of stars[2] is allowed to passively evolve. The DTD is expected to depend on the progenitor scenario; probing the DTD can therefore provide valuable clues that may solve the progenitor problem.

The next sections discuss in more detail models that have been proposed for the progenitor systems of SNe Ia. We briefly summarize some alternate models following the review of Maoz et al. (2014). Progenitor models have an effect on the shape of the DTD; this is discussed in §3.6.1.

---

[2]A population of stars of the same age and metallicity

1.3.1 Single Degenerate Channel

The single degenerate channel was the first proposed scenario to explain how a WD could undergo a thermonuclear explosion (Whelan & Iben, 1973). This scenario involves only one CO WD, which accretes mass from a less evolved companion star.

Mass transfer is expected to occur via Roche-lobe accretion (Whelan & Iben, 1973; Hachisu et al., 1989) or by the capture of material ejected in stellar winds by the companion star (van den Heuvel et al., 1992). According to Nomoto (1982b), if the CO WD accretes hydrogen from the secondary, then a critical mass accretion rate is given by:

$$(dM/dt)_{crit} = 8.5 \times 10^{-7}(M/M_\odot - 0.52) \ M_\odot yr^{-1}, \tag{1.1}$$

where M is the WD mass. This model assumes spherical symmetry, the same initial abundance of C and O ($X_C = X_O = 0.5$) and that the effect of H shell flashes are neglected during the accretion phase (although mass loss during these events is discussed). Three cases are allowed: *(i)* if the accretion rate is $< 0.4 \times dM/dt_{crit}$, then the accreted hydrogen burning is unstable and recurrent flashes occur, most likely expelling the accreted material. The WD mass does not reach the Chandrasekhar mass, and no SN Ia is expected. These systems are, however, observed as recurrent novae (Starrfield et al., 1972). *(ii)* If the accretion rate is in the range $0.4 - 1 \times (dM/dt)_{crit}$ ($1.5 - 4 \times 10^{-7}$ $M_\odot$ yr^{-1} for a 1 $M_\odot$ CO WD), then the accreted material is stably burnt, increasing the mass of the WD, and eventually leading to a SN Ia. *(iii)* If the accretion rate is $> (dM/dt)_{crit}$, then the primary develops a red-giant–like envelope and no SN Ia is expected.

The case in which a sub-Chandrasekhar mass WD accretes directly from a Helium companion has also been investigated (e.g. Nomoto 1982a, Nomoto 1982b, Fink et al. 2007, Wang et al. 2009). The ignition of CO is triggered by a helium flash of the accreted material. We postpone a discussion of this case to §1.3.3.

The evolutionary phase of the secondary is also unclear. While it is usually thought to be main sequence star (Langer et al., 2000; Nomoto et al., 2000), scenarios where the primary accretes mass from a subgiant (Han & Podsiadlowski, 2004; Wang et al., 2009) or red giant (Patat et al., 2008; Kutsuna & Shigeyama, 2015) star have also been extensively discussed in the literature.

The occurrence of recurrent novae (RN) is a strong indicator of the SD channel, since novae involve a CO WD accreting from a non-degenerate companion, just like

an SD SN Ia progenitor. It remains uncertain, however, if the rather narrow dM/dt range for stable burning/accretion occurs often enough to match the observed SN Ia rates.

It is expected that the SD channel can lead to at least some SNe Ia, but it is not known whether SD explosions correspond to a particular subclass of SNe Ia. For instance, based on analytic calculations and full 3D simulations, Fisher & Jumper (2015) claim that the SD channel preferentially leads to overluminous SNe Ia and the contribution of this channel to other subclasses of SNe Ia is unlikely to exceed 1%. On the other hand, Cao et al. (2015) investigate UV features within four days of the explosion, finding supportive evidence that subluminous supernovae with low expansion velocities are from the SD channel.

The non-degenerate companion star is expected to survive the thermonuclear explosion of the primary. The main challenge of the SD channel is the current lack of direct observational evidence for such a companion. The interaction of the supernova ejecta with the secondary should produce detectable X-ray, UV and optical emission (Kasen, 2010). Hayden et al. (2010a) investigated a sample of over 100 confirmed SNe Ia and found no evidence for shock emission. This result strongly disfavours red-giants as common companions because the interaction of the ejecta with the envelope of a giant star would result in shock emission comparable to the supernova at peak, which is not observed. Nevertheless, main sequence secondaries with $M \lesssim 6 M_\odot$ cannot be ruled out. As mentioned above, Cao et al. (2015) found an early UV signature from SN iPTF14atg, supportive of the single degenerate channel. It should be noted, however, that the observed optical features were not consistent with the predictions from Kasen (2010).

A piece of evidence that supports the SD channel comes from the analysis of X-ray observations of Tycho's SN (Ruiz-Lapuente et al., 2004). An arc is observed inside the remnant (Lu et al. 2011; see Fig. 1.8), possibly indicating the interaction of the explosion with the companion's envelope. However, Kerzendorf et al. (2013) analyze the central six stars of Tycho's remnant, which are candidates for the companion of this SN. None of these stars exhibits characteristics expected for a single degenerate companion. Similarly, Ruiz-Lapuente (2012) investigated the supernova remnant 0509-67.5, which is located in the Large Magellanic Cloud, and was able to rule out the presence of any single degenerate companion.

Simulations of the interaction of the SN ejecta with a main sequence companion predict that $0.11-0.18 M_\odot$ of H and He are stripped off the donor during the explosion.
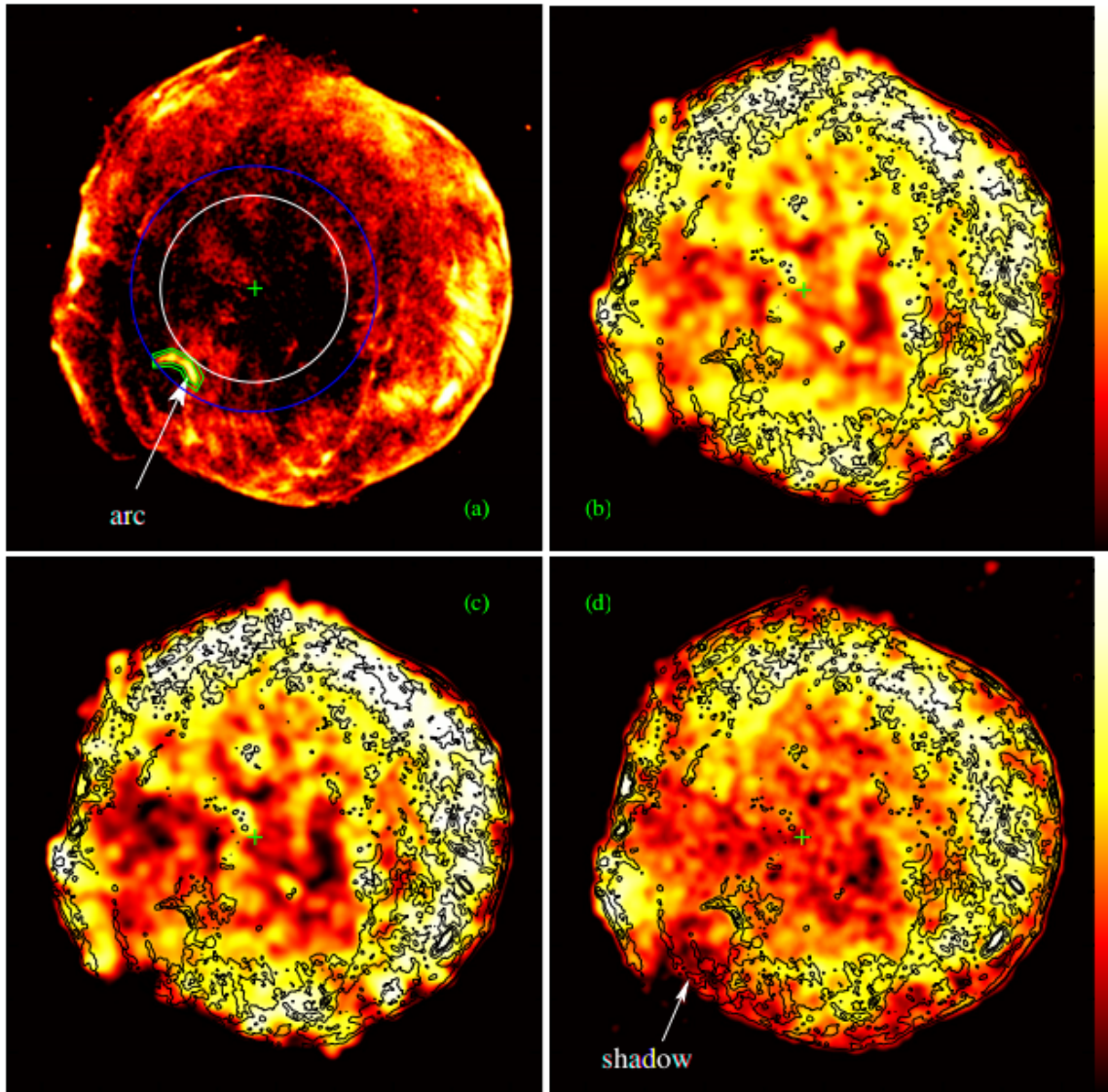
Figure 1.8 Tycho's remnant observed with *Chandra* using the ACIS-I spectrometer, from Lu et al. (2011). Panels (a), (b), (c) and (d) correspond to observations in the 4-6 KeV (non-thermal continuum), 1.6-2.0 KeV (Si), 2.2-2.6 KeV (S) and 6.2-6.8 KeV (Fe) bands, respectively. The colour coding is logarithmic and represents intensity. The green crosses correspond to the inferred explosion site.

The signature of these elements should be visible in the SN spectrum at late times when the ejecta become more transparent (Liu et al., 2012). Yet, no observational evidence of such a signature has been found. For instance, Leonard (2007) analyze a slightly subluminous and a normal supernovae and place an upper limit of $0.1 M_\odot$ of solar abundance material in the ejecta. A recent work by Lundqvist et al. (2015) investigates the presence of hydrogen lines in late optical spectra of SNe 2011fe and 2014J. The upper limits found for H mass in SN2011fe and SN2014J are $0.003 M_\odot$ and $0.0085 M_\odot$, respectively. The corresponding values found for He are $0.002 M_\odot$ and $0.005 M_\odot$. These constraints are at least one order of magnitude smaller than the values expected for the SD scenario, thus disfavouring this channel.

1.3.2   Double Degenerate Scenario

The double degenerate scenario was first proposed by Tutukov & Yungelson (1981). In the standard picture, a binary system composed of two CO WD's loses angular momentum via gravitational waves, causing the less massive CO WD to eventually be tidally disrupted and accreted onto the primary (Maoz et al., 2014; Pakmor et al., 2012). It has also been argued, however, that large accretion rates would cause off-centre ignition, producing Mg and Ne, which would induce electron capture reactions as the primary's mass grows towards the Chandrasekhar limit, ultimately forming a neutron star (Maoz et al., 2014; Shen et al., 2012).

Variants of the DD scenario include collisional models, where two CO WD's directly collide (Maoz et al., 2014; Lorén-Aguilar et al., 2010). This case could help to explain the occurrence of SNe Ia in the nuclei of galaxies, where the density is high enough and the probability of a head-on collision is non-negligible. Collisional models may also be applicable to SNe Ia in globular clusters.

As discussed in §1.3.1, the non-detection of residual amounts of hydrogen and helium in late-time spectra of SNe Ia, the non-detection of shock emission, and the non-detection of surviving companions all cast doubt on the SD scenario as the dominant channel. On the other hand, the DD channel cannot be ruled out by any of these observations.

Further evidence that supports the DD scenario includes the lack of radio emission from SNe Ia. In the SD channel, mass ejected by the secondary, or mass loss from the accretion flow, is expected to form a circumstellar medium (CSM) prior to the SN explosion. The interaction of accelerated electrons with the CSM would produce

synchrotron radiation that should be detectable at radio wavelengths (Maoz et al., 2014).

As argued in the previous section, the observation of recurrent novae is supportive of the SD channel, since these systems show a configuration similar to SD progenitors. Recurrent novae are thought to be a later evolutionary stage of supersoft X-ray sources (SSS). If RN are allowed to eventually trigger SNe Ia (Hachisu et al., 1999), then SSS are excellent SD candidates. The observed number of supersoft X-ray sources is, however, much smaller than would be expected to account for the majority of SNe Ia (Di Stefano, 2010). Whether this argument favours the SD or DD scenario has been disputed by Hachisu et al. (2010). The latter group claims that accreting WD's would spend a larger fraction of time in an optically thick regime and as recurrent novae, rather than in a SSS regime. This would lower the expected number of SD progenitors to be found as supersoft X-ray sources by roughly an order of magnitude, reconciling the predicted and observed rates. We note that this particular SD scenario often invokes a red-giant companion (Hachisu et al., 1999, 2010); this assumption may be unrealistic (see §1.3.1).

The occurrence of SNe Ia in early-type galaxies has been used to derive the SN Ia delay time distribution. The measured delay times support the DD scenario (e.g. Maoz et al. 2010), because these galaxies are predominantly composed of old populations with mostly low mass stars. These stars cannot trigger a SN Ia via the SD channel due to constraints on the mass of the donor (this is further discussed in §3.6.1). This argument is revisited throughout this thesis.

1.3.3   Sub-Chandrasekhar Models

In this scenario, a sub-Chandrasekhar mass WD accretes from a Helium companion at low mass accretion rates in the range $10^{-9} < dM/dt < 4 \times 10^{-8}$. This accretion may lead to a SN Ia through a process called *double detonation*, in which a helium shell flash induces carbon detonation. Hydrodynamic simulations indicate that even small helium shell masses ($\lesssim 0.01$ $M_\odot$) can trigger a double detonation SN Ia in a sub-Chandrasekhar mass WD (Fink et al., 2010). This version of sub-Chandrasekhar progenitor can, in principle, emerge from the DD channel, if the donor is a helium WD (e.g. Shen et al. 2013), or from the SD channel, if the donor is not supported by degeneracy pressure (e.g Wang et al. 2009). In the latter case, the presence of C and O in the predicted spectra is inconsistent with current observations (Maoz et al.,

2014).

In another variant of the DD model, two CO WD's of similar mass merge, but the total mass does not need to exceed the Chandrasekhar mass (van Kerkwijk et al., 2010). The merged object is surrounded by a dense disk, which is supported by degeneracy pressure. While this object is not hot and dense enough to ignite CO burning right after the merging process, its density can significantly increase through accretion of material from the thick disk. Compressional heating then causes the temperature to increase to $\sim 1.4 \times 10^9$ K, enough to ignite CO burning. Note, however, that this model is self-consistent only if the compressional heating timescale is shorter than the neutrino energy loss timescale. Such a condition holds if the contraction process is fast enough to be nearly adiabatic.

1.3.4 Core-Degenerate Channel

The recently proposed core-degenerate (CD) scenario stands between the standard single and double degenerate channels. Introduced by Kashi & Soker (2011), this scenario predicts that SNe Ia can occur as the result of the merger of a WD with the core of an asymptotic giant branch (AGB) star. Since the AGB core is degenerate, this channel resembles the DD scenario, but because it requires a companion that is not a WD, it is also similar to the SD channel.

In the core-degenerate scenario, a fraction of the common-envelope material remains bound to the binary system, forming a circumbinary disk (Aznar-Siguán et al., 2015). Both stars merge as a consequence of the interaction with this disk; the merging timescale of the CD channel is much shorter than the merging timescale of the DD channel.

1.3.5 Two Unconventional Models

Finally we consider two unconventional and possibly unrealistic models.

1. Quark Novae – Ouyed et al. (2014) propose that a binary progenitor system with a massive star ($M \gtrsim 8M_\odot$) and an intermediate mass star ($1 \lesssim M \lesssim 8M_\odot$) can also lead to SNe Ia. The primary eventually undergoes a core-collapse SN and becomes a neutron star (NS). When the secondary reaches the AGB phase, a common-envelope (CE) forms, causing the binary separation to shrink. In some cases the envelope may be ejected, resulting in a NS–CO WD tight binary system. On time scales $\gtrsim 1$ Gyr, the loss of angular momentum via gravitational waves further shrinks

the binary separation, causing the WD to overflow its Roche-lobe and transfer mass onto the NS. Ouyed et al. (2014) argue that when the NS surpasses a critical mass (1.6-1.9 $M_\odot$), a phase transition from hadronic matter to the theoretical up-down-strange (UDS) matter (Itoh, 1970) can occur, causing a quark nova explosion due to the release of quark deconfinement energy. The ejecta from this explosion would, in turn, collide with the WD, triggering a supernova type Ia. This model relies on many unverified assumptions, such as the transition to the UDS state of matter.

2. SNe Ia from Pycnonuclear Reactions in Single WD's – Pycnonuclear reactions can occur in high density environments (even at low temperatures), when electron screening effects become important, effectively decreasing and narrowing the Gamow peak and thus allowing the fusion reactions between slow moving nuclei (Harrison, 1964; Salpeter & van Horn, 1969). Chiosi et al. (2015) suggest that small amounts of hydrogen, $10^{-21} < X_H < 10^{-16}$ mixed in a CO WD can enhance the pycnonuclear reaction rate at densities of $10^7 - 10^8$ g cm^{-3}. Pycnonuclear reactions like ^{1}H+^{12}C would release enough energy to ignite carbon burning, leading to a thermonuclear runaway process, and therefore to a SN Ia. The CO WD mass range in which this channel would be viable is $0.85 \lesssim M_{WD} \lesssim 1.2$ $M_\odot$, lower than the Chandrasekhar limit. This proposed channel does not require a binary system; nor is it dependent on the Chandrasekhar limit. This model, however, depends on the assumption of very small quantities of residual hydrogen that current stellar models are not able to trace. Moreover, the authors point that the calculations do not take into account energy release due to element stratification, solid state transitions and gravitational contraction.

1.4   Early Type Galaxies

We approach the SN Ia progenitor problem by investigating the supernova rate in early type galaxies (E/S0) – galaxies with very low gas content and star formation rates, and a large dominant spheroidal component. Whether these galaxies passively evolve according to a monolithic formation scenario (e.g. Chiosi & Carraro 2002), or undergo successive merger episodes according to a hierarchical scenario (e.g. Hatton et al. 2003), is still unclear. However, it is known that these galaxies are generally composed of old populations with only a small admixture of younger stars, and can be found in a particular locus of the colour-magnitude diagram (CMD), called the
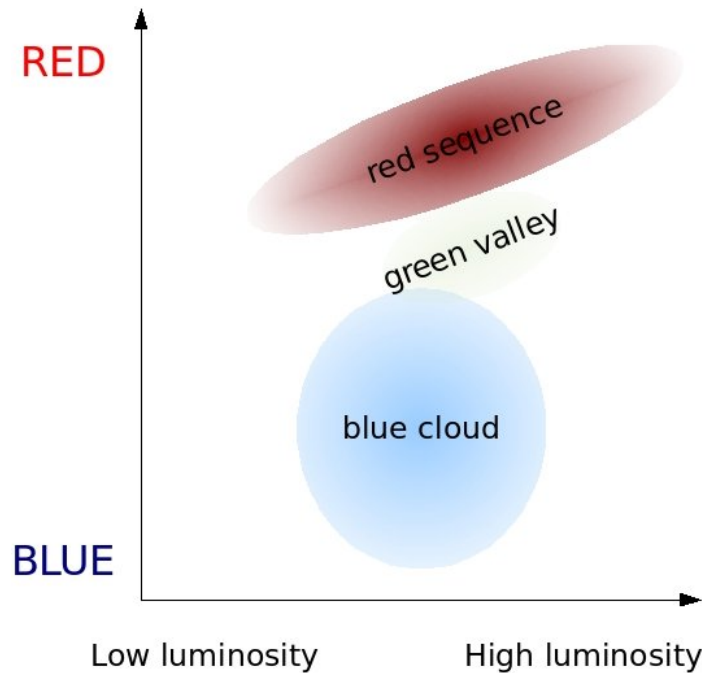
Figure 1.9 Schematic representation of the locus of galaxies in a colour-magnitude diagram. From Wikipedia.

red sequence (RS; Strateva et al. 2001; see Fig. 1.9)[3].

Early type galaxies are usually thought of as quiescent galaxies formed in short bursts at high redshifts ($z > 2$) (Jimenez et al., 2007; Maoz et al., 2014). This is an accurate statement for most of the galaxies on the RS; for example, Schawinski et al. (2007b) find that $\sim 82\%$ of the galaxies in a sample of morphologically selected early type galaxies are quiescent. Nevertheless, it has been observed that recent star formation (RSF) might occur in *some* early type galaxies (Ferreras et al., 1999; Ferreras & Silk, 2000; Schawinski et al., 2007a; Kaviraj et al., 2007).

The colour of a galaxy can be used to trace residual amounts of young populations. An early type galaxy with very red colours is not expected to have experienced any episodes of RSF, while slightly bluer colours with respect to the RS indicate the presence of young stars, which are hotter and have stronger emission at shorter wavelengths (Schawinski et al., 2007a; Kaviraj et al., 2007). In particular, the $NUV - r$ colour is very sensitive to even small amounts ($\sim 1\%$) of RSF and has been used to further investigate the evolution (Kaviraj et al., 2007), environmental effects (Schawinski et al., 2007a), distribution (Wyder et al., 2007), and SN Ia occurrence (Schawinski,

---

[3]A small fraction of galaxies in the RS are not actually early type (Graves et al., 2009).

2009) in early type galaxies.

It should be noted that old stars populating the extended horizontal branch (EHB) can also make a galaxy bluer (Petty et al., 2013). However, Yi et al. (2005) utilized both far- and near-UV bands to investigate a sample of 62 early type galaxies and concluded that only 4 objects exhibited UV flux that *could* be due to old stars. Thus, the observed colour deviations with respect to the RS are more likely to be due to younger populations. In our work (which does not include the FUV filter), we simply assume that the fraction of EHB stars is the same in all RS galaxies, and that the dominant mechanism causing deviations from the RS is young(er) stellar populations (and possibly metallicity).

To investigate the rate of SN Ia in early type galaxies, we model these galaxies as a composite of two populations: a dominant old population, plus a residual young population. We analyze the representative cases of 1% and 10% mass fraction in young stars. The age of the young population is inferred from the colour deviation with respect to the RS and the age of the old population is assumed to be 10 Gyr. We show in §3.7.1 that variations of a few Gyr in the assumed age of the RS are not relevant. Other works that have employed a double-burst model include Ferreras & Silk (2000), Yi et al. (2005), Kaviraj et al. (2007), and Schawinski (2009).

For each galaxy, from a set of assumed parameters (mass fraction, age of the young population and age of the old population), it is possible to compute the expected SN Ia rate from each progenitor channel, using the appropriate delay time distribution. Because the single degenerate channel requires a more massive main sequence star (as will be seen in §3.6.1), this scenario is less likely to occur in old populations, whereas in the double degenerate scenario, the longer timescale set by the loss of angular momentum via gravitational waves allows older populations to host SNe Ia.

1.5   Context

The observation of supernovae of type Ia in early type galaxies is often interpreted as supportive of a DTD expected from the DD channel (e.g. Maoz et al. 2010; see Fig. 1.10). This conclusion is usually based on the assumption that these galaxies can be represented by a single old population and that such populations are less likely to drive SNe Ia via the SD channel (a detailed discussion is reserved for §3.6.1). While this is a reasonable approximation, it is unable to account for a possible contribution from residual young populations.
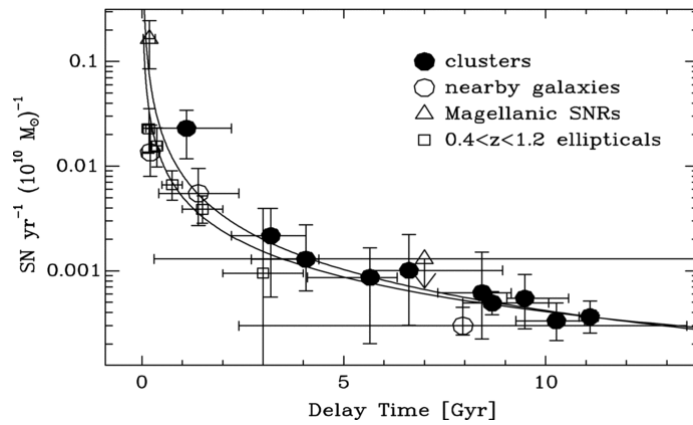
Figure 1.10 Delay times derived from the age of cluster galaxies (filled circles) modeled as single bursts. The curves represent scaled power laws with slopes of -1.1 and -1.3. From Maoz et al. (2010), and references therein.

Schawinski (2009) models early type galaxies as a composite of an old plus young population, and uses the $NUV - r$ colour to probe the age of the young population. Under the assumption that the SNe are hosted by the younger population, he is able, for the first time, to reconcile the occurrence of SNe in early-type galaxies with the DTD expected from the SD channel. It is made clear, however, that the observed SNe could have longer delay times, if hosted by the older population.

Another conclusion of Schawinski (2009) is that no 'prompt' ($\lesssim$100 Myr) SNe Ia are observed (corroborated by Anderson et al. 2015). This result is more robust than the previous, given that the ages probed are actually *minimum* delay times. A caveat to this conclusion, shared in our work, is that the colours used are not sensitive to exceptionally small fractions of young population ($\lesssim 1\%$). We postpone the discussion of effects of such small mass fractions to §5.

Whether the old or residual young population (or both) are responsible for the observed SNe Ia in early type galaxies remains unclear; which progenitor channel is favored depends heavily on the assumptions involved. Our work differs from previous studies in that we take into account the *composite* contribution of both populations to calculate expected supernova rates for DTD's representative of each channel. Moreover, we derive supernova rates per unit luminosity, rather than per unit mass, since the mass of a galaxy cannot be easily inferred. There is a powerful advantage to the luminosity approach, as will be seen.

The content of this thesis is as follows: §2 describes how we constructed our data samples, while §3 explains the model used to compute the expected SN occurrence as a function of colour. §4 presents our findings, which are then discussed and summarized in §5.

Chapter 2

Data Analysis

2.1 Overview

As described in §1, our objective is employ supernova surveys to compare the observed and expected rate of SN Ia. For each survey we construct a control and a host sample. The first contains the targeted galaxies that satisfy our selection criteria and the latter is a subsample of the first and consists of the galaxies that hosted a SN Ia. In this chapter we characterize our data samples.

In order to apply our models (described in §3), we need to compute, for each galaxy in a given survey, the colour deviation with respect to the Red Sequence. To this intent, the observed galaxies must have photometric data available, and a redshift (either photometric or spectroscopic). More importantly, the samples must have been targeted for a SN Ia survey.

We deal with three low redshift samples: MENeaCS, SDSS and GALEX+SDSS. For each sample, the standard procedure is to first compute the absolute magnitudes, applying the galactic extinction- and k- corrections[1] to the raw apparent magnitudes. The second step is to exclude the objects that do not satisfy our selection criteria. Finally, we fit the Red Sequence[2] and compute the colour deviation of each galaxy with respect to this fit. It should be noted that the completeness of the samples, at any given colour, should not influence our results, since it affects the control and host samples equally.

This chapter is divided as follows: §2.2, §2.3 and §2.4 describe the MENeaCS, SDSS and GALEX+SDSS samples, respectively. §2.5 explains how we fitted the RS

---

[1]k-corrections account for the shift of the rest frame spectrum of a galaxy according to its redshift.
[2]Meaning that we fit the locus of the red sequence in the color-magnitude diagram.

for each of the samples and how the $\Delta(colour)$ quantity is computed. §2.6 describes an alternative, k-correction independent, method to compute $\Delta(colour)$. §2.7 characterizes the subsamples that will be used to derive the expected SN Ia rate. A brief summary of this chapter is provided in §2.8.

2.2 The MENeaCS Sample

The Multi-Epoch Nearby Cluster Survey (MENeaCS; Sand et al. 2011, 2012) sampled 57 X-ray selected rich galaxy clusters with redshifts $0.05 < z < 0.15$. Repeated g- and r-band observations of these clusters were obtained over a 2 year period using the Canada-France-Hawaii Telescope with its MegaCam imager. The detection limit was $g=r=23.5$ mag for supernovae in the difference imaging, and the k-corrections were performed using the KCORRECT software package (Blanton & Roweis, 2007).

The MENeaCS survey spectroscopically confirmed 23 cluster SNe Ia (4 of which were almost certainly intracluster events which are not used in our analysis). Other than SN Ia hosts, spectroscopy is available only for some of the brighter galaxies in clusters which overlap the SDSS footprint.

We adopt an arbitrary colour cut of $g - r = -0.8$ to remove spurious objects; any object bluer this limit is removed from the control sample, leaving 57,313 out of the initial 57,638 galaxies. Out of the 19 cluster hosts, 2 galaxies are fainter than the detection limit and 1 galaxy is redder than the reddest galaxies in the control sample; we do not consider these hosts in our analysis. Thus, our MENeaCS sample of SN Ia hosts contains 16 galaxies.

2.3 The SDSS Sample

The Sloan Digital Sky Survey (SDSS; York et al. 2000) uses a 2.5m telescope that has been operating since 2000. Currently, there are three major surveys: SDSS-I (2000-2005), SDSS-II (2005-2008) and the recently finished SDSS-III (2008-2014). The on-going survey (SDSS-IV) is expected to run until 2020. In this work, we make use of the final SDSS-II DR-7 data release (Abazajian et al., 2009).

SDSS acquires photometry in five filters: u,g,r,i,z (Fukugita et al., 1996) with average wavelengths of 3551, 4686, 6165, 7481 and 8931 Å and 95% completness limits of 22.0, 22.2, 22.2, 21.3 and 20.5, respectively. The median resolution in the r

band is 1".4. The solid angle coverage (footprint) is $\sim$11,600 square degrees and the average exposure time per scan per filter is 54.1 s (Abazajian et al., 2009).

SDSS is also equipped with a spectrograph covering 3800 Å to 9200 Å. Its resolution is $\lambda/\Delta\lambda \sim 2000$. Objects brighter than $r = 17.77$ (where the magnitude is a galactic extinction-corrected Petrosian magnitude) are targeted for spectroscopic follow-up (Abazajian et al., 2009).

2.3.1   The SDSS-II Supernova Survey

The SDSS telescope was used to repeatedly scan a $\sim$ 300 sq. deg. region defined by: -60° < R.A. < 60° and -1.26° < Decl. < 1.26° . This region is designated Stripe 82; it was imaged, on average, every five nights during three month seasons from 2005 to 2007 (Frieman et al., 2008).

This survey has resulted in the discovery of more than 300 SNe Ia that were spectroscopically confirmed by other telescopes. Among these SNe Ia, 53 were hosted by galaxies that were targeted for the SDSS spectroscopic follow-up. The host-matching procedure is that of Sullivan et al. (2006), and is described in detail in Gao & Pritchet (2013).

2.3.2   The SDSS Control Sample

Of the more than 4,000,000 galaxies found in the Stripe 82 region, we subselect those that are part of the SDSS spectroscopic sample, trimming the number of objects in the sample to 20,707.

The data is treated as follows: first we correct the raw apparent magnitudes (see Fig. 2.1) by the galactic extinction values provided in the SDSS DR-7 catalog (see Fig. 2.2). (SDSS uses the Galactic extinction map of Schlegel et al. 1998.) The absolute magnitude is then calculated using:

$$M_X = m_X - 5log_{10}D_L - 25 - K_X(z) + Q \cdot z, \qquad (2.1)$$

where X is the passband, M is the absolute magnitude, m is the galactic extinction corrected apparent magnitude, D_L is the luminosity distance, K_X is the k-correction in the X filter and Q is the evolutionary factor.

The evolutionary correction, $Q \cdot z$, is computed using $Q = 1.6$ (Wyder et al., 2007). The k-corrections are computed relative to redshift zero using the KCOR-

RECT program, version 4.2 (Blanton & Roweis, 2007). This package contains a set of spectra of both star-forming and quiescent galaxies which are computed from the Bruzual & Charlot (2003) models. The program finds the linear combination of templates that better reproduces the observed photometry at the measured redshift. The k-corrections are then calculated by shifting the fitted spectrum to the desired redshift.

The adopted cosmological parameters are based on the results of Planck Collaboration et al. (2014); $H_0 = 67.04$ [Km s^{-1} Mpc^{-1}], $\Omega_\Lambda = 0.6817$ and $\Omega_m = 0.3183$.

We accept galaxies in the redshift range $0.01 < z < 0.2$ with galactic extinction corrected magnitudes $14.0 < r_{ext} < 17.77$. We limit the redshift range to ensure a complete SN sample. When computing the colour $X - r$, we also require X to be brighter than the 95% completeness limit, with errors X_{err}, $r_{err} < 0.2$. The number of objects in the control sample is reduced to 11,545 and 18,480 for the $u - r$ and $g - r$ colours, respectively. The selection criteria are summarized in Table 2.1.

2.4   The GALEX-SDSS Sample

In addition we combine SDSS r band photometry with near ultraviolet (NUV – 1771-2831 Å) photometry from The Galaxy Evolution Explorer (GALEX; Martin et al. 2005) to form an $NUV - r$ color which is very sensitive to small amounts of star formation (e.g. Schawinski et al. 2007a). The resolution of the NUV imaging is about 4.5 arcsec, vs. 1.4 arcsec in the SDSS r band; the effect of these resolution differences on $NUV - r$ color is small compared to the observational errors (Ree et al., 2007, 2012).

We use the Bianchi et al. (2011) matched GALEX+SDSS catalog, which uses a matching radius of 3" for pointlike (in GALEX) sources with NUV photometric errors < 0.5 magnitudes. We select only objects detected in the GALEX Medium Imaging Survey (MIS), since it has longer exposure time than the All Sky Survey. The area coverage of the MIS survey is $\sim$1000 sq. deg. and the 5σ limiting AB magnitude (Oke & Gunn, 1983) for NUV is 22.7 in the MIS survey.

The majority of the galaxies in this sample has colours bluer than the RS. The redder objects tend to exhibit low NUV fluxes and consequently magnitude errors larger than the adopted rejection limit, $NUV_{err} < 0.4$. Extinction corrections are performed using the extinction coefficients from Yuan et al. (2013): $R_{FUV} = 4.37$, $R_{NUV} = 7.06$, $R_u = 4.35$, $R_g = 3.31$, $R_r = 2.32$, $R_u = 1.72$, $R_u = 1.28$; these values

were derived using the Galactic extinction map of Schlegel et al. (1998), so that the reddening values are consistent with the SDSS sample (see §2.3).

Absolute magnitudes are also computed using the KCORRECT package (Blanton & Roweis, 2007), except that we provide FUV (when available), NUV, u, g, r, i, z photometry as input. We remove all objects for which the KCORRECT program is unable to compute the k-correction.

Table 2.1 Selection Criteria for the SDSS and SDSS+GALEX samples.

$NUV - r$	$u - r$	$g - r$
$0.01 \leq z_{spec}^a < 0.2$	$0.01 \leq z_{spec} < 0.2$	$0.01 \leq z_{spec} < 0.2$
$r < 22.75$	$14.0 \leq r_{ext} < 17.77$	$14.0 \leq r_{ext} < 17.77$
$16.0 \leq NUV < 23.25$	$u < 22.0$	$g < 22.2$
$r_{err} < 0.2$	$r_{err} < 0.2$	$r_{err} < 0.2$
$NUV_{err} < 0.4$	$u_{err} < 0.2$	$g_{err} < 0.2$

a Spectroscopic redshift

2.5 Red Sequence Fit

The RS fitting procedure of the MENeaCS sample is similar to Pimbblet et al. (2002) and is described in detail in Sand et al. (2012). The RS fit and colour deviations from the RS were independently computed for each cluster; the average $g - r$ slope is -0.026.

Due to the incompleteness of our GALEX+SDSS sample at red colours, our RS is not prominent and any fitting procedure would be susceptible to large uncertainties. Thus we adopt the linear fit values from Wyder et al. (2007): $(NUV - r)_{RS} = -0.175M_r + 1.897$. It should be noted that their sample is also constructed by combining SDSS and GALEX measurements, but unlike our sample, they are not restricted to the Stripe 82 region. Also, they compute k-corrections with respect to redshift 0.1, while we have chosen redshift zero as reference.

We fit the RS for the SDSS $u - r$ and $g - r$ control samples using an iterative rejection method, which accepts galaxies that belong to the RS locus only (the rejected objects are not excluded from the control sample; they are simply not considered for fitting the RS.) First, we visually reject the objects that clearly do not belong to the

RS, and make an initial guess for the linear coefficient and intercept parameters. The standard deviation is computed via:

$$\sigma_i = \sqrt{\frac{\sum_{k=1}^{N_i}((X-Y)_{obs,k} - (X-Y)_{fit})^2}{N_i - 1}}, \tag{2.2}$$

where N_i is the number of accepted objects at a given iteration i, $X - Y$ is the colour, Y is the magnitude and the quantity $(X - Y)_{fit}$ is determined at Y_k. All objects for which $|(X - Y)_{obs} - (X - Y)_{fit}| > 2 \cdot \sigma_i$ are then rejected and a new linear fit that minimizes χ^2 is computed. The iteration stops when the number of accepted objects remain invariant after an iteration (see Fig. 2.4). The σ computed at the last iteration, however, is not adequate to characterize the standard deviation of the RS. This is because the standard deviation is very sensitive to the reddest galaxies, which are rejected by this method and thus not taken into account in deriving σ.

We then compute the $\Delta(colour)$ of each galaxy (see Fig. 2.5) by subtracting the fitted colour of the RS at a given magnitude from the observed extinction- and k-corrected colour of a galaxy:

$$\Delta(X - Y) = (X - Y)_{abs} - (X - Y)_{fit}. \tag{2.3}$$

The standard deviation of the RS is calculated by fitting a Gaussian to the control sample's histogram in $\Delta(colour)$ parameter space. We only accept galaxies redder than a chosen colour cut to fit the RS. This is simply to reduce contamination from objects that belong to the green valley or the blue cloud loci. No bimodal fit has been attempted since such models are not always capable of accounting for the number of galaxies in the green-valley (e.g. Wyder et al. 2007). Figs. 2.6, 2.7, 2.8 and 2.9 show the best fit curves for each control sample.

The RS linear coefficient, intercept and standard deviation are shown in Table 2.2. In particular, the fitted linear coefficient of the SDSS $g - r$ sample, -0.019, is in agreement with the average value found for the MEneaCS sample, -0.026, and with the value obtained by Hogg et al. (2004), -0.022. Similarly, the linear coefficient of the $u - r$ SDSS sample, -0.069, is in agreement with the value found by Baldry et al. (2004), -0.08.

Table 2.2 RS parameters.

Color	Sample	slope	intercept	σ
	MENeaCS	-	-	-
$(NUV - r)$	SDSS	-	-	-
	GALEX-SDSS	-0.175^{a}	1.897^{a}	0.360
	MENeaCS	-	-	-
$(u - r)$	SDSS	-0.069	0.875	0.21
	GALEX-SDSS	-	-	-
	MENeaCS	-0.026	1.351	0.039
$(g - r)$	SDSS	-0.0188	0.347	0.04
	GALEX-SDSS	-	-	-

[a]Parameters for $NUV - r$ are from Wyder et al. (2007).
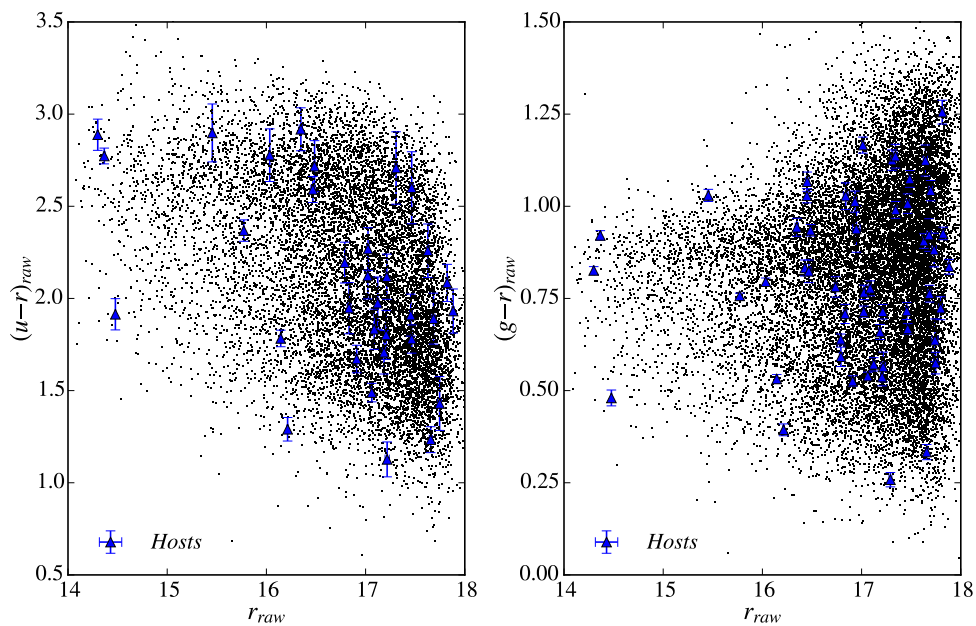
Figure 2.1 Raw colour-magnitude diagrams of the SDSS $u - r$ (left panel) and $g - r$ (right panel) control samples.
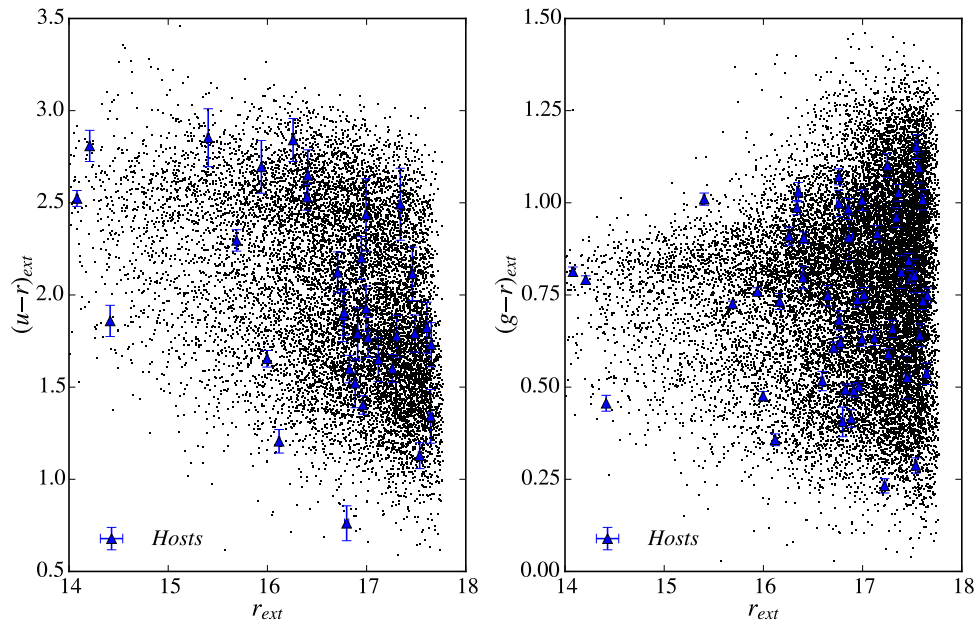
Figure 2.2 Extinction corrected colour-magnitude diagrams of the SDSS $u - r$ (left panel) and $g - r$ (right panel) control samples.
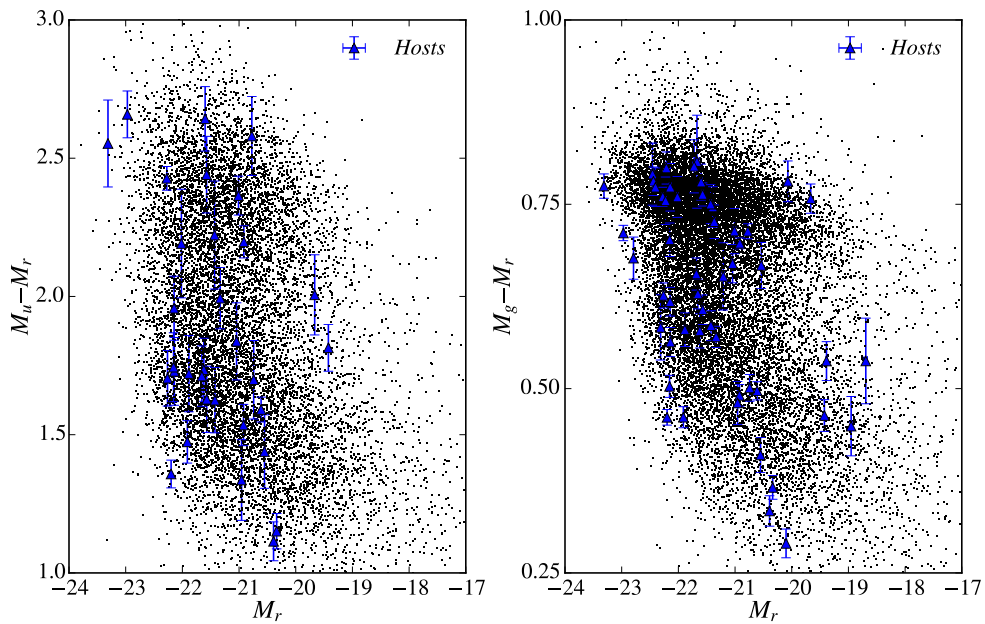
Figure 2.3 Extinction and k-corrected colour-magnitude diagrams of the SDSS $u - r$ (left panel) and $g - r$ (right panel) control samples.
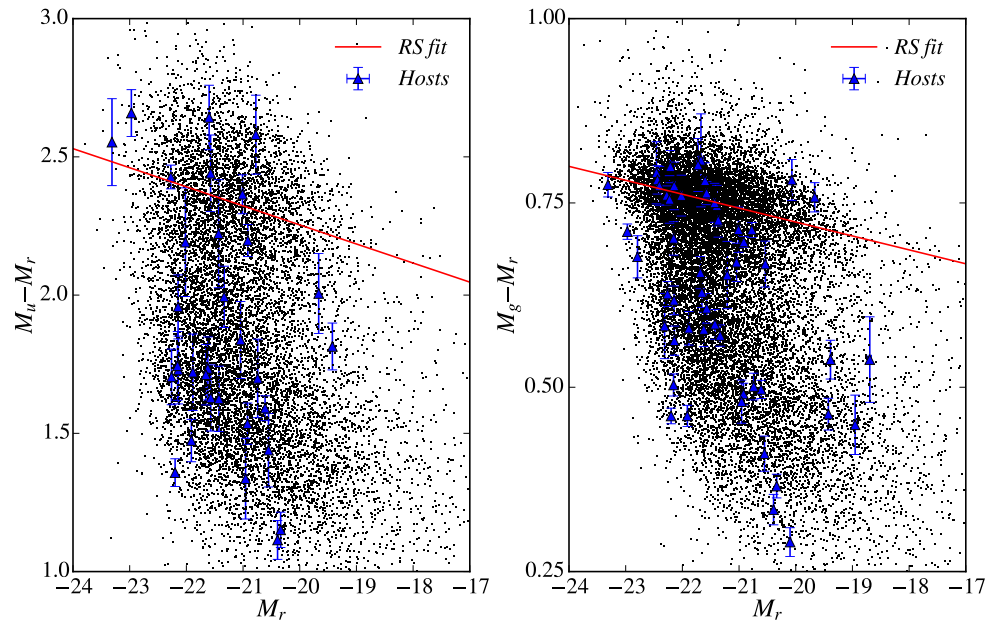
Figure 2.4 Same as Fig. 2.3. The red line is the linear fit of the red sequence obtained via an iterative rejection method.
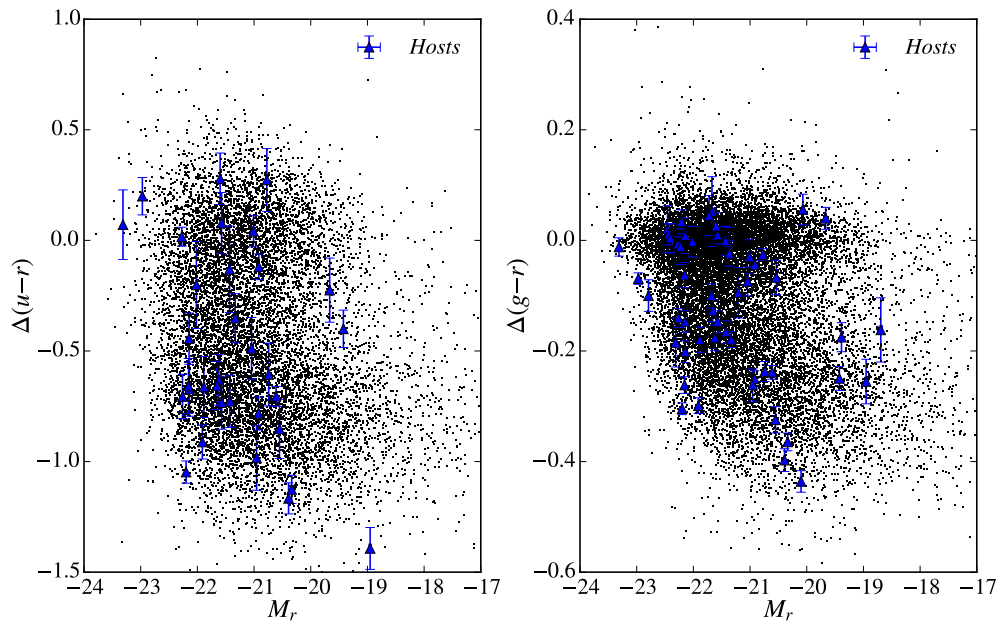
Figure 2.5 $\Delta(colour)$-magnitude diagram of the SDSS $u - r$ (left panel) and $g - r$ (right panel) control samples. The $\Delta(colour)$ is computed by subtracting the red sequence fitted colour at a given magnitude from the galactic extinction- and k-corrected observed colours.
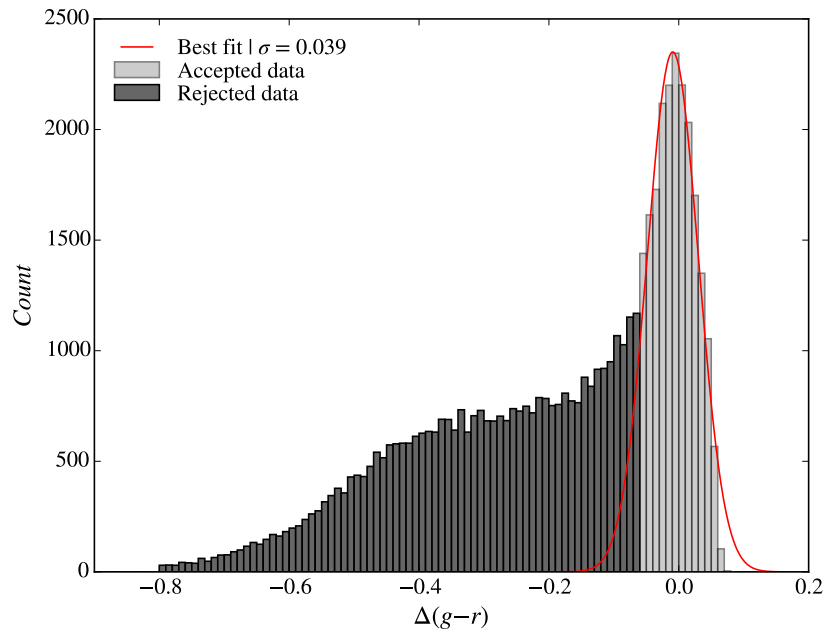
Figure 2.6 Histogram of the MENeaCS control sample in $\Delta(g - r)$ parameter space. The light and dark gray shades correspond to the accepted and rejected bins for the Gaussian fit (red line).
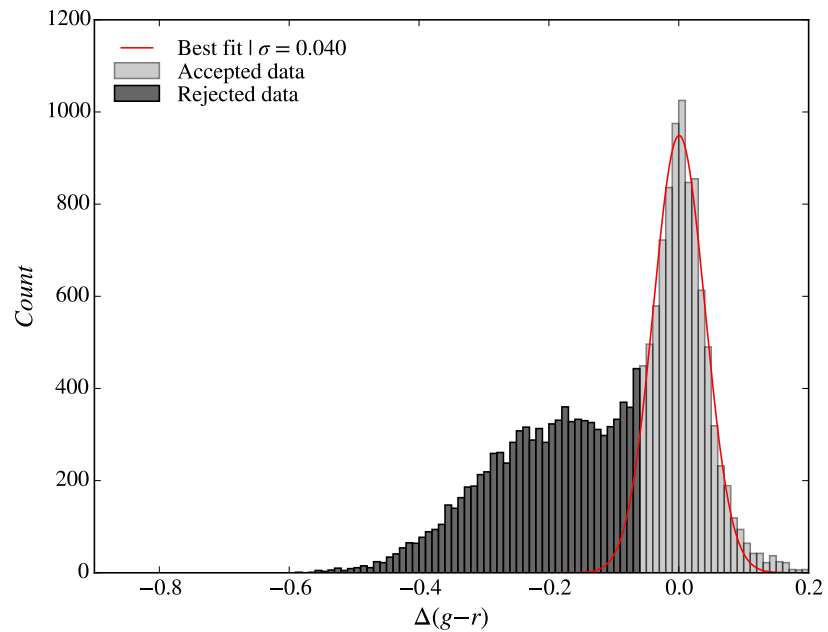
Figure 2.7 Same as Fig. 2.6, but for the SDSS $g - r$ control sample.
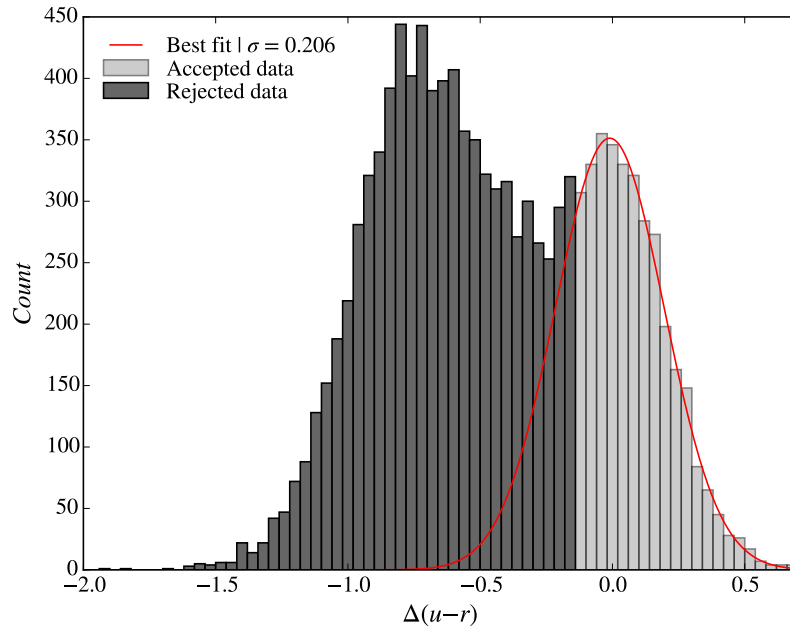
Figure 2.8 Same as Fig. 2.6, but for the SDSS $u - r$ control sample, in the $\Delta(u - r)$ parameter space.
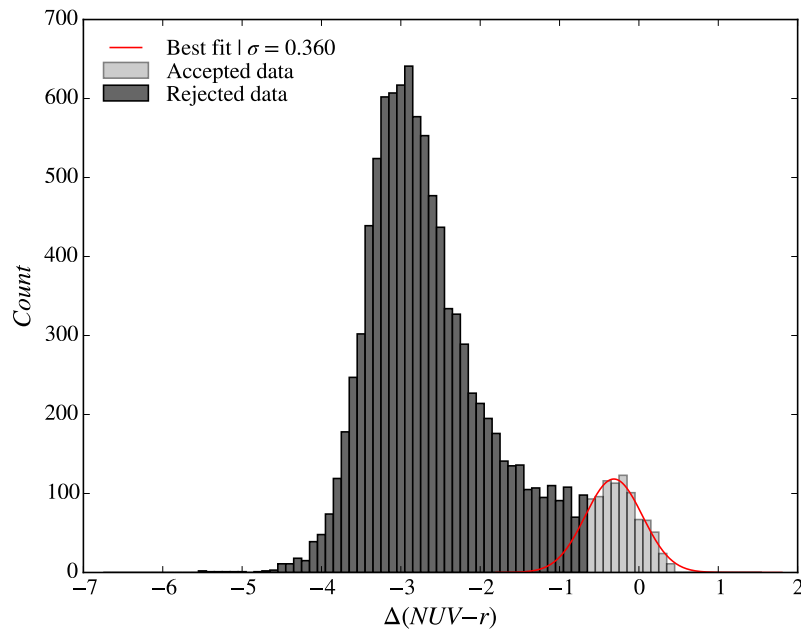
Figure 2.9 Same as Fig. 2.6, but for the GALEX+SDSS control sample, in the $\Delta(NUV - r)$ parameter space.

2.6 Alternative Methods

We also computed the $\Delta(colour)$ quantity using an alternative method, which relies on fitting the RS in colour-redshift space, rather than colour-magnitude space. The advantage of this method is that it is independent of k-corrections and therefore it is not necessary to use the KCORRECT software package. Thus, this method is less susceptible to uncertainties in fitting spectral energy distribution templates to the observed photometry. We employ this technique with the SDSS $g - r$ sample.

In this method, we first compute the galactic extinction correction for the raw magnitudes. The second step is to compute absolute magnitudes, not taking into account k-corrections (because these are accounted for below). Next, we correct for the red sequence slope: $(X - Y)_s = (X - Y)_{abs} + S_{corr}$, where

$$S_{corr} = slope \cdot (Y_{ref} - Y_k), \tag{2.4}$$

$slope$ is the slope of the red sequence, Y_{ref} is an arbitrary reference absolute magnitude and Y_k is simply the galaxy's absolute magnitude. Note that $(X - Y)_{abs} = (X - Y)_{ext}$, since the k-corrections are not taken into account to compute the absolute magnitudes. The reference magnitude employed was $M_r = -20$.

Since we want this method to be independent of the standard $\Delta(colour)$ calculation presented in §2.5, we adopt the $g - r$ $slope$ from Hogg et al. (2004), -0.022.

The red sequence is fit in the $z - (X - Y)_S$ parameter space using an iterative rejection method (as described in §2.5, except that we use a cubic polynomial, rather than linear fit), and the $\Delta(X - Y)$ values are computed by subtracting the RS fitted colour from $(X - Y)_s$. The respective colour-redshift diagrams are shown in Fig. 2.10.

The technique of fitting the RS in the z-colour domain, and then removing it, makes the implicit assumption that the k-correction is identical for red and blue galaxies. This is definitely not the case. The comparison between the $\Delta(colour)$'s obtained from each method can be misleading, since the objects in the RS locus will always exhibit $\Delta(colour) \sim 0$ (see Fig. 2.11).

We compare the colours which are used to compute $\Delta(g - r)$, i.e.: $M_g - M_r$ and $(g - r)_s$. The net effect is that blue colours get distorted relative to red colours, and by different amounts at different redshifts. The strong disagreement between the colours of the red-most objects is mainly due to the 4000 Å break being redshifted into the green filter range ($\sim$ 3800-5400 Å). This break is caused by metal absorption lines that are present in older populations, i.e., redder galaxies (see top plots in Fig.
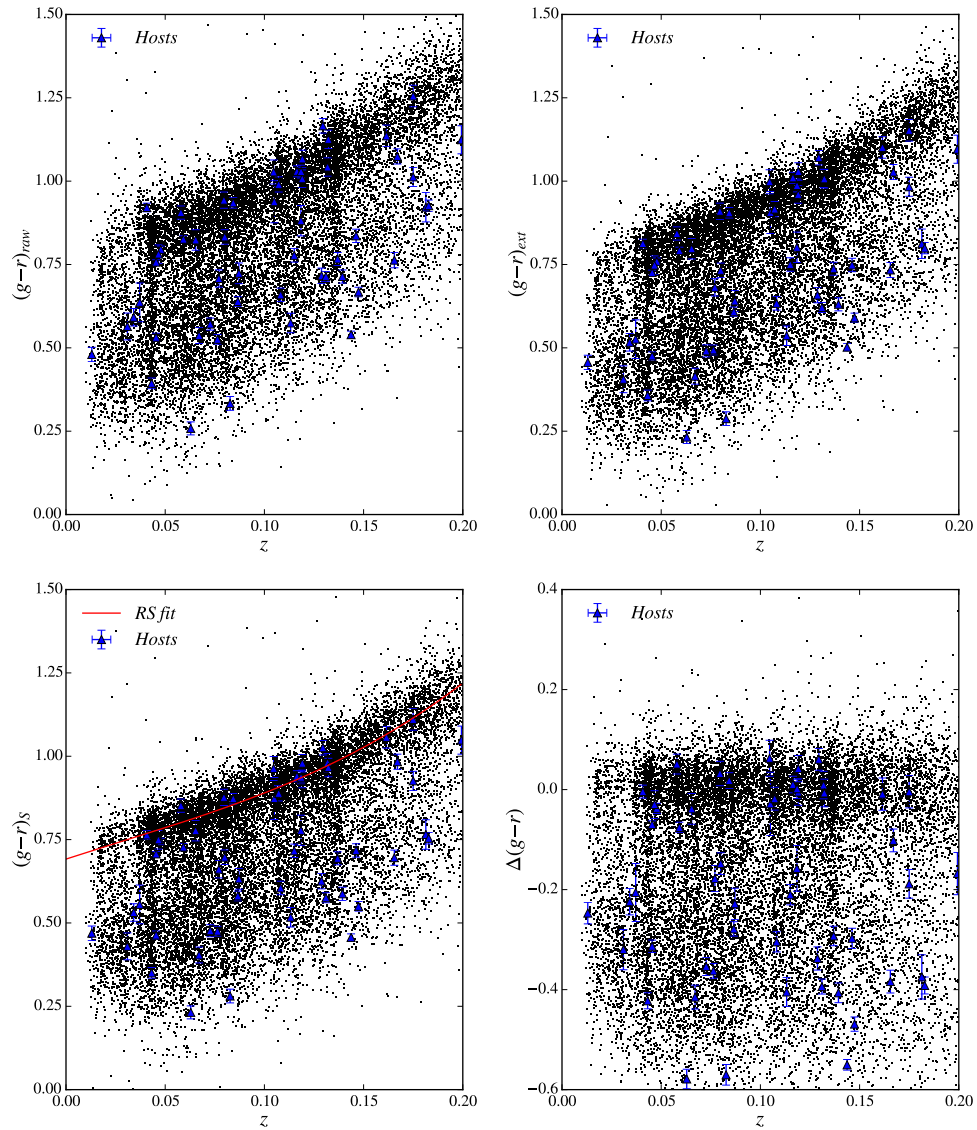
Figure 2.10 Colour-redshift diagrams of the SDSS $g−r$ sample. Top-left and top-right panels: the colours are computed using apparent and galactic extinction corrected magnitudes, respectively. Bottom-left: galactic extinction corrected magnitudes plus a colour correction due to the slope of the red sequence. The red line is the best fit of the red-sequence, obtained via an iterative rejection method. Bottom-right: slope corrected colours relative to the fitted red sequence colour.

2.12). Conversely, bluer colours are indicative of younger populations, which are not strongly affected by the 4000 Å break. This leads to a better agreement between the derived colours of bluer galaxies. The flux decrease at wavelengths shorter than ∼3600 Å (see bottom plots in Fig. 2.12) is caused by H ionization, which also affects young populations. This effect, however, is less significant than the effects of the 4000 Å break.

2.7 Data Usage

The histograms of the control samples in $\Delta(colour)$ space usually present two local maxima. The bluest maximum is defined as the blue cloud peak, and the reddest is the red sequence. The minimum between the two peaks defines the green valley. We use the colours of the green valley and blue cloud peak to construct subsamples in which we apply our models to compare the expected supernova Ia rate with the number of observed SN Ia.

The $\Delta(g - r)$ and $\Delta(u - r)$ values of both the green valley, $\Delta(X - Y)_{GV}$, and the blue cloud, $\Delta(X - Y)_{BC}$, are inferred from Figs. 2.7 and 2.8. The adopted values are: $\Delta(g - r)_{BC} = -0.18$, $\Delta(g - r)_{GV} = -0.12$, $\Delta(u - r)_{BC} = -1.2$ and $\Delta(u - r)_{GV} = -0.25$.

For each control sample, we define a "green valley" subsample, where only objects for which $\Delta_{GV} < \Delta_c < 2 \cdot \sigma_{RS}$ are accepted. As discussed in §1, objects in this colour region should predominantly be early type galaxies, to which our models should be applicable.

In §4 we comment on the applicability of our models to late-type galaxies (see §4.2); to this end we define a "supplementary" subsample, where we relax the blue limit of the accepted $\Delta(colour)$ range to include part of the blue cloud.

2.8 Data Summary

We have characterized our MENeaCS ($g-r$), SDSS ($u-r$ and $g-r$) and SDSS+GALEX ($NUV - r$) control samples in §2.2, 2.3 and 2.4, respectively.

In §2.5 we described our standard procedure to compute $\Delta(colour)$: we calculate the $X - Y$ colour using the galactic extinction- and k-corrected magnitudes and subtract the linearly fitted RS colour from it. We opt to use this procedure, rather than the alternative method described in §2.6, where $\Delta(colour)$ is calculated in redshift
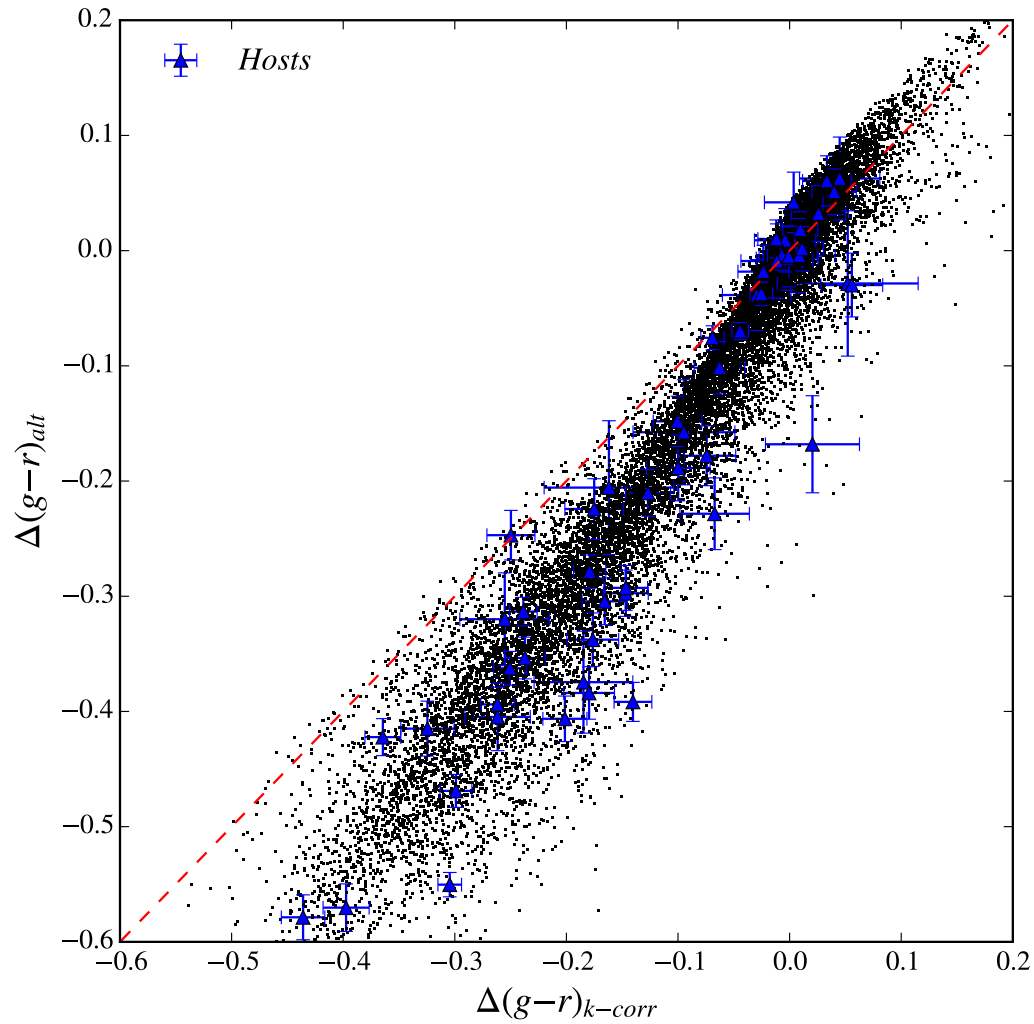
Figure 2.11 Comparison between the colour deviation with respect to the red sequence when derived from two distinct methods. $\Delta(g-r)_{k-corr}$ is computed in the colour–magnitude domain and k-corrections are required. This is the "standard" method used throughout this thesis. $\Delta(g-r)_{alt}$ is calculated in the z-colour parameter space and corresponds to the alternative method. The plotted galaxies belong to our SDSS spectroscopic sample.
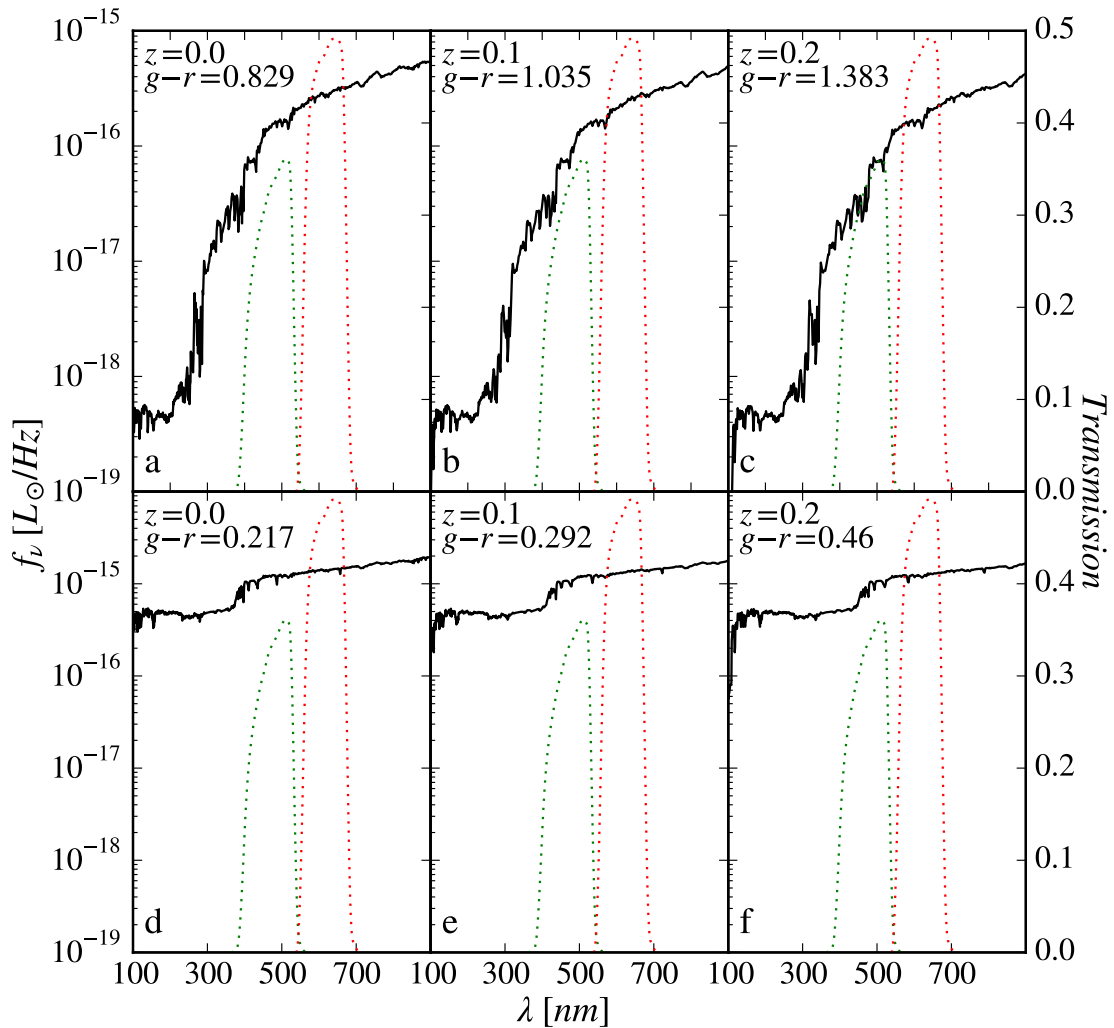
Figure 2.12 Comparison between the typical spectra of an old population (top plots) and young population (bottom plots). The old population is represented by a SSP at 10 Gyr and its spectra at redshifts 0.0, 0.1 and 0.2 are shown in panels *a*, *b* and *c*, respectively. The young population is represented by an exponential SFH with 3 Gyr timescale at ∼2.5 Gyr and its spectra at redshifts 0.0, 0.1 and 0.2 are shown in panels *d*, *e* and *f*, respectively. The specific flux is displayed on a logarithmic scale, while the *g* and *r* filter's transmission (green and red dashed lines, respectively) are shown on a linear scale.

Table 2.3 Subsamples.

Sample	Subsample	$\Delta(X-Y)$ range	Galaxies	Hosts
MENeaCS	Green Valley	$-0.12 < \Delta(g-r) < 0.08$	26746	9
	Suplementary	$-0.4 < \Delta(g-r) < 0.08$	47209	14
SDSS $g-r$	Green Valley	$-0.12 < \Delta(g-r) < 0.08$	10738	28
	Suplementary	$-1.0 < \Delta(g-r) < 0.08$	17550	52
SDSS $u-r$	Green Valley	$-0.25 < \Delta(u-r) < 0.44$	4046	11
	Suplementary	$-1.0 < \Delta(u-r) < 0.08$	10536	29
GALEX+SDSS	Green Valley	$-1.0 < \Delta(NUV-r) < 0.72$	1187	4
	Suplementary	$-3.8 < \Delta(NUV-r) < 0.72$	10085	18

space, because the g filter is very sensitive to k-corrections and the reddest galaxies would be attributed inconsistent colours compared to blue galaxies.

Finally, in §2.7 we characterized the subsamples that will be used to compare the predictions from our models with the observed SN Ia occurrence rates.

Chapter 3

The colour–Supernova model

3.1 Introduction

The quest to understand how SNe Ia explode has grown in importance since their use as standard candles to probe the energy distribution in the universe (Riess et al., 1998; Perlmutter et al., 1999). Their relatively rare occurrence rate and the distance scales involved make it difficult to obtain direct observational evidence of the progenitor system. The two long-standing scenarios are *(i)* the double degenerate (DD) scenario, in which two Carbon-Oxygen white dwarfs (CO WD) merge and the combined mass exceeds the Chandrasekhar mass, leading to an thermonuclear explosion; and *(ii)* the single degenerate (SD) scenario, in which a CO WD stably accretes mass from a main sequence or evolved subgiant companion (Nomoto, 1982b). The fresh material is burned and the effective CO mass eventually reaches the Chandrasekhar limit, leading to an thermonuclear explosion.

An indirect approach to obtain clues as to the progenitor system is to analyze the galaxies that host SNe Ia. Because of the distinct types of stars involved in each channel, the dependence of the SN Ia scenario on the host population is expected to be different. Previous works in this field include Sullivan et al. (2006), Neill et al. (2009) and Milne et al. (2013). In particular, in a work similar to this one, Schawinski (2009) probes the distribution of minimum delay times of SNe Ia using the colours of host galaxies to infer the age of a residual young population (see §1.5). Our work is different in that we take into account the statistical contribution of both the old and residual young populations.

This chapter describes how we built the model that relates the colour of an early-

type galaxy with its SN Ia rate per unit flux. In order to construct this relation we make use of the colour–age and mass-to-light (M/L)–age predictions from the Flexible Stellar Population Synthesis (FSPS) models, combined with various delay time distributions.

A general description of the usage of population synthesis codes is given in §3.2; §3.3 outlines the Star Formation Histories (SFH's) we considered to describe early type galaxies; §3.4 and 3.5 explain the procedure to derive the colour–age and M/L–age relations; §3.6 describes the DTD's that were used and their mapping into the SN Ia channels; §3.7 presents the derived relation between a galaxy's colour and the expected SN Ia rate; and §3.8 summarizes the model construction and applicability.

3.2   Synthetic Population of Stars

One standard procedure in astronomy to assess physical quantities, such as age, of a population of stars is to fit the observational data (colour, magnitude, spectrum) using a synthetic population model. Such analyses can be performed for both resolved (e.g. Li et al. 2014; Mackey et al. 2008; Milone et al. 2009) and unresolved populations (e.g. Trager et al. 2008; van Dokkum & Conroy 2010). Population synthesis models rely on a combination of three main ingredients – stellar evolution code, a spectral library and an initial mass function (IMF).

The stellar evolution codes describe how individual stars of different masses and metallicities evolve in time, tracking their internal structure, elemental abundance and energy output throughout the different evolutionary phases. Quantities such as the density, entropy and temperature profiles are calculated at each time step, providing a complete description of the star's properties. Examples of such codes include Pietrinferni et al. (2004), Marigo & Girardi (2007) and Paxton et al. (2010).

The spectral library uses an atmospheric model to attribute a spectrum to a given star, based on its surface gravity, effective temperature and elemental abundance (e.g. Lejeune et al. 1997, 1998; Falcón-Barroso et al. 2011). Finally, the IMF dictates how the stellar mass of the system is distributed at the formation time. In particular, the shape of this distribution is uncertain at the low mass end ($\lesssim 1 M_{\odot}$) and different formulations have been proposed (e.g. Salpeter 1955; Kroupa 2001; Chabrier 2003).

The most basic model that a population synthesis code can compute is a Simple Stellar Population (SSP), which is a coeval population where all the stars have the same age and metallicity. The integrated spectrum can be calculated by adding the

spectra of all stars, weighted by the IMF. From this, the magnitude can be calculated in a given band, provided that the efficiency curve of the filter is available. The SSP model is representative of a population that is formed through a rapid collapse of a large gas cloud, i.e. instantaneous burst. Composite Stellar Populations (CSP) are computed by convolving the integrated spectrum of a SSP with the Star Formation History (SFH).

Among the many population synthesis codes available (e.g. FSPS - Conroy et al. 2009, 2010; Conroy & Gunn 2010, PEGASE - Le Borgne et al. 2004 and GALAXEV - Bruzual & Charlot 2003) we chose to use FSPS, version 2.4, which allows particular parameters of interest for this study to be changed realistically – for instance, the fraction of stars in the Extended Horizontal Branch, and the metallicity.

3.2.1 FSPS Parameters

The first step in using FSPS is to calculate the evolution in time of the magnitude of an SSP in different filters; this is dependent on a set of general parameters that will remain unchanged throughout this work, unless otherwise stated.

FSPS was set up to use the BaSeL spectral library (Lejeune et al., 1997, 1998; Westera et al., 2002), combined with PADOVA isochrones (Marigo & Girardi, 2007; Marigo et al., 2008) and the Chabrier initial mass function (Chabrier, 2003). We assumed solar metallicity, and no shift in $\log(L)$ and $\log(T)$ for TP-AGB stars; the dust parameters, fraction of blue stragglers (BS), and fraction of EHB stars were all set to zero (some of these assumptions are tested in §3.7.1). The redshift is also set to zero to match our k-corrected samples (see §2.3.2).

3.3 The 2-Burst Population Model

The galaxies in our samples are predominantly early-type galaxies and we model their SFH as a simple old population plus a young burst (referred to herein as a 2-burst or double-burst model and represented by the acronym "2B"). This method has been applied in works attempting to probe episodes of recent star formation (RSF) in order to examine the evolution of early-type galaxies (e.g. Ferreras & Silk 2000; Kaviraj et al. 2007).

Despite the common usage of the 2B model, it has not been shown that it is equivalent to more complex and realistic SFH's for early-type galaxies. For instance,

Kaviraj et al. (2007) claim that, while the 2B model is an oversimplification of the true SFH of early-type galaxies, it can be used to probe whether there has been any recent star formation in these galaxies. Since our models will be used to calculate SN Ia rates, which are sensitive to the age of all the populations that constitute a galaxy, a more careful analysis is required and therefore we check the double-burst predictions against an exponential SFH with 1 Gyr timescale:

$$SFH = \tau \times e^{-t/\tau},$$

(3.1)

where τ is the star formation timescale. By definition, the SFH of a SSP is simply a δ-distribution. As a convention, we reserve the 2 first characters in the SFH label to designate the history type and the remaining characters to specify either the mass fraction (α) in the 2B case or timescale (τ) in the exponential case (e.g. 2B0.01 stands for a 2-burst SFH where the young population contains 1% of the mass[1] of the old population, whereas Ce1.0 represents the exponential SFH with formation timescale of 1 Gyr).

3.3.1 The 2-Burst Model Parameters

In the 2B model context, there are three parameters that determine the properties of a galaxy: the ages of the young and old populations, and the mass fraction of the burst.

In order to construct this model, it is necessary to distinguish between the mass in stars at some time t and the total initial mass of a burst at $t = 0$. The mass in stars changes with time, and is not actually used in our calculations. On the other hand, the total mass includes the mass in stars, gas from mass-loss, and remnants, and by convention is used to calculate absolute supernova rates (SNR; Maoz et al. 2014). We define the mass fraction α as the total initial mass in the young population divided by the total initial mass in the old population (or, equivalently, the ratio of the mass in stars of the old and young populations at their formation time):

$$\alpha \equiv \frac{M_{T_y}}{M_{T_o}},$$

(3.2)

where the subscripts y and o refer to young and old populations, and M_T is total initial mass. It should also be remarked that when we use the term "stars", we are

---

[1]See section 3.3.1 for mass definition.

referring to stars in a nuclear-burning phase, and not remnants such as white dwarfs, neutron stars or black holes.

3.4 Age – Colour Relation

Starting with the FSPS prediction for a $1M_\odot$ single burst, we can calculate the $A - B$ colour of galaxies composed of two populations using:

$$A - B = 2.5 \, log_{10}\left(\frac{10^{-0.4m_{Bo}} + \alpha 10^{-0.4m_{By}}}{10^{-0.4m_{Ao}} + \alpha 10^{-0.4m_{Ay}}}\right), \tag{3.3}$$

where A and B are filters, and m is magnitude. As mentioned before, the age of the old population is assumed to be 10 Gyr; variations of a few Gyr in the age of the old population do not change our model predictions significantly (see §3.7.1).

Fig. 3.1 shows the predictions for $(NUV-r)$, $(u-r)$ and $(g-r)$ as a function of the age of the young population for different values of mass fraction α. The black curves represent a simple population, in other words a limiting case where the α parameter tends to infinity. These curves present two prominent bumps, at $\sim 10^7$ yr (due to the supergiant phase) and $\sim 1.1 \times 10^9$ yr (due to the helium flash). The larger the mass fraction in the young population, the more its colour–age curve resembles the prediction of a SSP (1B). Conversely, the smaller the α parameter, the less relevant the young population is and therefore the more the composite colour will simply resemble the old population – i.e. a constant.

Massive stars can be found in the MS phase for very young populations and these objects are important contributors to the flux at short wavelengths. Therefore, younger populations exhibit bluer colours and, as the population ages towards the red giant phase, the emitted radiation tends to shift towards longer wavelengths. This explains the overall trend seen in Fig. 3.1 that the colours become redder with time. Because the exponential SFH continuously forms new stars, its colour is consistently bluer than the other analysed SFH's.

For the reasons discussed in section 1.4, our observational parameter is the colour difference from the RS, and therefore we offset the model predictions by the computed colour of the SSP at the assumed age of the RS. Eqn. 3.3 therefore becomes
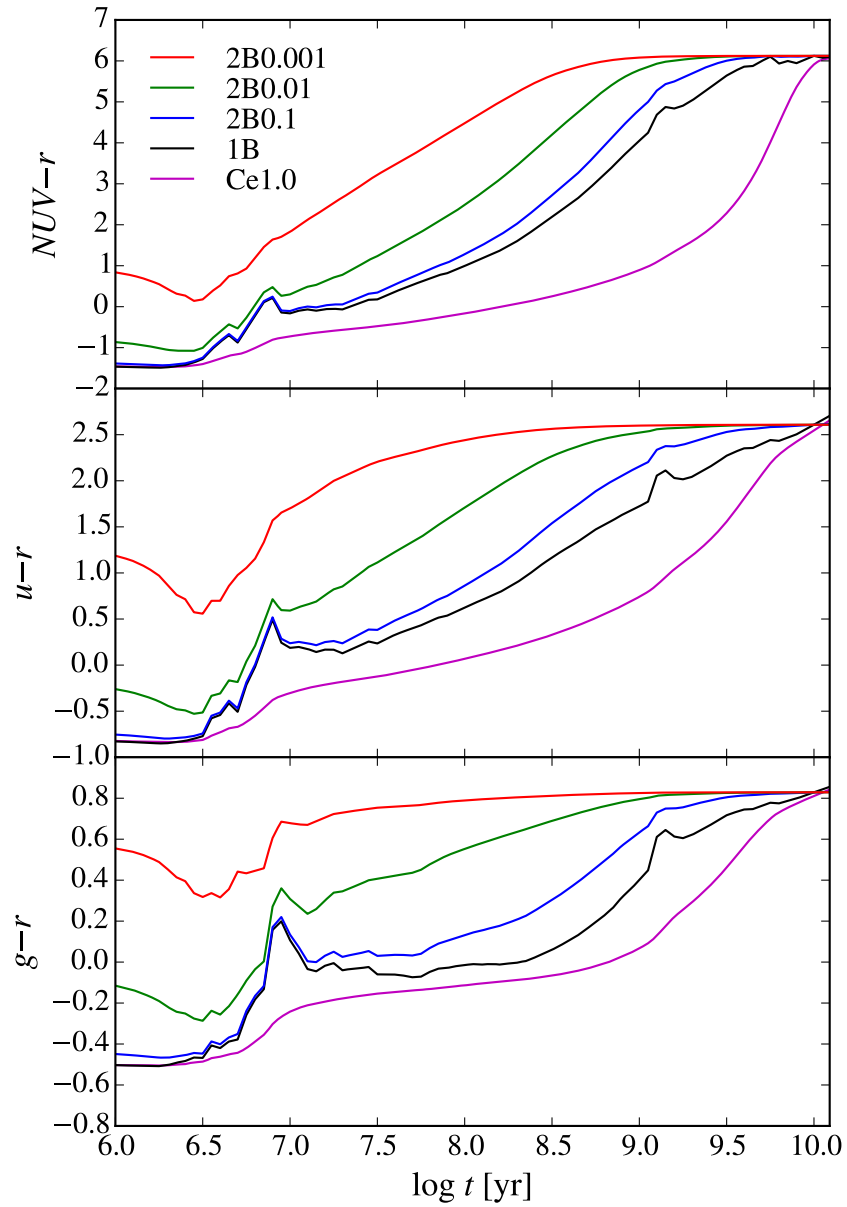
Figure 3.1 FSPS prediction of the colour evolution in time for different star formation histories (coded by line colour; e.g. 2B0.01 stands for a 2-burst SFH where the young population contains 1% of the mass.)

$$(A - B)_{RS} = 2.5 \ log_{10} \left(\frac{10^{-0.4m_{Bo}} + \alpha 10^{-0.4m_{By}}}{10^{-0.4m_{Ao}} + \alpha 10^{-0.4m_{Ay}}} \right) - 2.5 \ log_{10} \left(\frac{10^{-0.4m_{Bo}}}{10^{-0.4m_{Ao}}} \right). \quad (3.4)$$

The offset curves are show in Fig. 3.2. The dotted lines show the offset colours predicted in the full age range, while the superimposed full lines belong to the colour range in which we apply our models. Note that the 1B model in $NUV - r$ is degenerate[2] for $t \gtrsim 4$ Gyr. The same is true for bursts with large mass fractions ($\alpha \gtrsim 0.3$), but such cases can be regarded as unrealistic descriptions of early-type galaxies and therefore we limit the mass fraction used in our analysis to $\alpha \leqslant 0.1$. In principle it is possible to determine the age of the young burst from the age–$\Delta(colour)$ relation derived for a given small mass fraction. However, the slope of this relation is flat at old ages and a slight variation in colour corresponds to a large age range, causing the models to be "effectively" degenerate. In order to avoid this problem, we impose upper limits of -0.05, -0.02 and -0.02 for $\Delta(NUV - r)$, $\Delta(u - r)$ and $\Delta(g - r)$, respectively. Any observed colour greater than the imposed limit is treated separately (see 3.7).

Despite the relatively large age range that cannot be directly inferred from the age–$\Delta(colour)$ relation, the respective colour range is small and because our model relates the colour to SN Ia rates, this effective age degeneracy does not play an important role.

The age–colour relations in Fig. 3.2 also become degenerate if extended to 10^7 yr, because of the effects of supergiants; the degenerate colours are however far smaller than the lower $\Delta(colour)$ limits in which we apply our models, which are defined by the green valley (see 2.7). The constraints and corresponding age limits are shown in Table 3.1.

3.5 Age – M/L Relation

For each SFH considered we can retrieve a relation between the total mass and the composite flux of the synthetic population. The flux can be computed for any filter; we use the r band and adopt a solar absolute magnitude $M_{r,\odot} = +5$ for the conversion:

---

[2]Meaning that the age cannot be inferred from the $\Delta(colour)$.
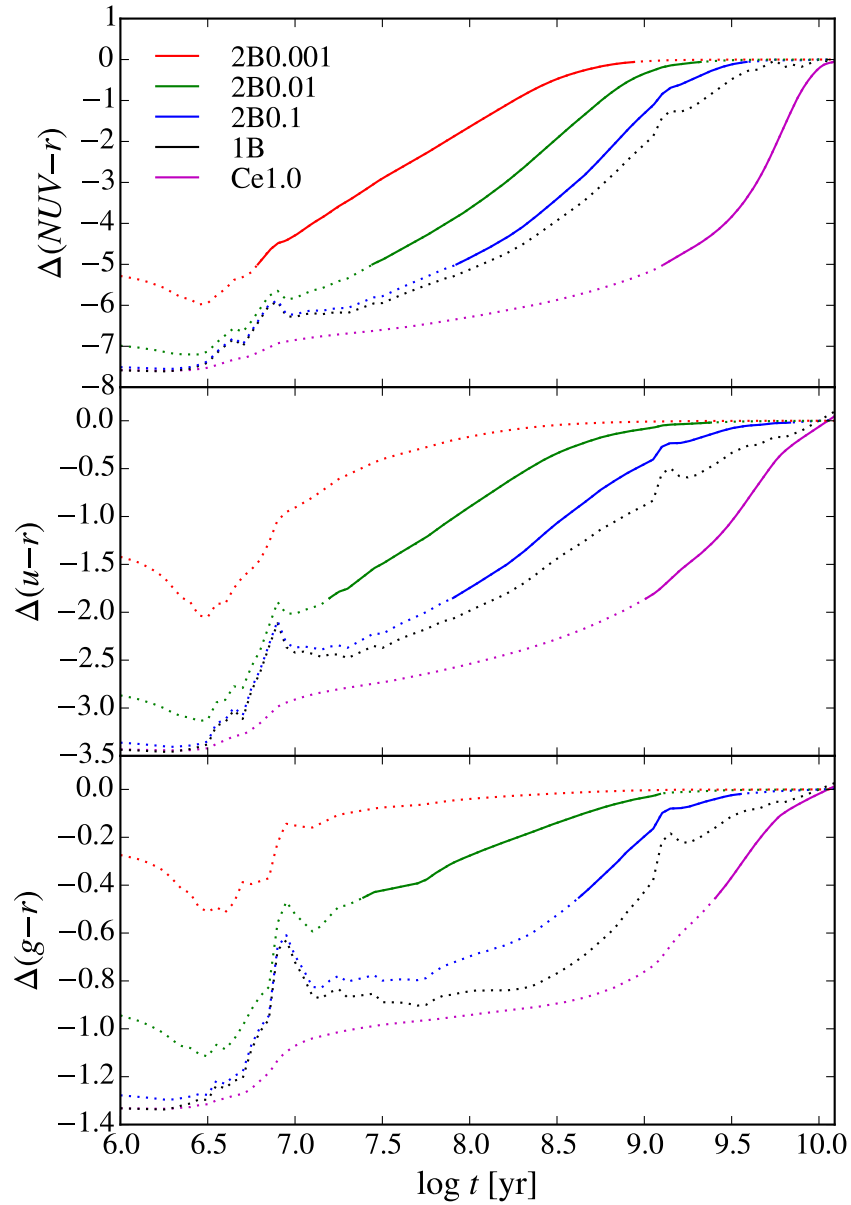
Figure 3.2 Relation between t and $\Delta(colour)$ for different SFH's. The dotted lines show the predictions of FSPS in the full age range, while the superimposed full lines corresponds to the colour ranges in which the age of the young population can be directly inferred.

Table 3.1 Colour parameters.

$\Delta(colour)$	SFH	$\Delta(colour)$	t [Gyr]
	Green Valley sample		
$\Delta(NUV - r)$	$2B0.1$	$(-1.0, -0.06)$	$(1.18, 3.83)$
	$2B0.01$	$(-1.0, -0.06)$	$(0.57, 2.09)$
	$2B0.001$	$(-1.0, -0.06)$	$(0.18, 0.87)$
	$Ce1.0$	$(-1.0, -0.046)$	$(7.41, 12.59)$
$\Delta(u - r)$	$2B0.1$	$(-0.25, -0.02)$	$(1.34, 6.71)$
	$2B0.01$	$(-0.25, -0.02)$	$(0.42, 2.34)$
	$Ce1.0$	$(-0.25, 0.06)$	$(7.07, 12.59)$
$\Delta(g - r)$	$2B0.1$	$(-0.12, -0.02)$	$(1.21, 3.48)$
	$2B0.01$	$(-0.12, -0.02)$	$(0.38, 1.22)$
	$Ce1.0$	$(-0.12, 0.017)$	$(5.79, 12.59)$
	Supplementary sample		
$\Delta(NUV - r)$	$2B0.1$	$(-3.8, -0.06)$	$(0.24, 3.83)$
	$2B0.01$	$(-3.8, -0.06)$	$(0.09, 2.09)$
	$2B0.001$	$(-3.8, -0.06)$	$(0.01, 0.87)$
	$Ce1.0$	$(-3.8, -0.046)$	$(3.22, 12.59)$
$\Delta(u - r)$	$2B0.1$	$(-1.0, -0.02)$	$(0.35, 6.71)$
	$2B0.01$	$(-1.0, -0.02)$	$(0.08, 2.34)$
	$Ce1.0$	$(-1.0, 0.06)$	$(3.32, 12.59)$
$\Delta(g - r)$	$2B0.1$	$(-0.4, -0.02)$	$(0.51, 3.48)$
	$2B0.01$	$(-0.4, -0.02)$	$(0.04, 1.22)$
	$Ce1.0$	$(-0.4, 0.017)$	$(2.93, 12.59)$

$$f_r \equiv L_r/L_{r,\odot} = 10^{-0.4(M_r-5.0)}, \tag{3.5}$$

where f_r is the flux in the r band in solar luminosities.

For the 2-burst case, given a 1 $M_\odot$ old population, the aggregate total mass is simply $(1 + \alpha)$ $M_\odot$ and the M/L is computed via:

$$M_T/L_\star = \frac{1+\alpha}{\alpha \cdot f_r(t_y) \ + \ f_r(t_o)}. \tag{3.6}$$

In the exponential SFH case, for a total formed mass of 1 $M_\odot$, the total mass as function of time is simply $1 - e^{-t/\tau}$ and the M/L is given by:

$$M_T/L_\star = \frac{1 - e^{-t/\tau}}{f_r(t)}. \tag{3.7}$$

Fig. 3.3 shows the age–M/L relation for the different SFH scenarios. As expected, the redder SFH's, i.e. with larger fractions of old population (i.e. 2B0.001 and 2B0.01), present a higher M/L ratio. Note that the smaller M/L prediction for an exponential SFH is consistent with the bluer colours predicted for this SFH in comparison with the double bursts, as shown in Fig. 3.1.

3.6   Age – Supernova Rate Relation

3.6.1   The Delay Time Distribution

The delay time distribution is defined as the rate of SN Ia per unit mass[3] for a SSP. Distinct SN Ia channels (e.g. SD and DD) are expected to exhibit DTD's with different behaviors according to theoretical predictions (Greggio, 2005; Mennekens et al., 2010; Claeys et al., 2014).

A thorough description of the characteristics of the DTD for SNe Ia is presented in Maoz et al. (2014). We summarize here the most relevant parts of this discussion.

Both the single and double-degenerate channels are affected by the time required to form the first WD's. Stars more massive than $\sim 8M_\odot$ end their lives as either black holes or neutron stars after a core collapse supernova, and therefore no WD's are created (Heger et al., 2003). The limiting mass $8M_\odot$ corresponds to a main sequence lifetime of ~ 40 Myr (t_{WD}). Hence SSP's younger than this age limit cannot host

---

[3]As discussed in section 3.3.1, this mass includes stars, gas and remnants.
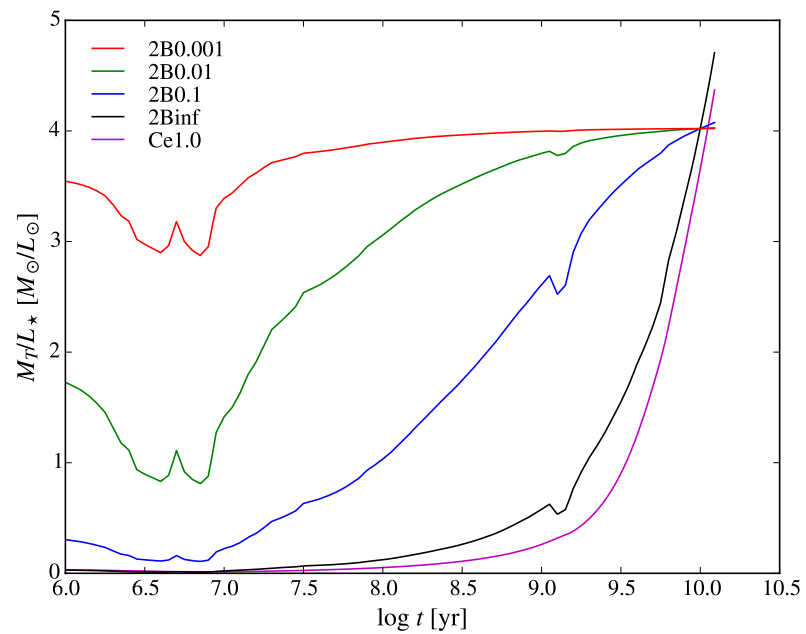
Figure 3.3 FSPS prediction of the mass to light ratio as a function of age. The mass here is the total mass and the light corresponds to the flux obtained from the magnitude in the r band.

SNe Ia: $DTD(t < t_{WD}) = 0$. Whether any SNe Ia can occur promptly after this time limit depends on the minimum assumed merging time in the DD scenario and on the exact treatment of mass transfer in the SD scenario.

It should be noted that $\gtrsim 7M_\odot$ stars are more like to form ONe rather than CO White Dwarfs (Poelarends et al., 2008). ONe WD's, however, are not expected to lead to a SN Ia and therefore $t_{WD} = 50$ Myr would be a more realistic assumption than the adopted value of 40 Myr. We have tested our models with both t_{WD} ages and the conclusions remained unchanged.

Another feature shared between both channels is the timescale t_c, set by the lowest mass that the progenitor of a CO WD can have in a binary system. According to Greggio (2005), stars less massive than $2M_\odot$ are more likely to evolve into a Helium WD rather than CO WD. During the helium flash, the primary's radius expands significantly, increasing up to a few hundreds of $R_\odot$ (see Fig. 3.4). Unless the binary separation is large enough ($\gtrsim 400R_\odot$), the secondary accretes mass from the primary and truncates its evolution. In this case, a He WD rather than a CO WD is formed, and hence no SN Ia explosion will occur. The lower mass constraint of $2M_\odot$ corresponds to a main sequence lifetime of $t_c \sim 1.1$ Gyr. The implications of this timescale for the DD and SD are channels are discussed below.

The shape of the DTD in the DD scenario is defined by a variety of factors, including the distributions of the separation and mass ratio between the two WD's. Delay times predicted by binary population synthesis simulations can be somewhat different, depending on the underlying assumptions. However, a common feature is that the predicted DTD will follow a power law with -1 index for $t > t_c$ (Maoz et al., 2014). This behavior is mainly determined by the time required to shrink the separation between the WD's via the emission of gravitational waves. Therefore, even if no CO WD's are formed at ages older than t_c, the DD channel still predicts that supernovae can occur in very old populations.

We employ two DTD's as proxy of the DD scenario. The first case assumes that the behavior of the DTD remains unaltered for $t \geq t_{WD}$, i.e., $DTD(t) = 0$ for $t < t_{WD}$ and $DTD(t) \propto t^{-1}$ for $t \geq t_{WD}$. In the second case we adopt the prediction from van Kerkwijk et al. (2010), where the DTD at $t_{WD} < t < t_c$ is dominated by the shallower power law of the formation rate of WD's, $t^{-0.5}$ (Pritchet et al., 2008). In summary, $DTD(t) = 0$ for $t < t_{WD}$, $DTD(t) \propto t^{-0.5}$ for $t_{WD} \leq t < t_c$ and $DTD(t) \propto t^{-1}$ for $t \geq t_c$.

The DTD representative of the SD scenario may, according to some authors, be
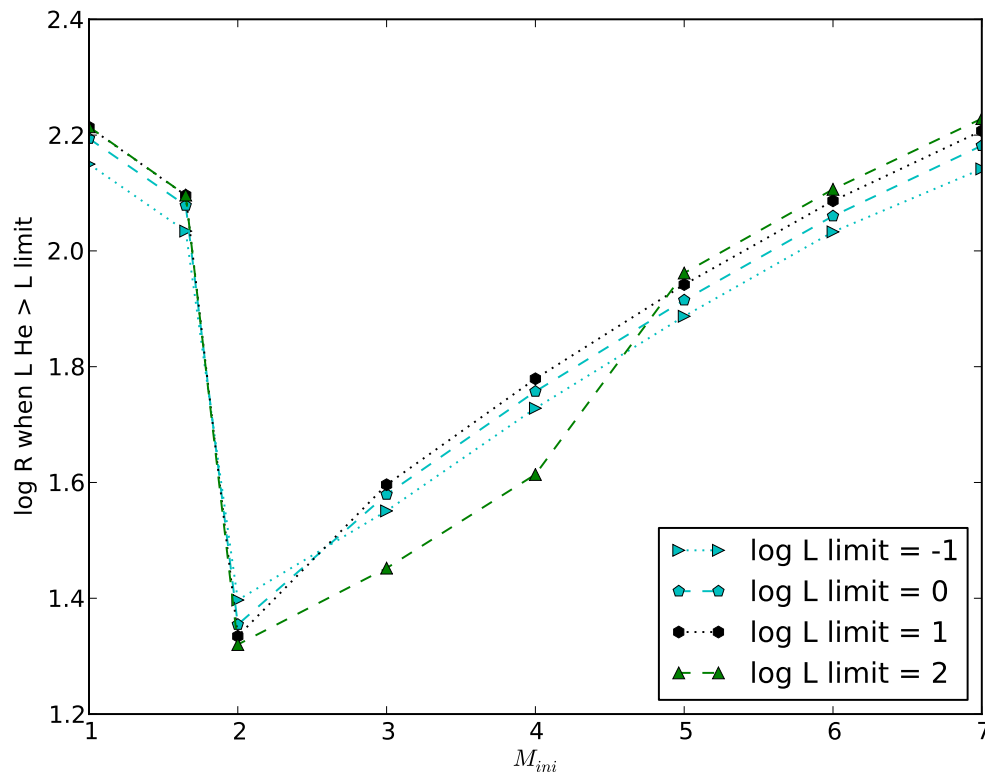
Figure 3.4 Stellar radius at the core helium flash time. The radii are shown as function of the intial stellar mass and for different luminosity limits. The plotted values were computed using the MESA code (Paxton et al., 2010). From Herwig (2015, private communication).

characterized by a sharp cutoff. One explanation is simply that the SD channel cannot produce any SN Ia at $t > t_c$, because after the CO WD is formed, the time required for mass accretion from the secondary is relatively short. Thus the SN Ia occurrence would cease when the production of new CO WD's in binary systems stops.

Another mechanism that constrains the age of the progenitor system in the SD channel is discussed by Maoz et al. (2014) (first published by Nomoto 1982b). The accretion rate onto the WD needs to be in a narrow range, so that the accreted material undergoes stable burning, thus increasing the CO mass of the WD until it reaches the Chandrasekhar limit. This particular accretion rate range happens only for $2 - 3M_\odot$ donors that are on the main sequence or slightly evolved subgiant phase. This would place both an upper and lower age constraint on the DTD: $350\mathrm{Myr} \lesssim t \lesssim 1.1\mathrm{Gyr}$. A variety of power laws (and more complex functions) have been proposed for the DTD of the SD channel.

A compilation of theoretical DTD's for both the SD and DD scenarios is shown in Fig. 3.5 from Maoz et al. (2014). Note the fair agreement of the slope and "turn-on" time for the DD DTD's, and the discrepancy of the same for the SD DTD's. In fact, SD population synthesis models are in very poor agreement with each other, often differing by a factor of $1000\times$ or more.

Because the DTD's associated with the different SN Ia channels have different features, such as the strength of the cutoff at $\sim 1 - 2\mathrm{Gyr}$, it is in principle possible to determine which channel is more likely to occur by assessing which DTD is in better agreement with the observational data.

3.6.2   The DTDs Used in This Work

The minimum age at which a population can host a SN Ia is t_{WD}. The DTD is assumed to be $\propto t^{s_1}$ for $t_{WD} < t < t_c$, and $\propto t^{s_2}$ for $t > t_c$. The DTD segments are normalized so that the DTD is continuous at t_c. The normalization constant for $t < t_c$ is determined from the condition $DTD(5 \times 10^8 yr) = 10^{-12.2} SNe\ M_\odot^{-1}\ yr^{-1}$. This condition is approximate only, and comes from Sullivan et al. (2006). The overall normalization does not affect the results that we discuss.

Following the discussion presented in §3.6.1, we consider 5 cases: *(i)* a soft break $s_1 = -0.5, s_2 = -1$ (hereafter "-0.5/-1"); *(ii)* a constant power slope $s_1 = s_2 = -1$ ("-1/-1"); *(iii)* a constant power slope $s_1 = s_2 = -1.5$ (-1.5/-1.5); *(iv)* a break $s_1 = -1, s_2 = -2$ (-1/-2); and *(v)* a drastic cutoff $s_1 = -1, s_2 = -\infty$ $(-1/-\infty)$.
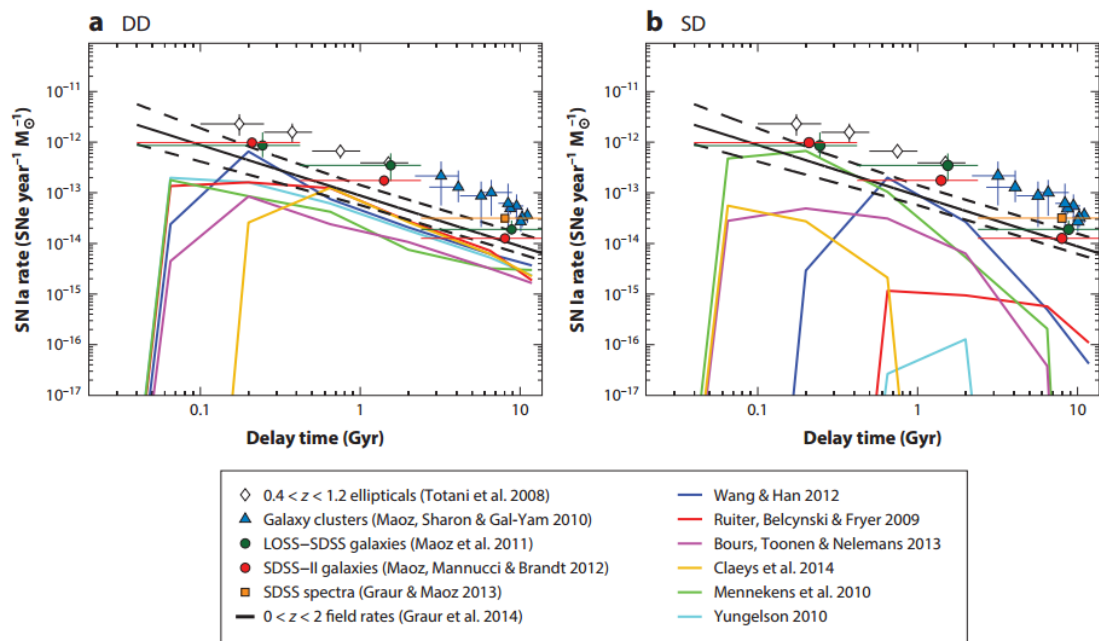
Figure 3.5 Compilation of delay time distributions from Maoz et al. (2014). The DTD's proposed for the DD channel are shown in panel *a* and for the SD channel in panel *b*. The markers and black lines represent observational data. The reference box is from the original figure. The solid lines are based on detailed population synthesis models.
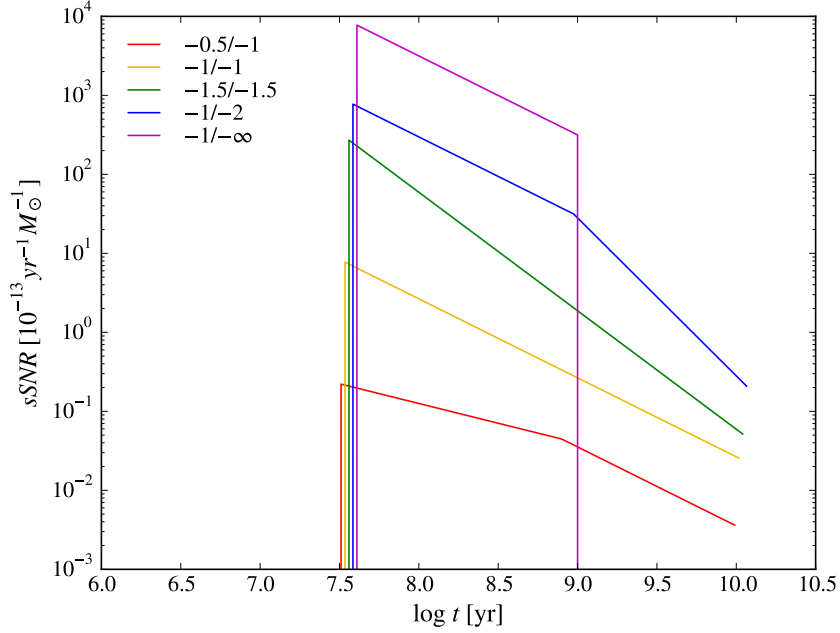
Figure 3.6 The delay time distributions considered in this work. The curves are separated for clarity; the overall normalization of the curves does not affect the results.

These cases are shown in Fig. 3.6 and detailed in Table 3.2.

Table 3.2 Power law indexes and age timescales of the delay time distributions.

DTD Alias	t_{WD} [Myr]	t_c [Gyr]	s_1	s_2
-0.5/-1	40.00	1.00	-0.5	-1.0
-1/-1	40.00	1.00	-1.0	-1.0
-1.5/-1.5	40.00	1.00	-1.5	-1.5
-1/-2	40.00	1.00	-1.0	-2.0
$-1/-\infty$	40.00	1.00	-1.0	$-\infty$

Although the exact age limits derived from mass constraints depend on the stellar evolution model, we adopted the same t_{WD} and t_c for all DTD's because of the common physical motivations that lead to these ages. For instance, a 2 $M_\odot$ star has a main sequence lifetime of $\sim$1.1 Gyr. This is according to the relation

$$\log t = 0.825 \log^2(M/120) + 6.43, \qquad (3.8)$$

which was fit by Buzzoni (2002) and holds for solar metallicity stars.

3.6.3   The Specific Supernova Rate

The specific supernova rate (sSNR) is the rate of SNe Ia per unit mass[4]; it is derived from the convolution product of the SFH and the delay time distribution:

$$sSNR(t) \;=\; [SFH * DTD](t). \tag{3.9}$$

This is valid under the assumption that the DTD itself is independent of SFH. For instance, if the DTD is affected by the metallicity parameter, then the SN Ia rate from younger populations will follow a different DTD and the convolution does not hold.

In the 2-burst context, the combined contribution from the young and old populations is simply

$$sSNR = \frac{sSNR_o + \alpha \cdot sSNR_y}{1 + \alpha}. \tag{3.10}$$

The sSNR for the exponential SFH can be obtained by using Eqn. 3.9.

The composite sSNR's are shown in Fig. 3.7. Note that in the case of the sharp cutoff at 1 Gyr, the sSNR before 40 Myr and after 1 Gyr is zero, because the old population makes no contribution to the composite $sSNR$. In the other cases there is always a residual contribution from the old population and $sSNR(t < t_{WD}) = sSNR(10Gyr)/(1+\alpha)$. Note also that the smaller the mass fraction, the smaller the $sSNR$ break at 40 Myr; this happens because the constant contribution from the old population dominates the composite $sSNR$ for small α's.

3.7   Colour – SNR Relation

The age of the young population cannot be inferred for $\Delta(colour)$'s larger than the adopted upper limits (see §3.4 and Table 3.1). This affects the $\Delta(Colour)$–sSNR relation. For the 2B model we treat this colour region in two different ways: *(i)* to any $\Delta(colour)$ redder than the upper limit, we attribute the sSNR predicted for the old population. Note that, since we assume the age of the old population to be 10 Gyr, we do not need to infer it from the age–$\Delta(colour)$ relation and therefore the sSNR at $\Delta(colour) \;=\; 0$ can be easily calculated. *(ii)* We linearly extrapolate the $\Delta(colour)$–

---

[4]As discussed in section 3.3.1, this mass is *by convention* the total mass and includes stars, gas and remnants.
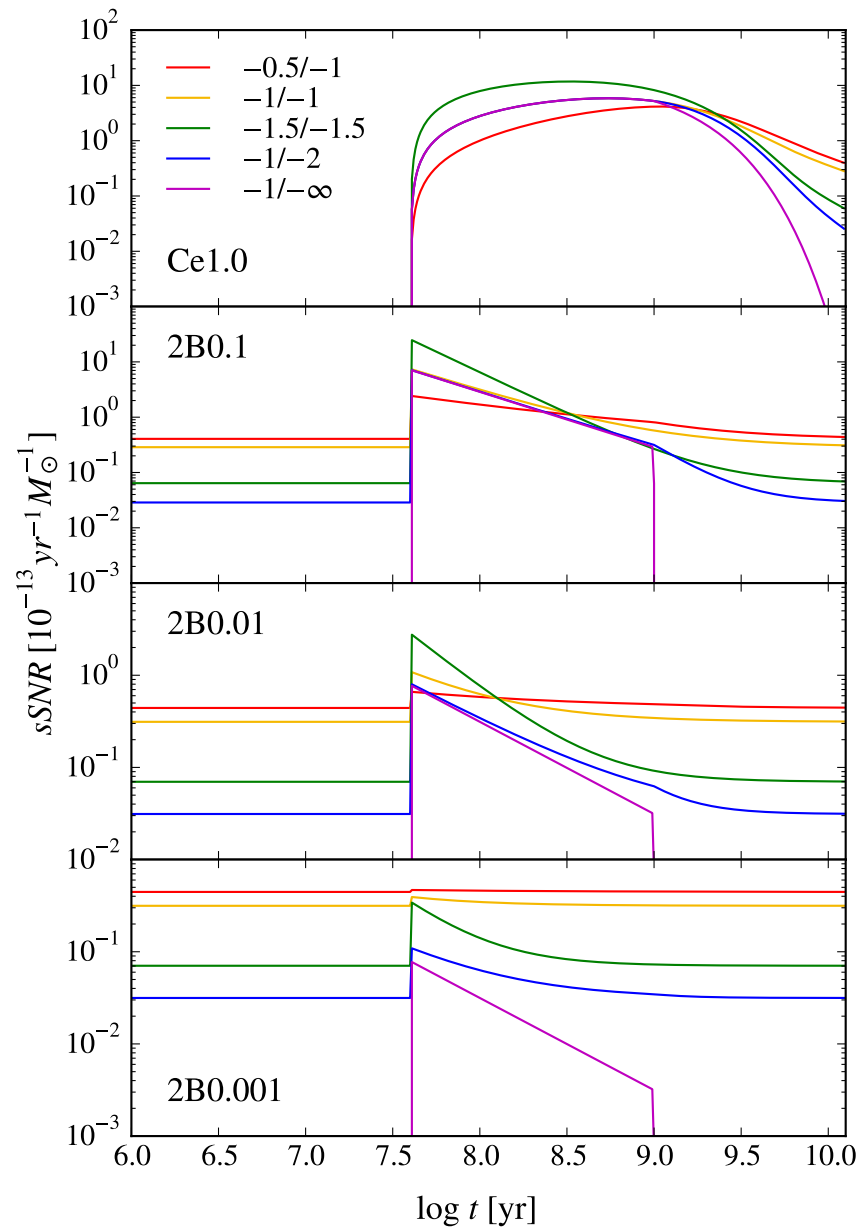
Figure 3.7 Composite SN Ia rate per unit mass as a function of time for the DTD's considered. Each panel shows the sSNR prediction for one particular SFH.

SNR relation between the points at which $\Delta(colour)$ is the upper limit and zero; the sSNR predicted for the old population is attributed to positive $\Delta(colour)$'s. The choice of procedure does not strongly influence our results. The sSNR dependence on $\Delta(u-r)$ is shown in Fig. 3.8.

The exponential SFH models are treated in a slightly different manner. This is because the predicted colour at 10 Gyr is not necessarily zero, since the offset is computed with respect to the colour of the SSP at 10 Gyr. Moreover, the age of the young population can be inferred from the colour–age relation, even at old ages. We adopt a colour limit that corresponds to the colour computed at ∼12.6 Gyr. The sSNR$_L$ is assumed constant for any colour redder than this limit.

To calculate the supernova rate of an observed galaxy, one needs to express the specific supernova rate in terms of luminosity rather than mass. The relation between $\Delta(colour)$ and sSNR$_L$ can be obtained by multiplying the $sSNR(t)$ by $M_T/L_\star(t)$ and substituting the age dependence of these quantities by colour using the $Age - \Delta(colour)$ relation, i.e.

$$SNR_L(\Delta) = sSNR(t(\Delta)) \cdot M/L(t(\Delta)), \qquad (3.11)$$

where $\Delta \equiv \Delta(colour)$.

Fig. 3.8 shows the dependence of the sSNR with $\Delta(u-r)$. Note that the sSNR predicted for a given DTD is consistent (within one order of magnitude) between different SFH's. This happens because there is an interplay between the mass fraction and the age of the young population. For instance, a measured $\Delta(colour)$ can be explained by either a small fraction of a very young population, which has a high individual sSNR but relatively small contribution to the composite sSNR, or a large mass fraction of a older young population, which presents a lower individual sSNR, but is more significant to the composite sSNR.

Other features of the $\Delta(colour)$–sSNR relation are common to the $\Delta(colour)$–SNR$_L$ relations; these are shown for $\Delta(NUV-r)$, $\Delta(u-r)$ and $\Delta(g-r)$ in Figs. 3.9, 3.10 and 3.11, respectively.

While the composite sSNR curves cover an order of magnitude, the predicted sSNR$_L$ values are usually within a factor of 2–3 for any DTD considered. Moreover, the $-1/-1$ and $-0.5/-1$ DTD's present a nearly constant $\Delta(colour)$–sSNR$_L$ relation for both the double-burst and exponential SFH's. In fact, the flatness of these curves remain true for colours much bluer than the green valley threshold (see Fig. 3.12).

These features were not expected *a priori*, and can provide meaningful insight into the rate of SNe Ia. The following statement summarizes this finding:

For a delay time distribution like

$$\text{DTD}(t) = 0 \text{ for } t < t_{WD},$$
$$\text{DTD}(t) \propto t^{-1} \text{ for } t \geq t_{WD},$$

convolved with star formation histories representative of early type galaxies, the expected supernova Ia rate per unit r-band flux is nearly constant and independent of Δ, where Δ is the $\Delta(colour)$ of an early type galaxy.

Furthermore, if for $\Delta > \Delta_{GV}$ the galaxy sample follows a flat distribution in luminosity space, then the absolute Supernova Ia rate maps the sample number distribution in Δ space.

The two main reasons that lead to further convergence of the sSNR$_L$ for our SFH's are: *(i)* the colour range that covers the RS is small and therefore the corresponding age range is relatively short (see Table 3.1); *(ii)* more importantly, the $M_T/L_\star$ ratio scaling is opposite to the sSNR scaling, i.e. while the $M_T/L_\star$ increases as the age increases, the sSNR decreases as age increases. It should be noted the flatness of the $\Delta(colour)$–sSNR$_L$ relation holds for colours bluer than the green valley colour.

Another particular feature in the $\Delta(colour)$–SNR relation is the abrupt change in slope for the double-burst model with $\alpha = 0.1$ (2B0.1). This is ultimately related to the ~ 1.1 Gyr bump present in the age–colour relation for a SSP (see Fig. 3.2), which is caused by the low mass stars reaching the tip of the RGB phase and undergoing a helium flash in their cores. Among the mass fractions we considered, only $\alpha = 0.1$ has a young burst that is strong enough to be susceptible to this effect.

In the $-1/-\infty$ case, the residual SNR contribution from the old population is zero because it is older than the cutoff in the DTD. If the young population is also older than this cutoff, then the SNR is zero. The $\Delta(colour)$ corresponding to the cutoff age (hereafter $\Delta_{c,\alpha}$) depends on the assumed mass fraction in the double-burst model and any $\Delta(colour)$ redder than $\Delta_{c,\alpha}$ corresponds to a null SNR, i.e. SNR$(\Delta_\alpha) = 0$ for all $\Delta > \Delta_{c,\alpha}$. For instance, $\Delta(u-r)_{c,0.1} \approx -0.48$ and $\Delta(u-r)_{c,0.01} \approx -0.1$. Note also that as the mass fraction becomes smaller, the cutoff colour becomes redder. This is to be expected, since for two distinct composite populations for which the young populations are at the same age, the composite population with a smaller
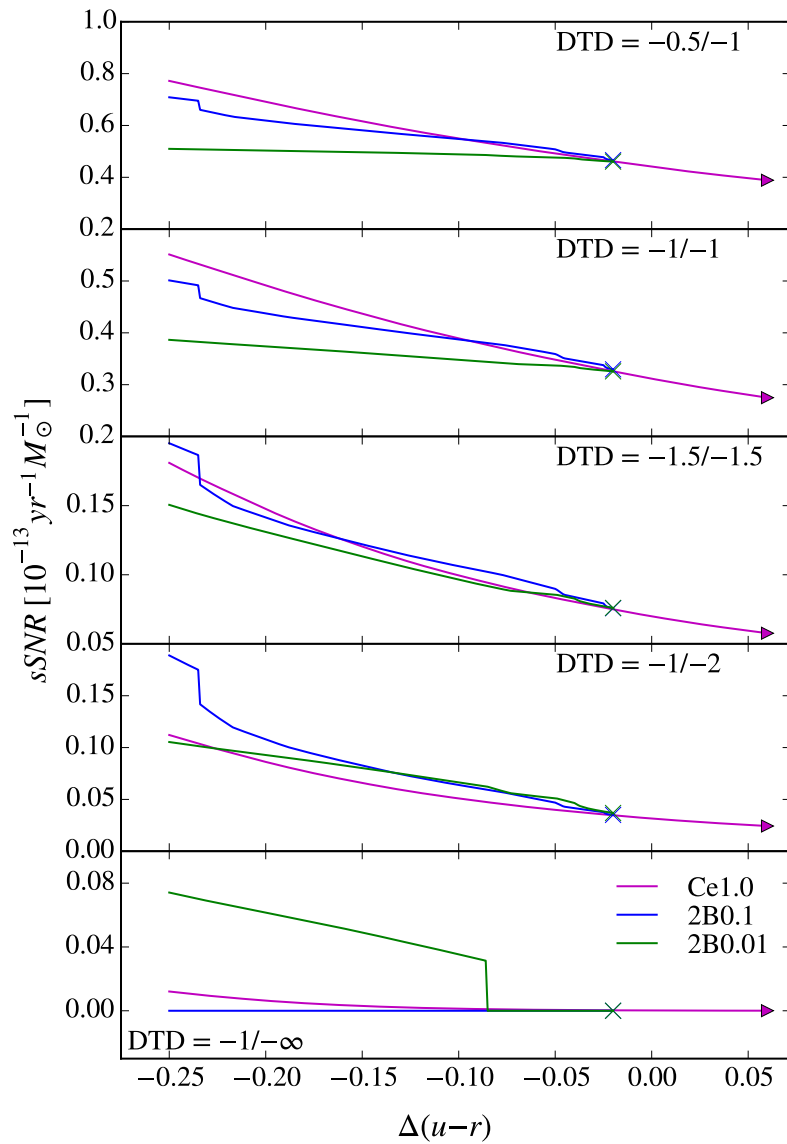
Figure 3.8 Supernova rate per unit mass as a function of $\Delta(u - r)$. The crosses indicate the $\Delta(u - r)$ upper limits. Some crosses may lie on top of each other.
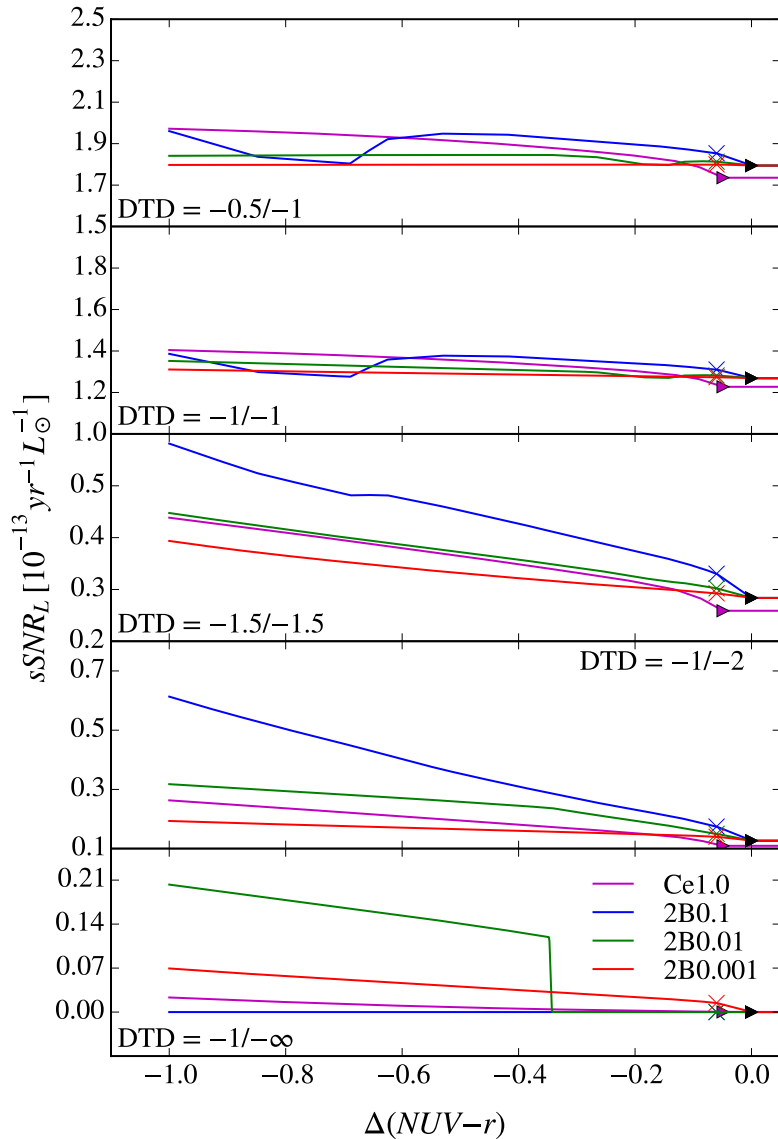
Figure 3.9 Supernova rate per solar luminosity as a function of $\Delta(NUV - r)$. The crosses indicate the $\Delta(NUV-r)$ upper limits. The age of the young population cannot be directly inferred from the age–$\Delta(colour)$ relation for colours redder than this limit. Some crosses may lie on top of each other. The sSNR$_L$ is linearly extrapolated between the cross and right triangle markers (the latter are placed at 10 Gyr for 2B models and 12.6 Gyr for the exponential SFH model). The sSNR$_L$ is assumed to be constant at colours redder than the colour demarcated by the triangles. The black triangle is placed at the $\Delta(colour)$ of the RS (i.e. zero) and is common to all 2B models.
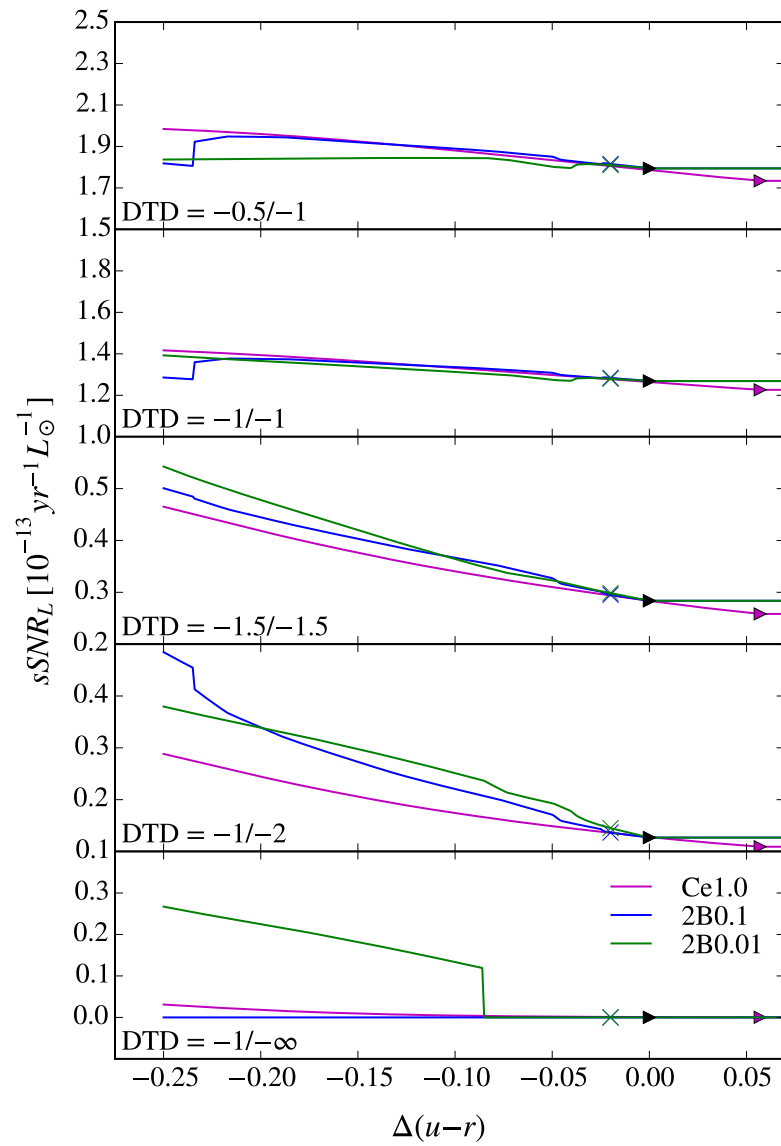
Figure 3.10 Same as Fig. 3.9 but for $\Delta(u-r)$.
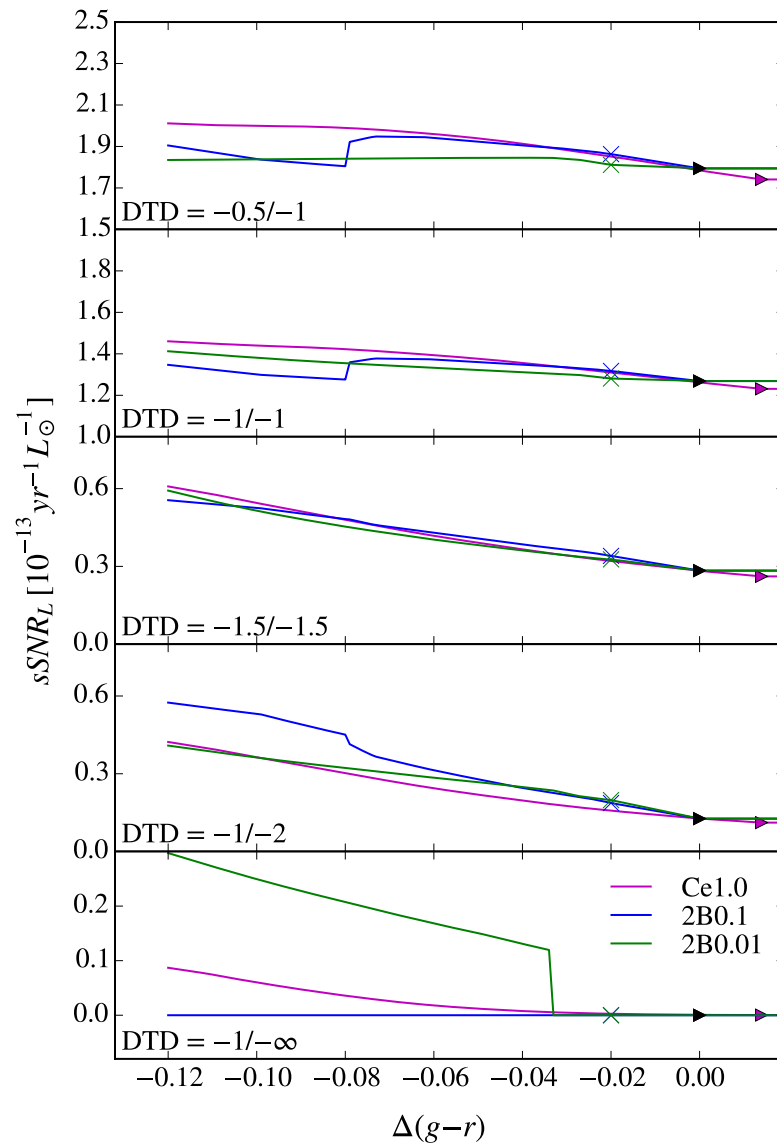
Figure 3.11 Same as Fig. 3.9 but for $\Delta(g - r)$.
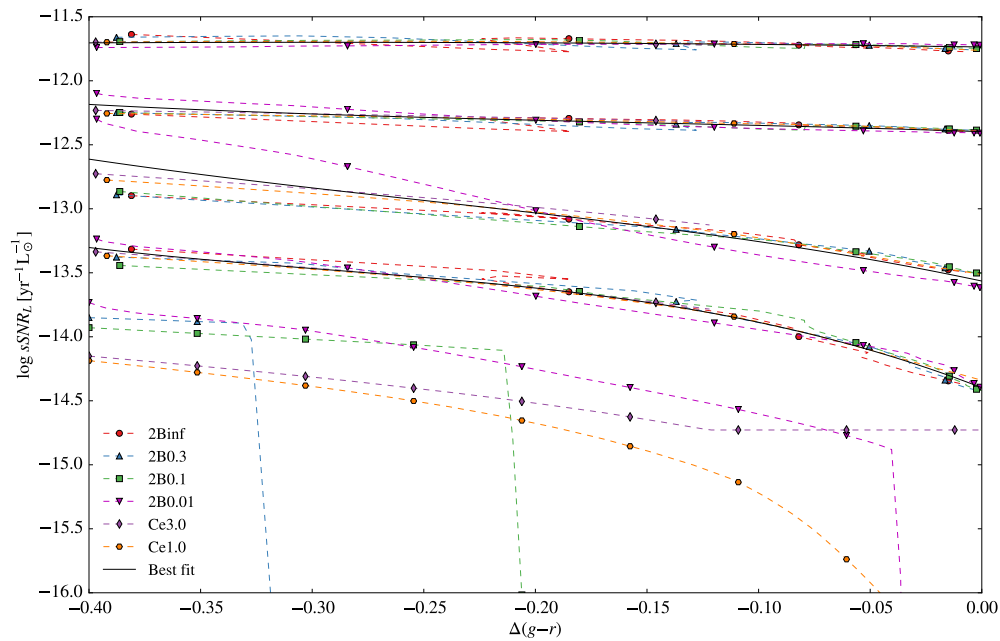
Figure 3.12 $\Delta(g-r) - SNR_L$ relation shown in an extended range. The colour is coded to represent different SFH's. Each group of lines indicate a DTD; from top to bottom $-0.5/-1$, $-1/-1$, $-1.5/-1.5$, $-1/-2$ and $-1/-\infty$. The full black lines are the best fit for each DTD. No fit is attempt for the $-1/-\infty$ case. The predictions have been shifted vertically to minimize the standard deviation of best fit. This does not influence the results because we compare normalized rates. No treatment was necessary for colour degeneracies.

mass fraction of young stars is redder. In other words, $\Delta_{c,\alpha_2} < \Delta_{c,\alpha_1}$ if $\alpha_2 < \alpha_1$. In the limit that the mass fraction in the young population becomes negligible (so that the composite population is predominantly old), the colour break approaches the RS colour (i.e. zero) and its SNR contribution before the break also tends to zero because of its low mass:

$$\lim_{\alpha \to 0} \Delta_{c,\alpha} = 0 \,, \tag{3.12}$$

$$\lim_{\alpha \to 0} SNR(\Delta < \Delta_{c,\alpha}) = 0 \,. \tag{3.13}$$

In particular, note that because $g - r$ is the less sensitive colour to young populations, the 10% break is redder than the adopted range, $\Delta_{c,0.1} < -0.12$.

3.7.1 Tests of the Stellar Population Models

To test the results from FSPS, we used PEGASE.2 (Fioc & Rocca-Volmerange, 1997, 1999) models to produce age–colour and age–luminosity relations for simple bursts. (PEGASE models use the older Padova evolutionary tracks coupled with the BaSeL (Lejeune et al., 1997, 1998) spectral library). The results were almost identical to FSPS, even for the GALEX NUV filter (see Fig. 3.13).

We also verified that our model is not strongly dependent on metallicity, fraction of stars on the EHB, fiducial age of the old population, or IMF parameters. We show in Fig. 3.14 how one representative scenario – a double-burst with $\alpha = 0.01$, $-1/-1$ DTD, observed in $\Delta(u - r)$ – is influenced by changes in each of several parameters, while keeping others invariant. The standard model uses the parameters described in §3.2.1 and corresponds to the black curves. The vertical scale is kept invariant so that the order of magnitude of the sSNR$_L$ change can be readily assessed. The net effect for any of the changes can be very well approximated by an offset in the (nearly constant) sSNR$_L$.

Since the slope of the age–colour relation (see Fig. 3.2) is nearly flat at old ages for the double-burst models, the colour of the old population is only weakly influenced by variations in the age of the old population, and therefore the composite colour versus age curves remain nearly unaltered. The composite sSNR vs. age function, on the other hand, is in general more affected by this parameter. In the $-1/-1$ case, in which the slope is flatter at old ages, the old population sSNR changes by less than
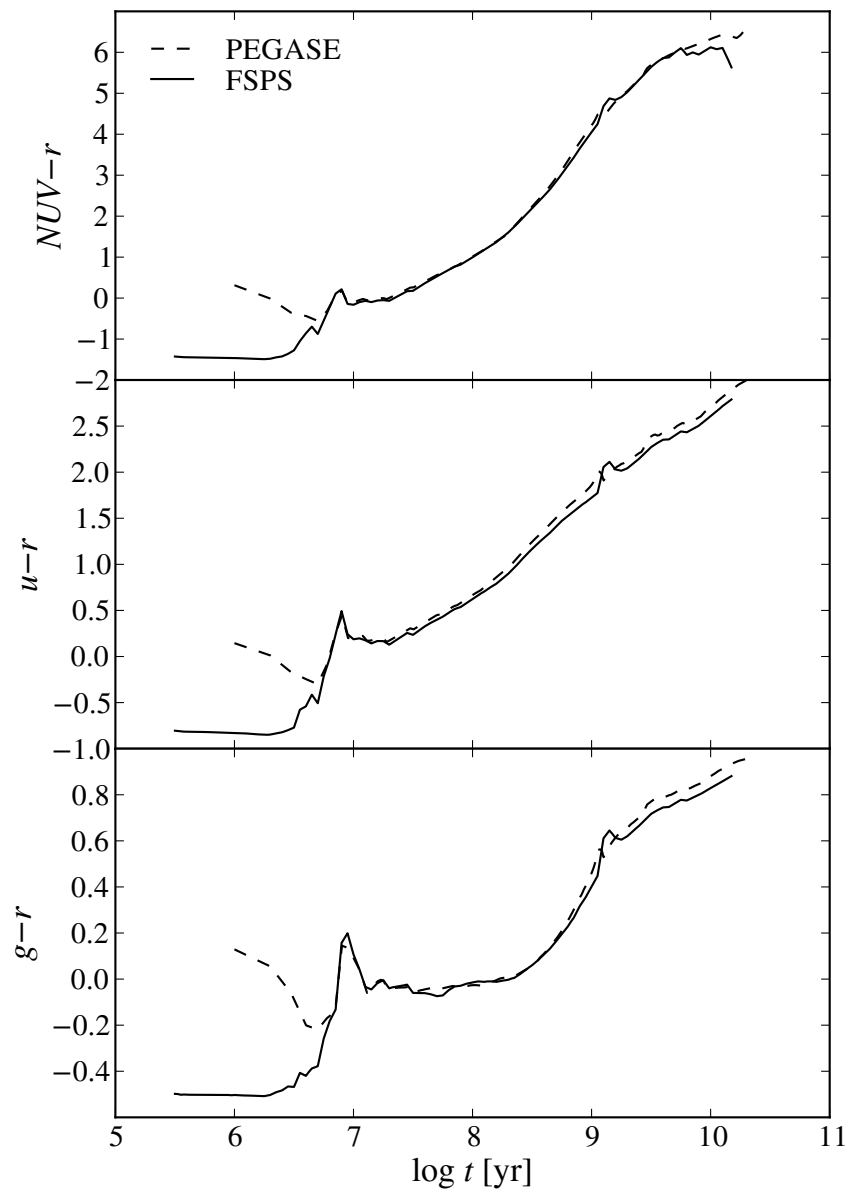
Figure 3.13 FSPS and PEGASE.2 colour predictions as a function of age for a SSP.

one order of magnitude (see Fig. 3.6). This variation is diluted in the composite sSNR and the net effect is similar to an offset in the composite sSNR caused by the offset in the sSNR from the old population. From this, we should expect that a younger old population presents a slightly higher SNR compared to older old populations. This trend is observed in Fig. 3.6.

The net effect of the variations in the fraction of the stars on the extended horizontal branch is to simply offset the age–colour relation, because all the galaxies are assumed to exhibit the same fraction of EHB stars (for instance, the conclusion would likely be different if a bias of EHB stars were to be found towards bluer galaxies). The offset in the age–colour relation vanishes when the $\Delta(colour)$ is computed. Hence, this parameter is less relevant in our model, and the predictions for an extreme fraction of EHB stars, $f_{EHB} = 0.5$, are consistent with the predictions for $f_{EHB} = 0$.

3.8   Model summary

This chapter has explained how we built our model that correlates the SNR to the colour of a given galaxy. The first step was to model these galaxies as a combination of a young burst with mass fraction α on top of an old burst with age 10 Gyr. The age–colour relation was computed and offset with respect to the colour of the old population. The second step was to derive the composite sSNR as a function of time for diverse DTD's. The specific SNR per unit flux was then obtained by multiplying the sSNR by the $M_T/L_\star$ ratio. The final step was to combine the age–sSNR and age–colour relations to eliminate the time dependence. The model is robust against variations in a number of FSPS parameters, such as metallicity, fraction of stars on the EHB, fiducial age of the old population and IMF.
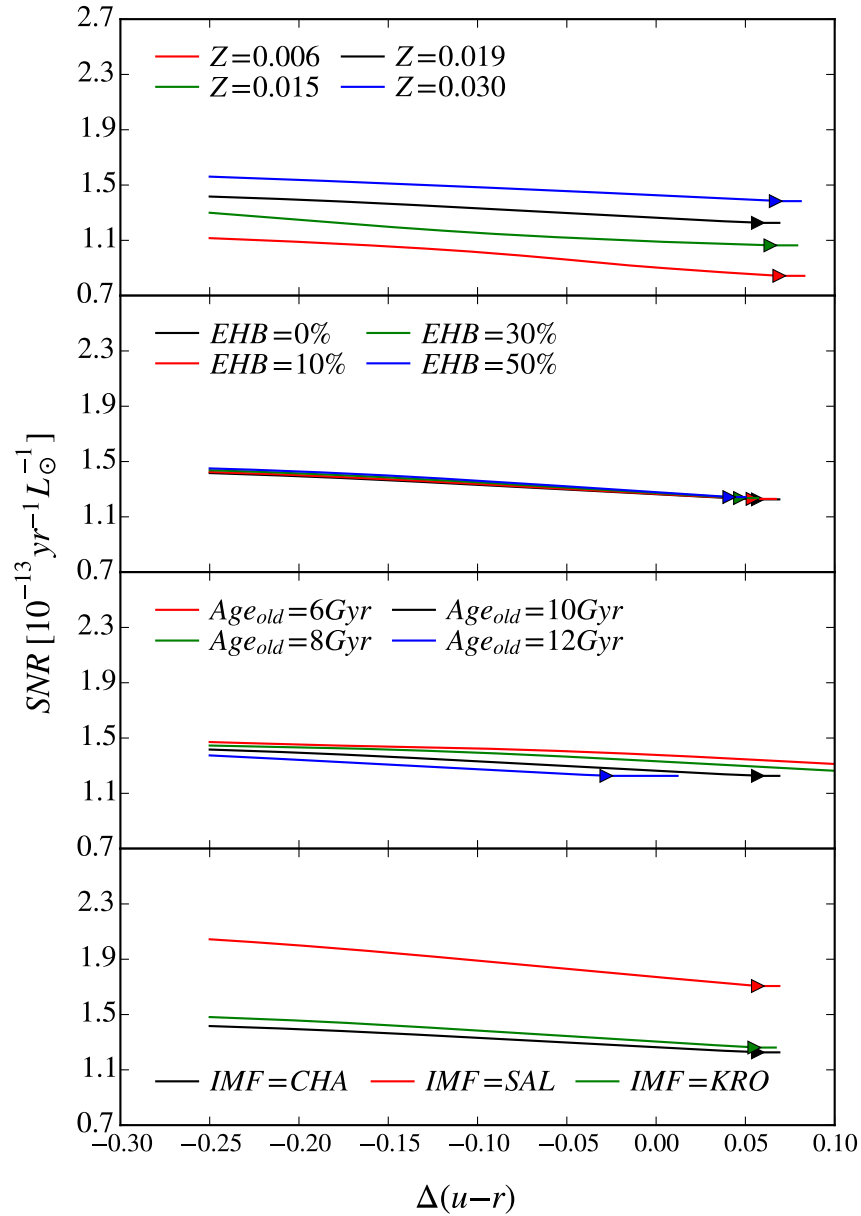
Figure 3.14 Comparison between the $\Delta(colour)$-SNR relations for different FSPS parameters. The black curves corresponds to our standard model, which assume a metallicity of Z=0.019, EHB=0, 10 Gyr old population and Chabrier IMF. Each parameter is varied separately, with the others kept at the standard model values. The sSNR$_L$ at colours redder than the colour demarcated by right triangles is assumed to be constant.

Chapter 4

Results

4.1 General Usage of the Colour-SNR Model

We explain here how to apply the $\Delta(colour)$–sSNR$_L$ model that was described in §3 to our data samples that were characterized in §2.

For a particular data sample, to be analyzed in a given colour, we convert the $\Delta(colour)$ of a galaxy, Δ_i, to a SNR per solar luminosity, $r(\Delta_i)$, via the relations presented in §3.7. We then calculate an absolute SNR value, $R(\Delta_i)$, by multiplying the sSNR$_L$ by the observed flux, $R(\Delta_i) = r(\Delta_i) \cdot f_i$. The flux f_i is computed via Eqn. 3.5 using absolute k-corrected r magnitudes, so that it is consistent with the fluxes used to derive the $M_T/L_\star$ relations in §3.5.

After calculating the $R(\Delta_i)$ value for all galaxies in the sample of interest, we compute the smoothed cumulative distribution of $R(\Delta_i)$ in Δ space. The smoothing procedure is to attribute a normal distribution to the SNR of each galaxy:

$$\tilde{R}(\Delta) = R(\Delta_i) \cdot \frac{1}{2\pi\sigma^2} \cdot e^{\frac{(\Delta - \Delta_i)^2}{2\sigma^2}}, \tag{4.1}$$

where $\tilde{R}(\Delta)$ is the smoothed absolute SNR function of a given galaxy and σ is the standard deviation, for which we use the standard deviation of the RS fit of the sample. The σ values are colour dependent and are shown in Table 2.2.

Although only the galaxies that satisfy $\Delta_{GV} \leq \Delta \leq 2\sigma_{RS}$ are accepted in our samples (see §2.7), the chosen binning range is somewhat larger so that the above Gaussian convolution can be computed. For this purpose we expand the binning range by 1σ on both ends. The width of the bin is set so that 16 bins are computed. The approximate adopted values are shown in Table 4.1.

Table 4.1 Bin parameters.

Sample	$\Delta(color)$	Binning range	Bin width
Main sample			
MENeaCS	$\Delta(g-r)$	$[-0.16, 0.12]$	0.0175
SDSS	$\Delta(g-r)$	$[-0.16, 0.12]$	0.0175
	$\Delta(u-r)$	$[-0.45, 0.6]$	0.066
GALEX+SDSS	$\Delta(NUV-r)$	$[-1.35, 1.05]$	0.15
Supplementary sample			
MENeaCS	$\Delta(g-r)$	$[-0.44, 0.12]$	0.035
SDSS	$\Delta(g-r)$	$[-0.44, 0.12]$	0.035
	$\Delta(u-r)$	$[-1.2, 0.6]$	0.11
GALEX+SDSS	$\Delta(NUV-r)$	$[-4.16, 1.08]$	0.328

For each bin j, defined by $\Delta_j \leq \Delta < \Delta_{j+1}$, we compute the histogram $H_j(\Delta)$ of the smoothed absolute SNR:

$$H_j = \sum_{i=1}^{N} \int_{\Delta_j}^{\Delta_{j+1}} \tilde{R}_i(\Delta)d\Delta, \qquad (4.2)$$

where N is the number of galaxies in the sample. This smoothed histogram is then normalized, so that the sum of all absolute SNR's is unity:

$$h_j = \frac{H_j}{\sum_{j=1}^{J} H_j}, \qquad (4.3)$$

where J is the number of bins.

Finally, the cumulative absolute SNR in each bin, C_j, is computed via:

$$C_j = \sum_{j'=1}^{j} h_{j'}. \qquad (4.4)$$

The observational curves are treated in a similar way, with the exceptions that we deal with the subsample of host galaxies, and each SNR is simply 1, i.e. $R(\Delta_i) = 1$. Also, the σ used in the smoothing procedure is $\sqrt{X_{err,i}^2 + Y_{err,i}^2}$, where $X_{err,i}$ and $Y_{err,i}$ are the uncertainties in the magnitudes employed to compute the colour.

4.2   The Main and Supplementary Analyses

We apply the $\Delta(colour)$–sSNR$_L$ model to the "green valley" (main) and supplementary samples defined in §2.7. The supplementary samples contain objects bluer than the green valley colour and for this reason it is likely that non-early type galaxies are included. As discussed in §3.3, our 2-burst population models should, in principle, be applicable only to early type galaxies. However, the derived colour–SNR relation is remarkably flat for DTD's that are relevant for the double-degenerate channel, i.e. $-1/-1$ and $-0.5/-1$. This particular characteristic holds not only for colours redder than the green-valley, but is also true for significantly bluer colours. For instance, we found the green valley colour to be ~ -0.12 in $\Delta(g-r)$ for both the MENeaCS and SDSS samples, but the colour–sSNR$_L$ relation remains flat (within a factor of 2) for colours as blue as -0.4 (see Fig. 3.12), which is more than 3 times larger than the green-valley threshold and about 10 times larger than the sigma of the RS

(~ 0.04). Note that even SFH's that are more relevant for late type galaxies, such as an exponential starburst with 3 Gyr timescale, do not vary by more than one order of magnitude.

4.3   The Two-Sample Kolmogorov–Smirnov Test

We use the two-sample Kolmogorov–Smirnov (hereafter K-S; Chakravarti et al. 1967) test to compute at which level the prediction from a given DTD can be rejected. This method can be used to quantify the likelihood of the the assumption that two cumulative curves are drawn from the same underlying distribution.

The confidence levels provided, however, are not sensitive to systematic errors nor to the robustness of the assumptions of our model. Therefore, the values computed by the K-S test should be simply seen as probabilities derived from the maximum separation of the observed and predicted curves, and should be treated with caution.

Given two cumulative distributions, $F_{1,n}$ and $F_{2,n'}$, computed from samples containing n and n' objects, respectively, the maximum difference between the two distributions at a given point is calculated as:

$$D_{n,n'} = \sup_x |F_{2,n'}(x) - F_{1,n}(x)|, \tag{4.5}$$

and the rejection level is then inferred from:

$$c(\delta) < D_{n,n'} \cdot \sqrt{\frac{nn'}{n + n'}}, \tag{4.6}$$

where $c(\delta)$ is related to the rejection level δ by the values shown in Table 4.2. For example, if $c = 1.54$, then the model can be ruled out at the 97.5% confidence level.

Table 4.2 K-S test conversion table between the C parameter and the rejection level δ.

δ	0.10	0.05	0.025	0.01	0.005	0.001
$C(\delta)$	1.22	1.36	1.48	1.63	1.73	1.95

4.4   The MENeaCS Sample

The MENeaCS sample consists of galaxies in rich X-ray clusters and therefore should be predominantly populated by early type galaxies. For this reason, we expect the results from this sample to be the most reliable. For the main sample, containing objects redder than the green valley only, Figs. 4.1 and 4.2 show the comparison between the observational curve and the model prediction for each of the DTD's. The better agreement occurs for the DTD's that are representative of the double degenerate scenario channel, i.e. $-0.5/-1$ and $-1/-1$. The predicted curves from the $-1/-2$ and $-1.5/-1.5$ cases are similar and fall short of the observational curve. The catastrophic cutoff case, $-1/-\infty$, exhibits the worst agreement among the DTD's that were tested. The $-0.5/-1$, $-1/-1$ and $-1.5/-1.5$ prediction curves derived for the supplementary sample are shown in Fig. 4.3, while the $-1.5/-1.5$ and $-1/-\infty$ cases are omitted. The latter is ruled out at 99.5% confidence level according to the K-S test. The comments made for the main sample are also pertinent to the supplementary sample.

4.5   The SDSS sample

While the MENeaCS sample is a good representative of the cluster environment, the SDSS sample includes mainly field objects. A field sample is more susceptible to contamination from late type galaxies, for which our model may not be applicable. Nevertheless, this contamination should be less significant for objects redder than the green valley (main sample). Moreover, as discussed in §4.2, the model prediction for SFH's relevant for late-type galaxies are not very different than the predictions based on SFH's relevant for early-type galaxies.

4.5.1   The (g-r) Analysis

The $\Delta(g-r)$ range used for the SDSS sample analysis is practically identical to the range used for the MENeaCS sample (true for both the main and supplementary samples). This is because both the SDSS and MENeaCS main samples are observed to have similar standard deviation for the RS (~ 0.04) and our colour ranges are defined using this parameter.

Figs. 4.4 and 4.5 show the comparison between the observational curve with the
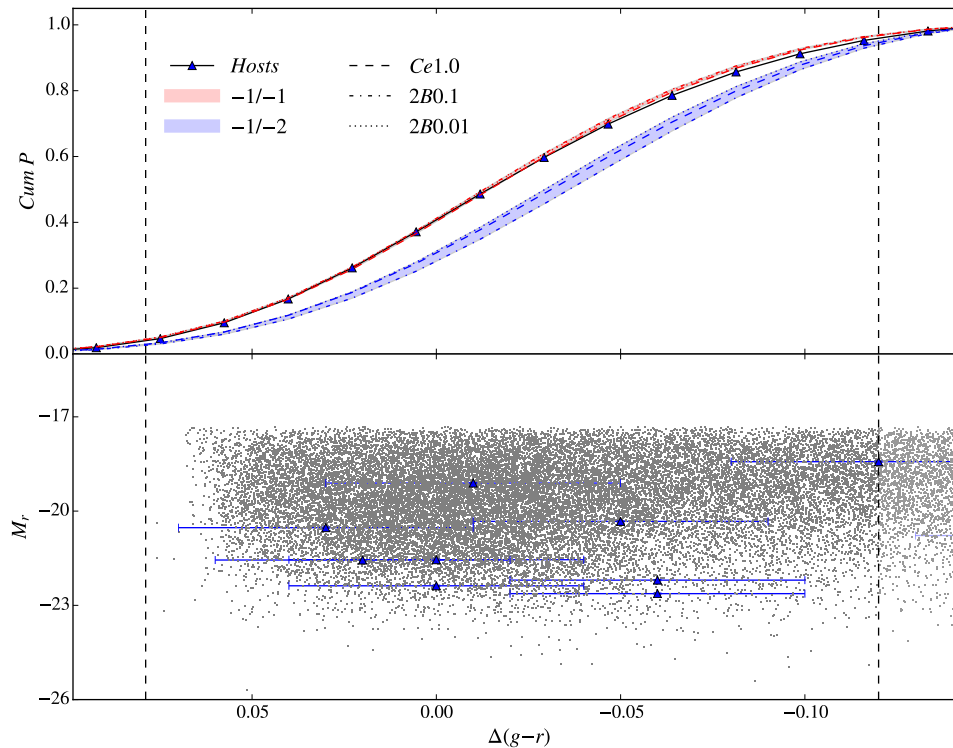
Figure 4.1 Comparison between the predictions from the $\Delta(g - r)$–sSNR$_L$ model and observations for the main MENeaCS sample. The galaxies in the sample under consideration are shown in the bottom plot. We use our models to attributed a supernova rate to each galaxy. These rates are used to compute the predictions shown in the top panel. All the curves are cumulative, normalized and smoothed. The colour in the top plot is coded to indicate a given DTD, and the filled region spans the minimum and maximum predicted values. The different SFH's are coded by line styles: dashed corresponds to the exponential SFH with 1 Gyr timescale, dash-dotted and dotted corresponds to the double-burst with mass fractions of 10% and 1% respectively.
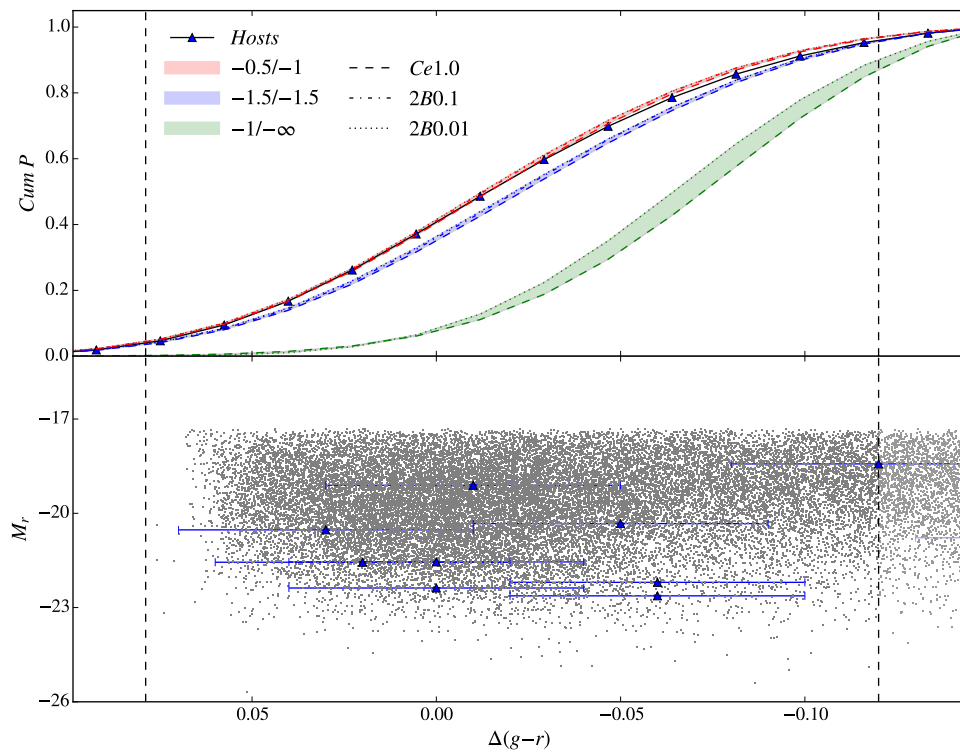
Figure 4.2 Same as Fig. 4.1, but for a different set of DTD's. The prediction of the $-1/-\infty$ DTD combined with the 2B0.1 SFH is null in this colour range.
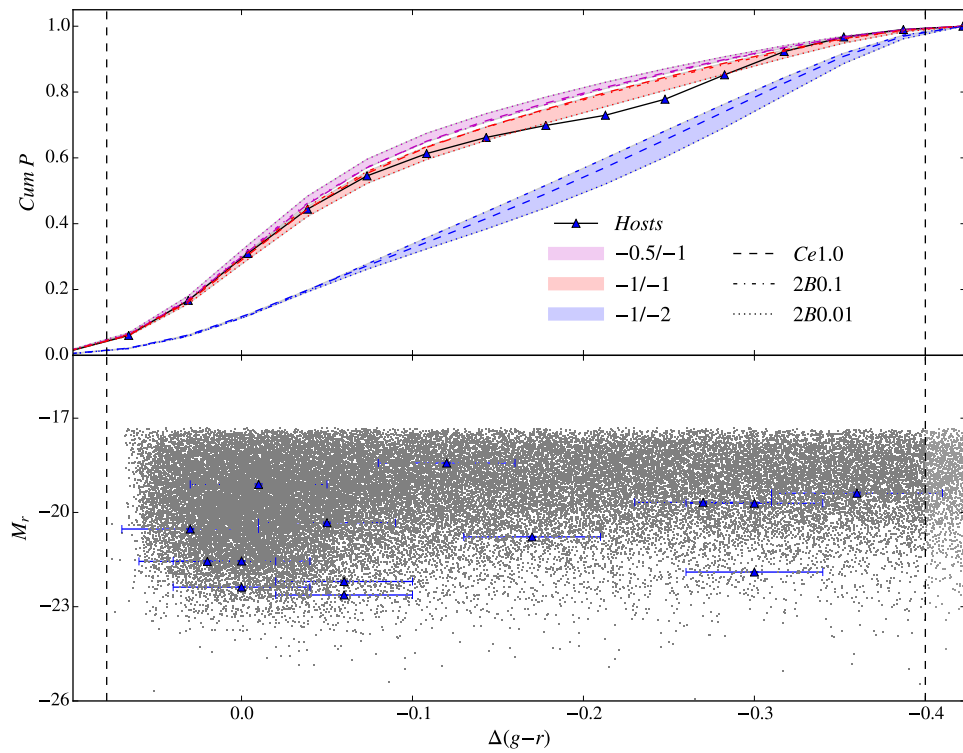
Figure 4.3 Same as Fig. 4.1, but for the supplementary sample.

model prediction for each of the DTD's that we discuss. As for the MENeaCS sample, better agreement occurs for the DTD's ($-0.5/-1$ and $-1/-1$) that are representative of the double degenerate scenario. The predictions derived employing the $-1/-2$ and $-1.5/-1.5$ DTD's are similar and fall short of the observational curve in most of the $\Delta(colour)$ range. The latter cases, however, show a slightly better agreement with the observational curve for $\Delta(colour) > 0$. The $-1/-\infty$ DTD is rejected at the 99.9% confidence level.

Fig. 4.6 shows the prediction curves for the $-0.5/-1$, $-1/-1$ and $-1/-2$ DTD's applied to the supplementary sample. Again, the $-1.5/-1.5$ case is similar to the $-1/-2$ DTD and the $-1/-\infty$ case is the most discrepant scenario. None of the employed DTD's closely match the observational curve and this might indicate that more than one channel is relevant in this sample. The $-1/-\infty$ DTD is again rejected at the 99.9% confidence level.

4.5.2 The (u-r) analysis

The $(u-r)$ colour is expected to be more sensitive to the presence of young populations, mainly because the u filter probes shorter wavelengths than the g filter. Young stars have stronger UV emission relative to old stars and therefore a better contrast should be obtained by measuring $u-r$. However, the magnitude uncertainty is, on average, larger in the u filter, causing part of the data sample to be excluded by the criterion that $u_{err} \leq 0.2$ (see §2.3.2). Moreover, in the $u-r$ colour, the standard deviation of the RS is comparable to the green valley limit, meaning that the double-burst assumption becomes less robust. This is because the colour variations probed can be due either to the presence of a young burst, or to other factors that cause the broadening of the RS, such as metallicity variations.

Both the analysis of the main (Figs. 4.7 and 4.8) and the supplementary samples (Fig. 4.9) corroborate the results of the $\Delta(g-r)$ analysis of the MENeaCS and SDSS samples, i.e. the DTD's $-0.5/-1$ and $-1/-1$, are in better agreement with the observations. Also, the predictions from the $-1.5/-1.5$ and $-1/-2$ DTD's are similar and the $-1/-\infty$ case severely underpredicts the number of supernovae at the red end. Note, however, that the agreement in the supplementary sample, while clear, is less strong than the agreement found in the main sample. The discrepancy occurs at $\Delta(u-r) \sim -0.7$, where the observations fall in between the double degenerate DTD's and the $-1/-2$ case. No DTD tested can be ruled out at a high confidence
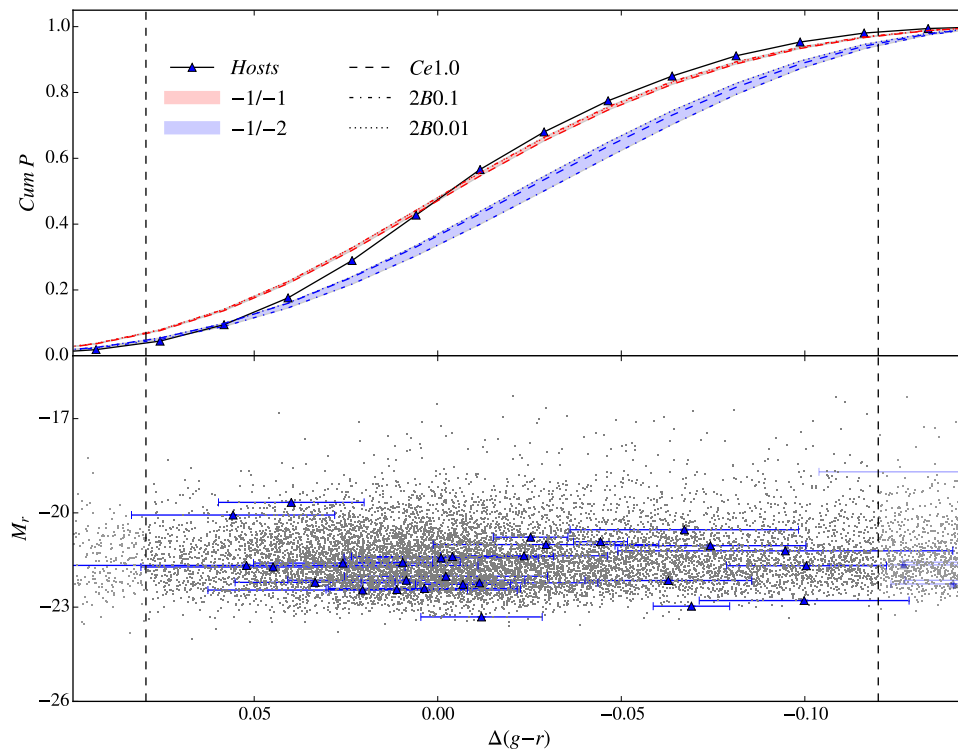
Figure 4.4 Comparison between the predictions from the $\Delta(g-r)$–sSNR$_L$ model and observations for the main SDSS sample. All the curves are cumulative, normalized and smoothed. The colour in the top plot is coded to indicate a given DTD, and the filled region spans the minimum and maximum predicted values. The different SFH's are coded by line styles: dashed corresponds to the exponential SFH with 1 Gyr timescale, dash-dotted and dotted corresponds to the double-burst with mass fractions of 10% and 1% respectively.
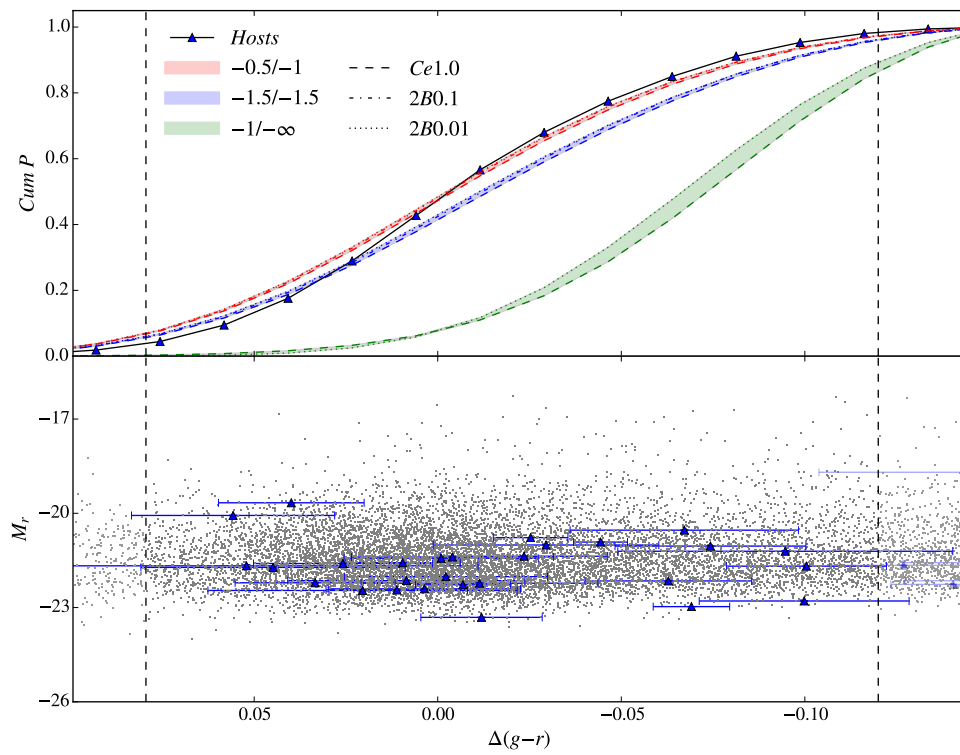
Figure 4.5 Same as Fig. 4.4, but for a different set of DTD's. The prediction of the $-1/-\infty$ DTD combined with the 2B0.1 SFH is null in this colour range.
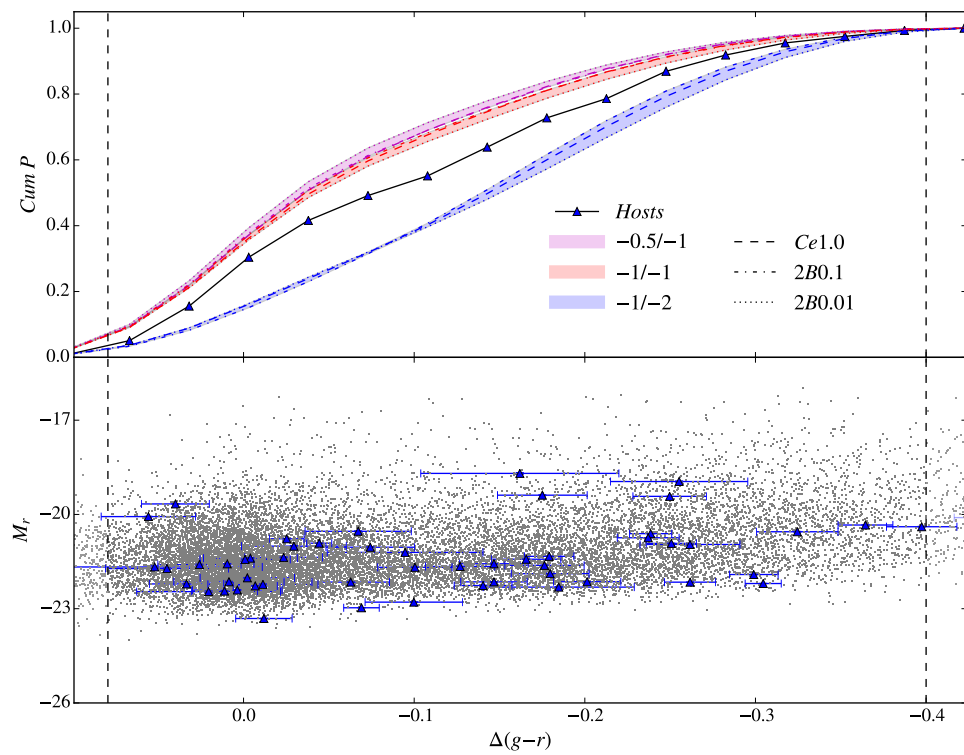
Figure 4.6 Same as Fig. 4.4, but for the supplementary sample.
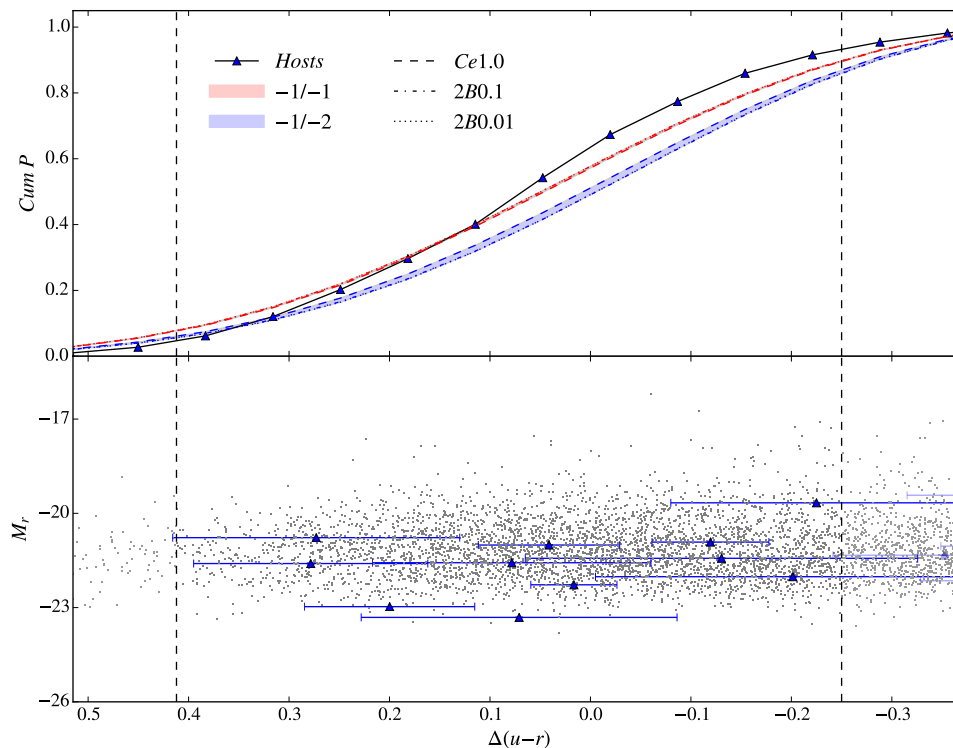
Figure 4.7 Comparison between the predictions from the $\Delta(u-r)$–sSNR$_L$ model and observations for the main SDSS sample. All the curves are cumulative, normalized and smoothed. The colour in the top plot is coded to indicate a given DTD, and the filled region spans the minimum and maximum predicted values for the SFH. The different SFH's are coded by line styles: dashed corresponds to the exponential SFH with 1 Gyr timescale, dash-dotted and dotted corresponds to the double-burst with mass fractions of 10% and 1% respectively.

level based on the K-S test.

4.6 The GALEX+SDSS sample

The $NUV - r$ colour can be measured by matching GALEX and SDSS photometry; of the colours we have used, this colour is the most sensitive colour to residual young populations (see Kaviraj et al. 2007; Schawinski 2009). The undesirable side effect of using this colour, however, is that the sample size is much reduced. A large fraction of galaxies that have measurements from SDSS in the r filter do not have an NUV
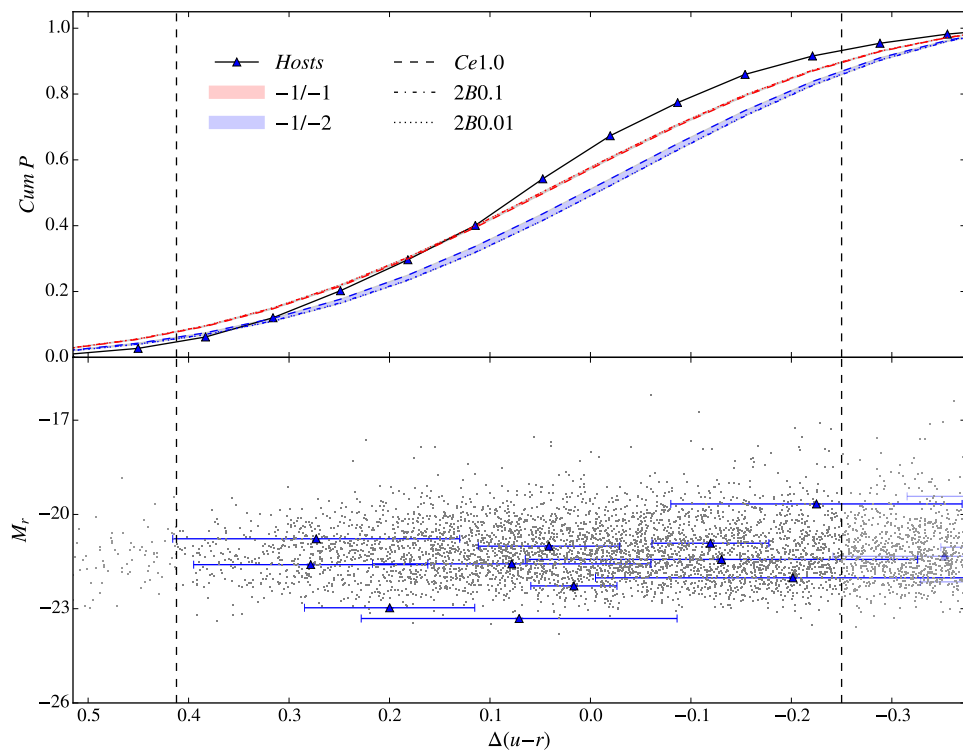
Figure 4.8 Same as Fig. 4.7, but for a different set of DTD's.
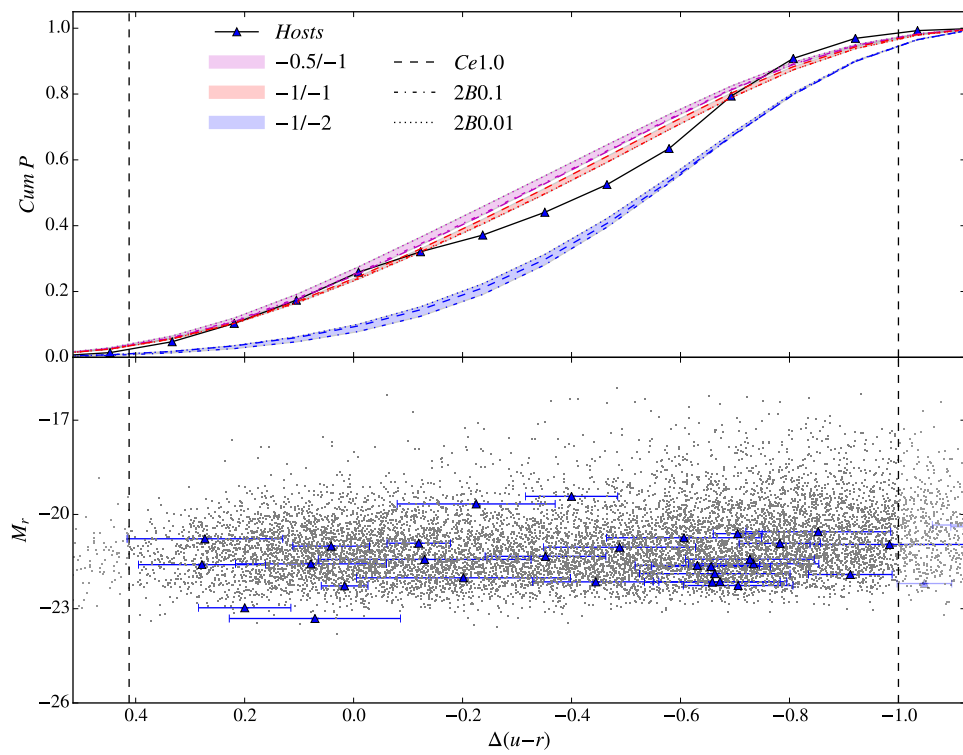
Figure 4.9 Same as Fig. 4.7, but for the supplementary sample.

measurement from GALEX, either because GALEX's resolution is poorer, or because the error in NUV flux is too large. In particular, the RS region is the most affected, since these objects are redder and usually have a very low NUV flux.

We can draw no conclusion from the plots 4.10 and 4.11. There are only 4 hosts that are redder than the green valley and very few galaxies in the sample. Any conclusions would lack statistical significance in this case.

The observational curve derived from the supplementary sample (see Fig. 4.12) exhibits better agreement in most of the colour range with the predictions of the $-0.5/-1$ and $-1/-1$ cases. The only tested mass fraction that allows the $-1/-2$ case to match the observations is 0.1%. Such a small mass fraction can be probed with GALEX data because of the superior sensitivity of the NUV filter to young populations. However, as discussed in the §5, if the observed galaxies possessed RSF with a mass fraction smaller than 1%, very few supernovae would be observed in hosts with $\Delta(g - r) \lesssim -0.2$. (This is because the young population would need to be younger than the formation time of WD's to account for such colour deviations.) This trend is not observed.

4.7   Test Cases

We use the supplementary MENeaCS sample in the $\Delta(g - r)$ colour to compare the predictions of simple toy models with the observations. We employ the supplementary sample simply because possible differences between the original and toy models should be more evident, since the smoothing procedure has less of an effect when applied over a larger $\Delta(colour)$ range. The toy models represent simplified cases to test the relevance of particular assumptions. For example, we consider the following: *(i)* All galaxies in the sample are assumed to have the same $M_T/L_\star$. This is equivalent to saying that the predictions are calculated directly from the sSNR rather than the sSNR$_L$. *(ii)* A constant sSNR$_L$ is used for all objects in the sample. *(iii)* The fiducial age of the RS galaxies is changed to 6 Gyr, 8Gyr and 12 Gyr, but the other parameters of the models remain unaltered. *(iv)* Small errors in the slope of the $-1/-1$ DTD.

Note that the particular values attributed to the assumed constant $M_T/L\star$ and sSNR$_L$ are irrelevant, since the predictions are normalized to match the observed number of supernovae.

The net effect of a constant $M_T/L_\star$ is to decrease the relative SN Ia prediction from the old population (see Fig. 4.13). This happens because a constant mass-
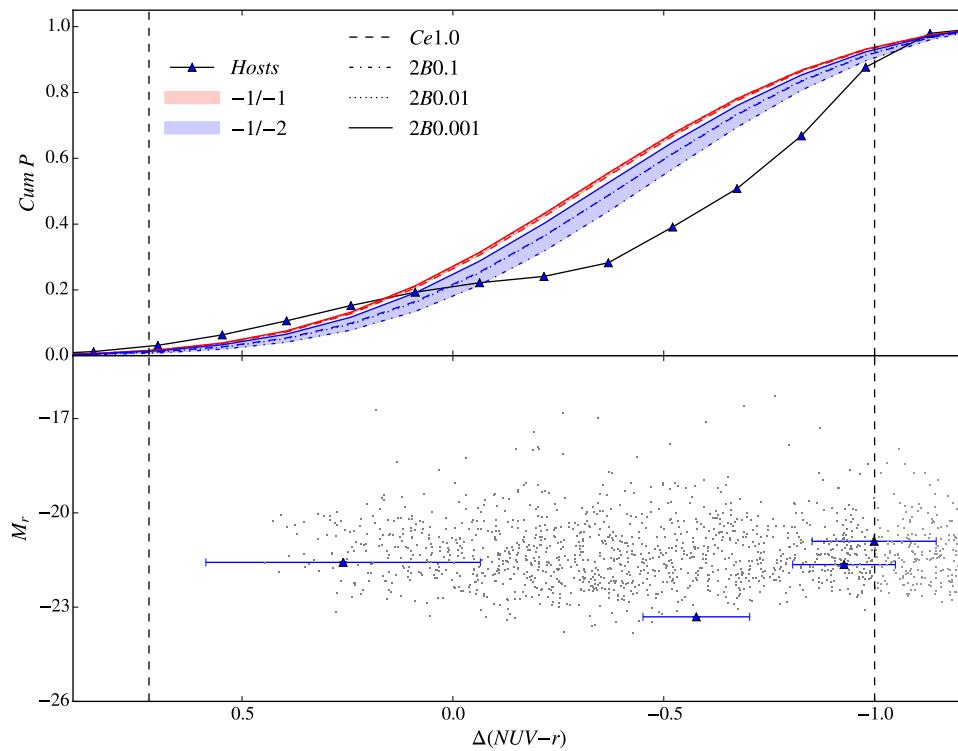
Figure 4.10 Comparison between the predictions from the $\Delta(NUV-r)$–sSNR$_L$ model and observations for the main GALEX+SDSS sample. All the curves are cumulative, normalized and smoothed. The colour in the top plot is coded to indicate a given DTD and the filled region spans the minimum and maximum predicted values. The different SFH's are coded by line styles: dashed corresponds to the exponential SFH with 1 Gyr timescale, dash-dotted and dotted corresponds to the double-burst with mass fractions of 10% and 1% respectively.
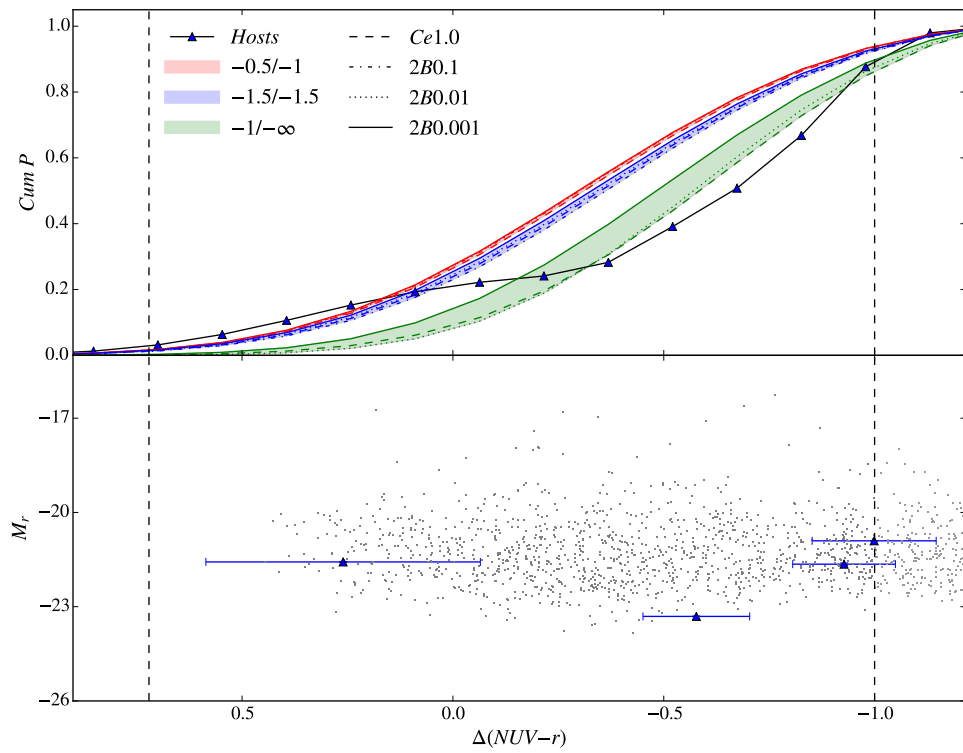
Figure 4.11 Same as Fig. 4.10, but for a different set of DTD's.
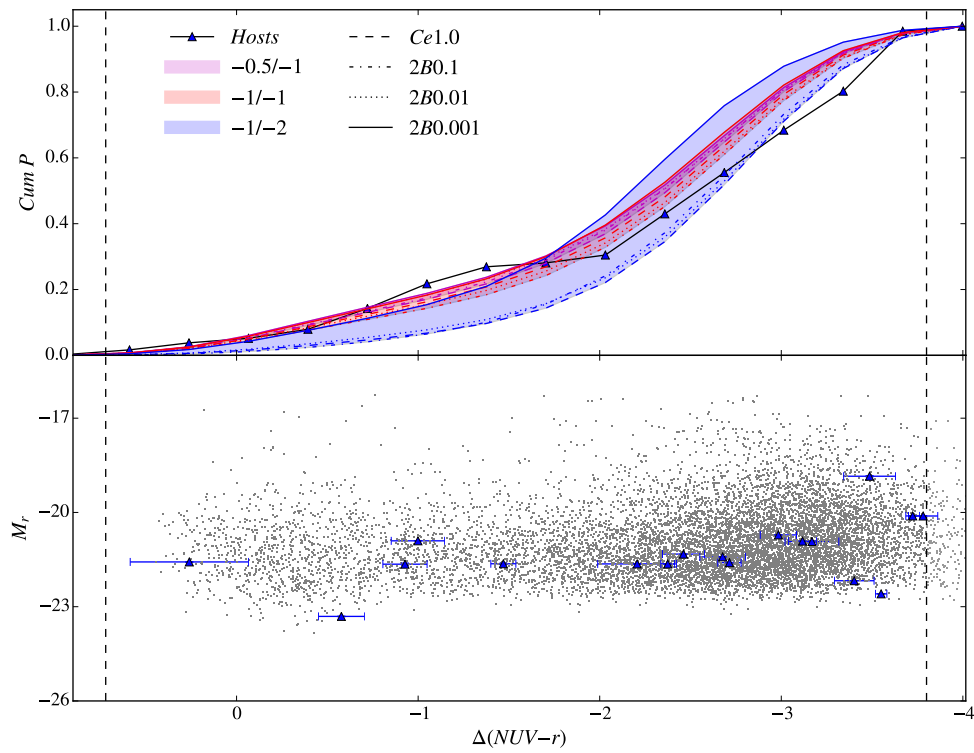
Figure 4.12 Same as Fig. 4.10, but for the supplementary sample.

to-light ratio ignores the tendency of redder galaxies to be more massive; a constant $M_T/L_\star$ therefore underpredicts the number of SN Ia from red galaxies relative to blue galaxies. Also note that the predictions from different SFH's separate, since in this case $M_T/L_\star$ does not contribute to the convergence of the sSNR predictions. (See §3.7.)

In the second test case we hold the SNR_L constant, which corresponds to a simplification of the supernova rate predicted from both the $-0.5/-1$ and $-1/-1$ DTD's. Here we employ the main sample, instead of the supplementary one. The results are shown in Fig. 4.14.

Next, we analyze the third test case. While it is clear that decreasing the age of the old population will lead to higher sSNR_L (because the overall contribution from the old population increases), this situation is complicated because the predictions are normalized and a change in the age of the old population also changes the age–colour relations.

Figs. 4.15 – 4.17 show the model predictions for an age of the old population of 6, 8 and 12 Gyr. The largest discrepancy occurs for the 1% mass fraction, combined with the $-1/-2$ DTD. This happens because of the break caused by the 40 Myr cutoff coming into the range of interest and causing the SNR_L to drop by approximately one order of magnitude. This break is outside the -0.4 to 0 $\Delta(g-r)$ range for the 12 Gyr model, and occurs at ~ -0.35 and ~ -0.30 for the 8 and 6 Gyr parameters, respectively.

Finally we consider the fourth test case. In order to estimate the effect of small errors in the slope of the DTD's, we compare the predictions of the following cases: $-0.8/-0.8$, $-0.9/-0.9$, $-1.0/-1.0$, $-1.1/-1.1$ and $-1.2/-1.2$ (see Fig. 4.18). The predictions of DTD's with slope variations of 0.1 are somewhat similar. However, differences of 0.2 in the slope are sufficient to change significantly the predictions.
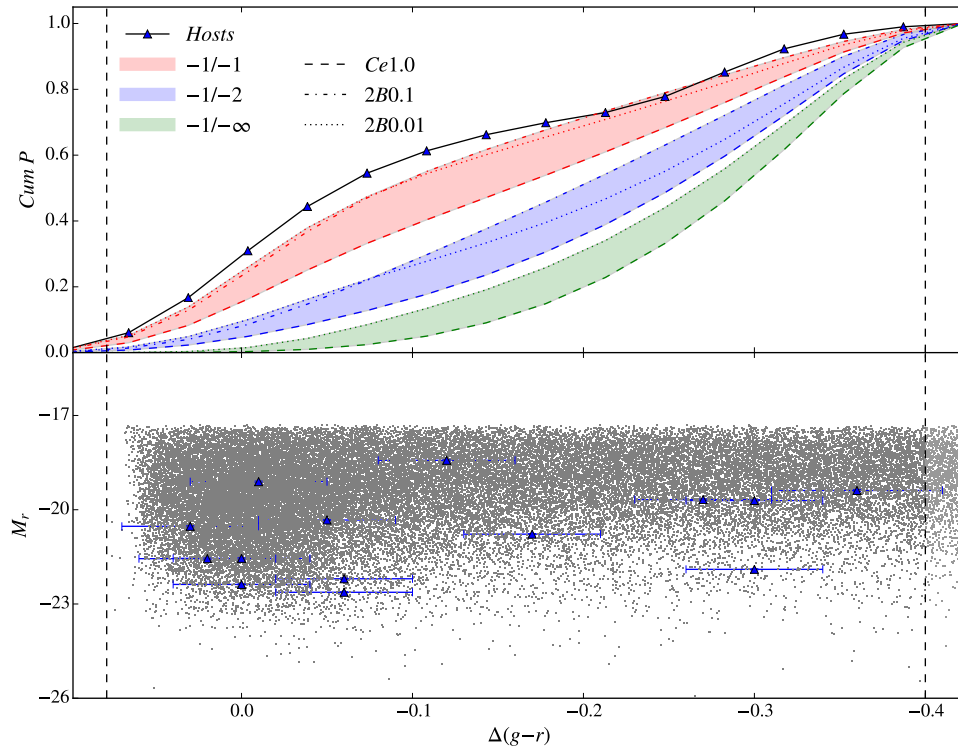
Figure 4.13 Predictions of the $\Delta(g - r)$–sSNR$_L$ model, under the assumption that $M_T/L\star$ is constant. The observations are from the supplementary MENeaCS sample. All the curves are cumulative, normalized and smoothed. The colour in the top plot is coded to indicate a given DTD, and the filled region spans the minimum and maximum predicted values. The different SFH's are coded by line styles: dashed corresponds to the exponential SFH with 1 Gyr timescale, dash-dotted and dotted corresponds to the double-burst with mass fractions of 10% and 1% respectively. The prediction of the $-1/-\infty$ DTD combined with the 2B0.1 SFH is omitted for clarity.
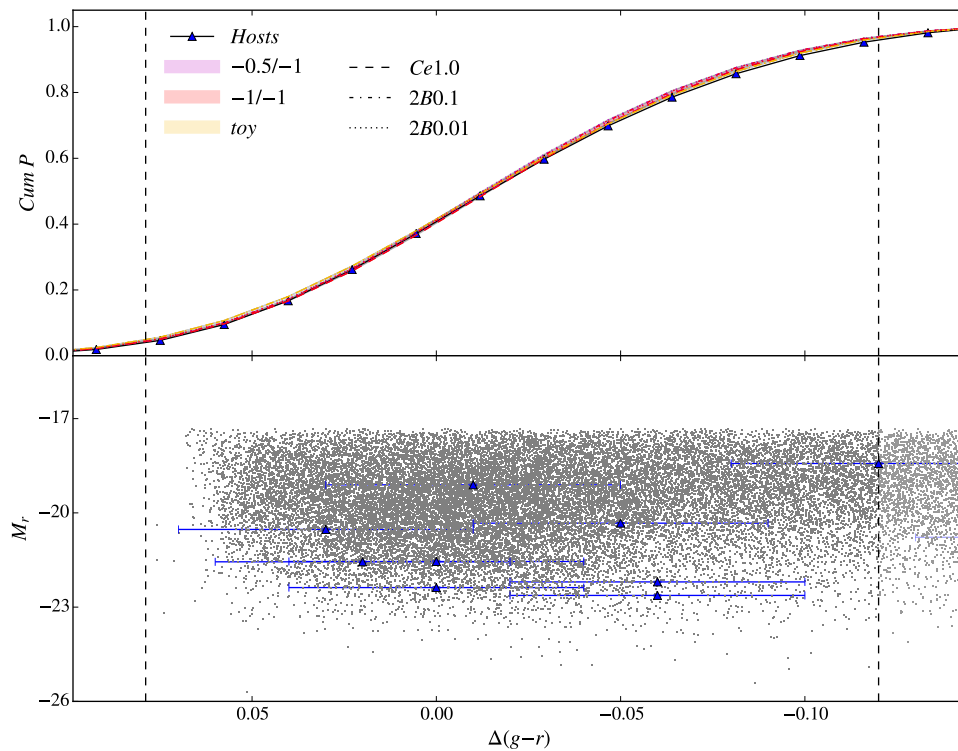
Figure 4.14 Predictions of the $\Delta(g-r)$–sSNR$_L$ model, under the assumption that the sSNR$_L$ is constant. The observations are from the main MENeaCS sample. All the curves are cumulative, normalized and smoothed. The colour in the top plot is coded to indicate a given DTD, and the filled region spans the minimum and maximum predicted values. The different SFH's are coded by line styles: dashed corresponds to the exponential SFH with 1 Gyr timescale, dash-dotted and dotted corresponds to the double-burst with mass fractions of 10% and 1% respectively.
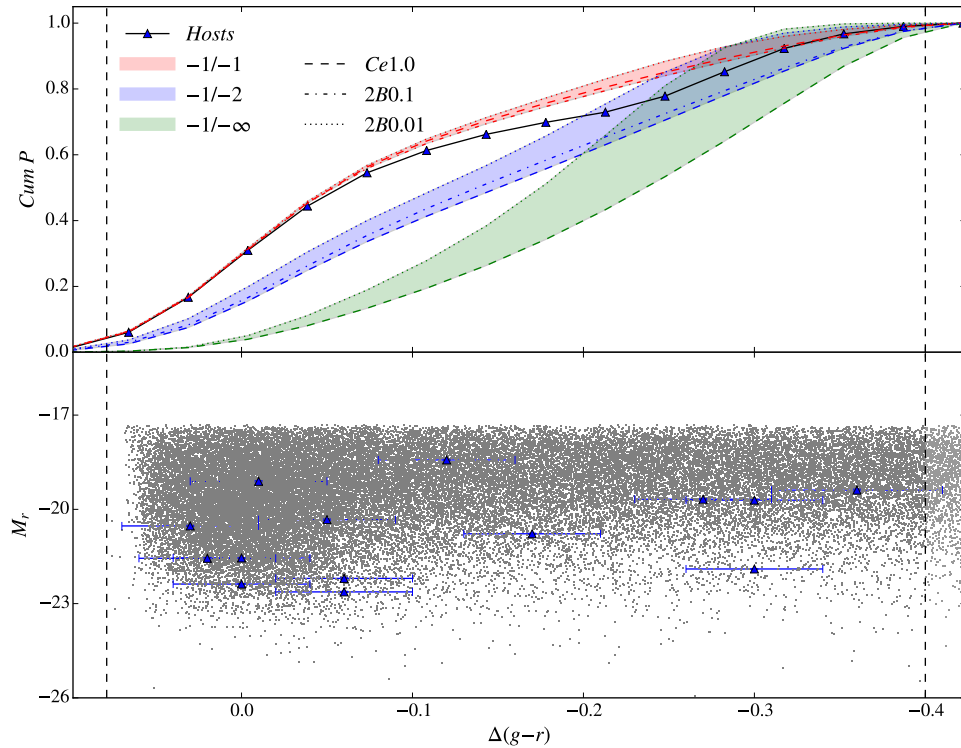
Figure 4.15 Predictions of the $\Delta(g - r)$–sSNR$_L$ model, under the assumption that the fiducial age of the old population is 6 Gyr. The observations are from the main MENeaCS sample. All the curves are cumulative, normalized and smoothed. The colour in the top plot is coded to indicate a given DTD, and the filled region spans the minimum and maximum predicted values. The different SFH's are coded by line styles: dashed corresponds to the exponential SFH with 1 Gyr timescale, dash-dotted and dotted corresponds to the double-burst with mass fractions of 10% and 1% respectively. The prediction of the $-1/-\infty$ DTD combined with the 2B0.1 SFH is omitted for clarity.
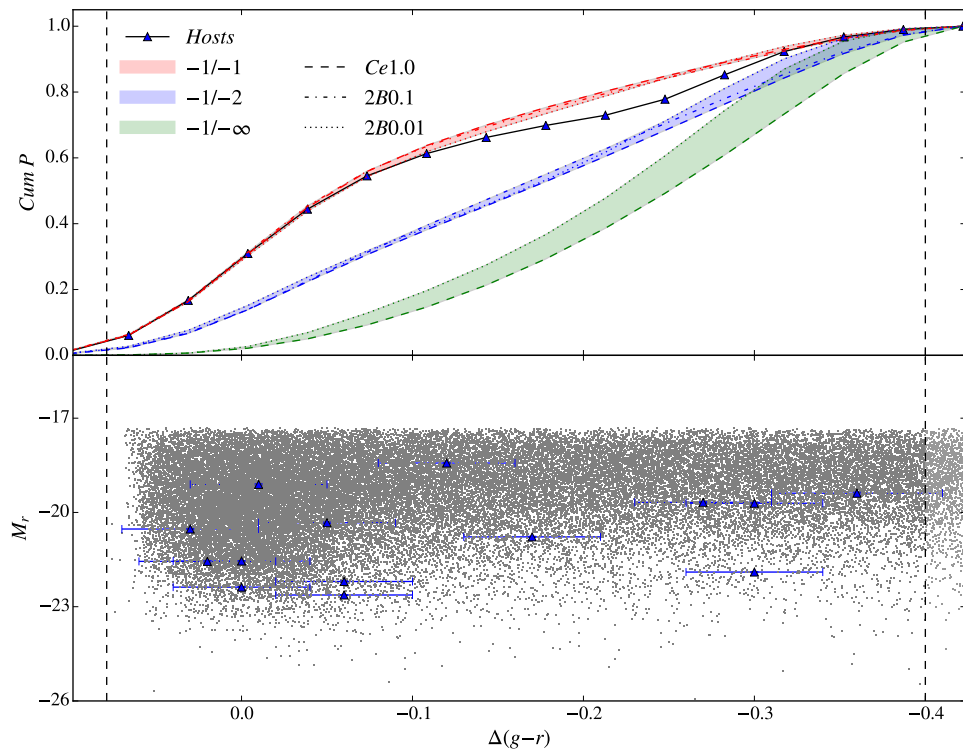
Figure 4.16 Same as Fig. 4.15, but for fiducial age of the old population of 8 Gyr.
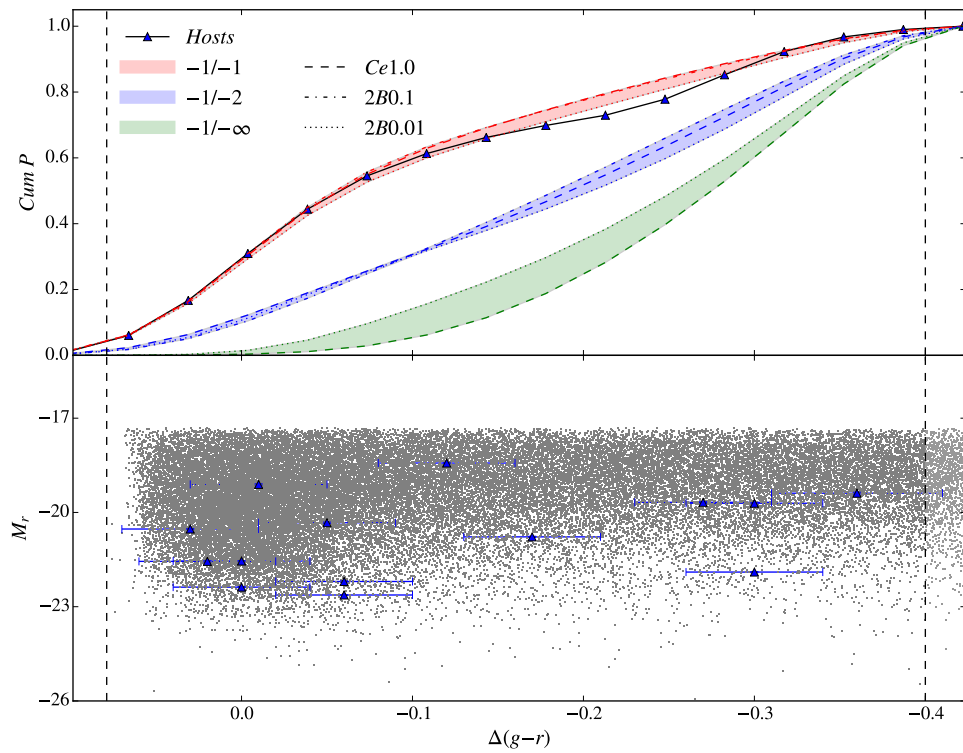
Figure 4.17 Same as Fig. 4.15, but for fiducial age of the old population of 12 Gyr.
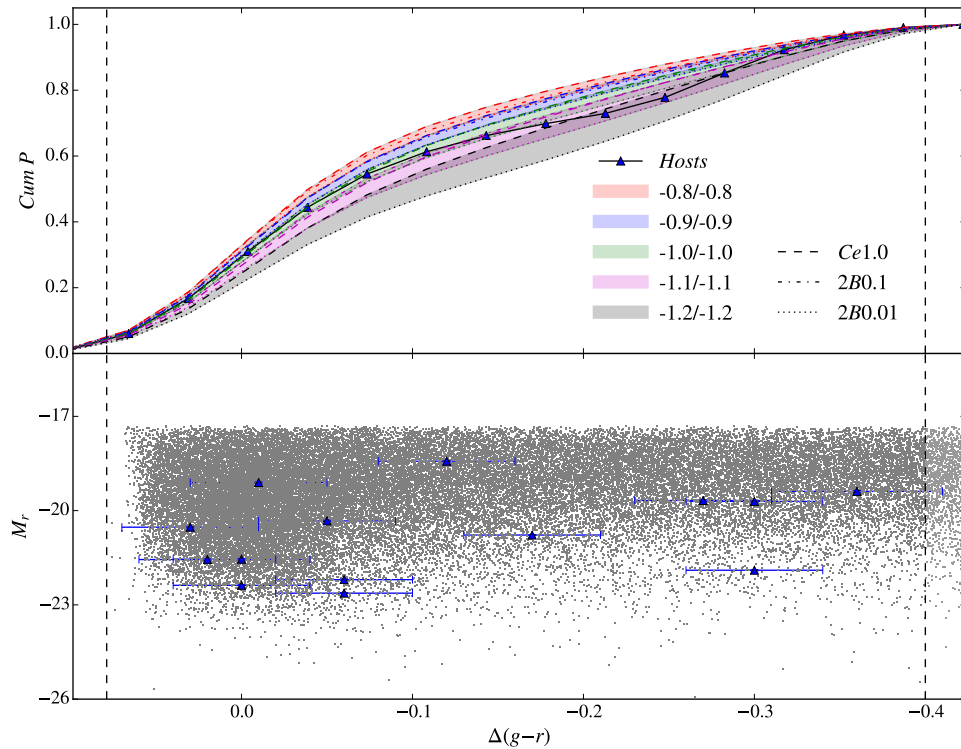
Figure 4.18 Effect of small errors in the slope of the $-1/-1$ DTD. No cutoff is assumed at 1 Gyr and the prediction and observational curves are calculated for the MENeaCS supplementary subsample. All the curves are cumulative, normalized and smoothed. The colour in the top plot is coded to indicate a given DTD, and the filled region spans the minimum and maximum predicted values for the SFH. The different SFH's are coded by line styles: dashed corresponds to the exponential SFH with 1 Gyr timescale, dash-dotted and dotted corresponds to the double-burst with mass fractions of 10% and 1% respectively.

Chapter 5

Discussion and Summary

The results presented in §4 indicate that a DTD without a cutoff at 1-2 Gyr is preferred to match the observations of SNe Ia in colour space. A good fit to most of the data is obtained with a DTD $\propto t^{-1}$. Based on our current (limited) understanding of how different SN Ia channels should influence the shape of their DTD's, we concluded that our results favour the DD scenario.

Our results indicate that a single DTD is sufficient to explain the observed occurrence of SN Ia (except for the SDSS supplementary sample analyzed in $\Delta(g - r)$; see §4.5.1). This is not surprising, given that one progenitor system might be dominant over the others. For instance, if all *normal* SNe Ia originated from the same channel, then $\sim 75\%$ of the observed SNe Ia have a common progenitor system (see Fig. 1.7). This fraction increases to $\gtrsim 85\%$ if, in fact, the regularity of the SN Ia light curves are associated with a single channel. In this case, not only the normal subclass, but also the 1991T-like (and possibly the 1991bg-like) subclass(es) is(are) related to the same channel. In either case, the contribution of the DTD of the less frequent channel would be small.

While our results suggest that the DD channel dominates, this does not mean that the DD scenario is the *only* SN Ia channel. The presence of small numbers of SNe Ia with a completely different DTD could easily go undetected.

We emphasize that the presented probabilities, based on the K-S test, do not take into account systematic errors which ideally would need to be quantified. For example, internal dust reddening can strongly affect the $NUV - r$ colour and yet we ignored this effect. In addition, the treatment of observational uncertainties was quite simplistic. In any case, the predictions of the DTD's that possess: *(i)* a soft or no cutoff, *(ii)* a strong cutoff or *(iii)* a catastrophic cutoff, are well separated. Thus,

the confrontation of these predictions with the data provides a reliable clue as to the progenitor system.

It is well-known that SNe Ia explode in all types of galaxies, including early-type galaxies (Maoz et al., 2014). Schawinski (2009) showed that some early-type galaxies host RSF, and demonstrated that the SD channel could not be ruled out for SNe Ia in these galaxies. In our work, we have used the composite supernova rate from both the young and old populations to show that a DTD $\propto t^{-1}$ is preferred, thus supporting the DD scenario as the dominant SN Ia channel in early-type galaxies. The assumption that all observed SNe would be from the residual young population is unrealistic, given the numbers of SNe observed in RS galaxies.

Our conclusion that SNe Ia are dominated by DD events depends on whether there is a cutoff in the DTD for the SD scenario. This cutoff is predicted from constraints on the mass of the donor (see §3.6.1). However, the findings of Moe & Di Stefano (2015) challenge this picture by introducing a new class of binaries with extreme mass ratios, potentially leading to more SD SNe Ia at longer delay times. This is because the more massive star would quickly evolve into a CO-WD, but the low mass secondary would stay in the MS (or subgiant) phase for several Gyr's before the mass transfer process starts. A modified DTD including these binaries is yet to be computed, and it is unclear if its expected shape past 1-2 Gyr should be a t^{-1} power law. Nevertheless, the possible existence of these binaries could affect our conclusions.

Resorting to the "standard" picture of the SD channel, we tested two DTD's with a cutoff at 1 Gyr. Considering first the *optimistic* $-1/-2$ case, we note that this DTD still allows the SD channel to produce SNe Ia at long delay times, but at a lower rate. Yet this DTD fails to reproduce the observed rates of SNe Ia. Furthermore, the constraints on the mass of both the primary and donor should lead to a stronger cutoff, such as the $-1/-\infty$ case, which completely fails to match the observations. In particular, the $-1/-\infty$ case, combined with the 10% mass fraction parameter as shown in Fig 3.11, predicts zero SNe in the range $-0.12 < g - r < 0$, since the young population would need to be older than 1 Gyr. This prediction is in absolute disagreement with the observed SNe in colour space. In essence, the occurrence of SNe Ia in galaxies that belong to the red sequence locus indicates that the observed DTD cannot possess a strong cutoff [1].

One concern in this thesis could be the possible presence of young populations with mass fractions smaller than 1%, to which our models are not sensitive. The

---

[1]But note that a soft cutoff, as in the $-0.5/-1$ case, is in agreement with the observations.

presence of such RSF will not change our conclusions because: *(i)* If the DD channel is dominant, then the old population also hosts supernovae and the contribution from a young population with such small mass fraction is likely to be negligible. *(ii)* If the SD channel is dominant, then a young population with a small mass fraction could explain the supernovae observed in the RS locus. This is because the young population would not affect the red colour of the underlying old population, and would be able to host supernovae. However, galaxies observed to have $\Delta(g-r) \lesssim -0.2$ would indicate that the age of this young population is $\lesssim 10$ Myr (see Fig. 3.2). In this case neither the old population nor the young population would be able to host SNe Ia. Thus, a clear cut in the observational curves should be observed in the MENeaCS and SDSS supplementary subsamples. This is not observed.

We checked the underlying assumption of our analysis that galaxies in the red sequence possess roughly the same age in both field and cluster environments. To this end, we selected 35 MENeaCS clusters that were in the SDSS footprint, and extracted data for a 4 deg^2 area centred on each cluster. We separated the galaxies in these regions into cluster and field, based on their radial distance from the cluster centroid. The peak of the red sequence occurs nearly at the same colour for the two groups, thus suggesting that the assumption of RS galaxies possessing the same age in either environment is realistic.

Could the treatment of colour degeneracy affect our results? We have chosen to linearly interpolate the sSNR$_L$ at the reddest degenerate colour[2] with the sSNR$_L$ at $\Delta(colour) = 0$. We further assume that the sSNR$_L$ remains constant at colours redder than the RS. If we instead assume a constant sSNR$_L$ for colours redder than the reddest degenerate colour, the conclusions remain unchanged. The models shown in Fig. 3.12, where no treatment is necessary for colour degeneracies, corroborate this claim.

We have interpreted our results only in terms of the SD and DD scenarios; the DTD's of other channels have not yet been extensively calculated. For the core degenerate channel, in which a WD merges with the core of an AGB star, a SN Ia might result during or shortly after the common-envelope phase (Livio & Riess, 2003). If this is the case, Ilkov & Soker (2013) claim that the CD scenario would be able to explain SNe Ia only in star forming galaxies. Ilkov & Soker (2012), on the other hand, propose that the SN Ia explosion event might be delayed because of the effects

---

[2]Meaning that the age of the young population cannot be inferred if the observed colour is redder than this limit.

of rapid rotation. In this case, the time delay necessary to spin down the object via magneto-dipole radiation would allow populations as old as 10 Gyr to host SNe Ia. Nevertheless, the shape of this DTD is not yet known; it would be surprising if a t^{-1} power law (as for the DD channel) were found, given the different nature of the delay-time mechanism.

Ruiter et al. (2011) investigated the DTD of the sub-Chandrasekhar double detonation channel and concluded that it has two distinct components. The first part exhibits short delay times ($\lesssim$500 Myr) and is derived from the case where the donor is a non-degenerate He-star (resembling the SD scenario). The second component includes long delay times, from $\sim$1 Gyr to one Hubble time, and is derived from the case where the donor is a He-WD (resembling the DD scenario). Thus, as this model stands in between the SD and DD channels, the corresponding DTD shows the behavior expected from both scenarios. However, the predicted DTD shape of the double detonation channel is closer to a power law with -2 index for $t \gtrsim 1$ Gyr. This does not agree with our results.

The quark-nova model would exhibit a DTD similar to the DD channel, since the timescale for the WD to approach its NS companion is governed by gravitational waves. This model should be analyzed with caution, however, given the number of uncertainties involved. In the pycnonuclear context, Chiosi et al. (2015) point out that the delay time can be as low as a few tens of thousand years after the formation of the WD, but longer times are not discussed. This scenario seems to contradict the lack of prompt SNe Ia (Schawinski, 2009; Anderson et al., 2015), since WD's start forming at ages as short as $\sim$40 Myr.

Another result of our work is that the DTD for the DD channel exhibits a nearly constant sSNR$_L$ in colour space, irrespective of assumed mass fraction; this is also true for an exponential SFH with a wide-range of timescales, for more complicated SFH's involving infall, and for mixtures of these SFH's with pure bursts (Pritchet, private communication). This result was not expected *a priori*, and is the result of a fine balance between age, colour and mass-to-light ratio. We have used this result to verify that the DTD that best matches the observational curves does not have a strong cutoff.

Under the implicit assumption that one progenitor channel is dominant over the others, the derived model can be employed to test if a proposed DTD is in agreement with the observed rate of SN Ia. However, the model cannot probe small errors in the DTD slopes. For instance, the predictions of a DTD like $-1.1/-1.1$ cannot be

distinguished from the $-1/-1$ case. We also remark that two distinct DTD's can have similar predictions. This is true for the cases $-1/-2$ and $-1.5/-1.5$ and for $-0.5/-1$ and $-1/-1$.

In summary, we have derived relations between sSNR$_L$ and colour deviation from the red sequence for five distinct delay time distributions. By comparing the predicted cumulative and smoothed curves with the observations, we have concluded that the $-1/-1$ and $-0.5/-1$ cases provide the best agreement. This result is supportive of the DD channel.

Follow-up research should primarily focus on improving the statistical significance of our results. Larger control and host samples would allow a better contrast between the different delay time distributions. For example, relaxing the spectroscopic redshift requirement for the SDSS samples would increase the number of supernovae by an order of magnitude. Photometric redshifts, however, are less reliable and might significantly distort the k-corrections. This would change the $\Delta(colour)$ distribution, affecting the attributed supernova rates and artificially increase the colour spread of the RS, thus diminishing the reliability of the results.

Another option is to apply our method to surveys that probe SNe Ia at higher redshifts ($0.2 \lesssim z \lesssim 1.0$), such as the Supernova Legacy Survey (SNLS; e.g. Conley et al. 2011 and Sullivan et al. 2011). Although spectroscopic redshift is not available for all galaxies in the targeted fields, the large number of detected SNe Ia can be used further test our models.

Larger SN samples would also allow the search for correlations between SN Ia subclasses and the $\Delta(colour)$ parameter. Of particular interest is the light curve stretch factor and its apparent dependence on the star forming properties of host galaxies (e.g. Lampeitl et al. 2010 and Smith et al. 2012). Is it possible that a division of the sample by stretch would indicate two (or more) different DTD's, indicative of different progenitor systems?

Further investigation and compilation of the DTD's expected for each proposed SN Ia channel would help to elucidate the progenitor puzzle. For instance, the expected delay times of the core degenerate scenario are still being actively discussed in the literature. Moreover, the DTD's predicted for the SD channel are in severe disagreement, as shown in Fig. 3.5, from Maoz et al. (2014). For a given channel, the discrepant DTD features that are predicted make it difficult to find definitive evidence of the progenitor system based on a single method.

It is of great interest to test a modified DTD for the SD channel that would

account for the new class of binaries proposed by Moe & Di Stefano (2015). If this new DTD predicts a shallower power law index (or similar function) at old ages, then it might strengthen the case for the SD scenario in old stellar populations and early-type galaxies. Direct evidence supportive of the existence of these binaries would help to establish such systems as potential progenitors of SNe Ia.

Finally, we plan to investigate the applicability of the colour–$sSNR_L$ relation to more complex SFH's and include other parameters, such as internal dust reddening, in its formulation. This would allow one to fully utilize the colour range of SN Ia hosts, consequently enlarging the control and host samples.

Bibliography

Abazajian, K. N. et al. 2009, Astrophysical Journal, Supplement Series, 182, 543

Anderson, J. P., James, P. A., Förster, F., González-Gaitán, S., Habergham, S. M., Hamuy, M., & Lyman, J. D. 2015, Monthly Notices of the RAS, 448, 732

Aznar-Siguán, G., García-Berro, E., Lorén-Aguilar, P., Soker, N., & Kashi, A. 2015, Monthly Notices of the RAS, 450, 2948

Baldry, I. K., Glazebrook, K., Brinkmann, J., Ivezić, Ž., Lupton, R. H., Nichol, R. C., & Szalay, A. S. 2004, Astrophysical Journal, 600, 681

Bianchi, L., Efremova, B., Herald, J., Girardi, L., Zabot, A., Marigo, P., & Martin, C. 2011, Monthly Notices of the RAS, 411, 2770

Blanton, M. R. & Roweis, S. 2007, Astronomical Journal, 133, 734

Bloom, J. S. et al. 2012, Astrophysical Journal, Letters to the Editor, 744, L17

Bours, M. C. P., Toonen, S., & Nelemans, G. 2013, Astronomy and Astrophysics, 552, A24

Branch, D. & Miller, D. L. 1993, Astrophysical Journal, Letters to the Editor, 405, L5

Branch, D. & Tammann, G. A. 1992, Annual Review of Astronomy and Astrophysics, 30, 359

Bruzual, G. & Charlot, S. 2003, Monthly Notices of the RAS, 344, 1000

Buzzoni, A. 2002, Astronomical Journal, 123, 1188

Cadonau, R. 1986, PhD thesis, , Univ. of Basel, (1986)

Cao, Y. et al. 2015, Nature, 521, 328

Chabrier, G. 2003, Publications of the ASP, 115, 763

Chakravarti, I., Laha, R., & Roy, J. 1967, Handbook of methods of applied statistics, Wiley series in probability and mathematical statistics No. v. 1 (Wiley)

Chandrasekhar, S. 1931, Astrophysical Journal, 74, 81

Chiosi, C. & Carraro, G. 2002, Monthly Notices of the RAS, 335, 335

Chiosi, E., Chiosi, C., Trevisan, P., Piovan, L., & Orio, M. 2015, Monthly Notices of the RAS, 448, 2100

Claeys, J. S. W., Pols, O. R., Izzard, R. G., Vink, J., & Verbunt, F. W. M. 2014, Astronomy and Astrophysics, 563, A83

Conley, A. et al. 2011, Astrophysical Journal, Supplement Series, 192, 1

Conroy, C. & Gunn, J. E. 2010, Astrophysical Journal, 712, 833

Conroy, C., Gunn, J. E., & White, M. 2009, Astrophysical Journal, 699, 486

Conroy, C., White, M., & Gunn, J. E. 2010, Astrophysical Journal, 708, 58

Di Stefano, R. 2010, Astrophysical Journal, 712, 728

Falcón-Barroso, J., Sánchez-Blázquez, P., Vazdekis, A., Ricciardelli, E., Cardiel, N., Cenarro, A. J., Gorgas, J., & Peletier, R. F. 2011, Astronomy and Astrophysics, 532, A95

Ferreras, I., Cayon, L., Martinez-Gonzalez, E., & Benitez, N. 1999, Monthly Notices of the RAS, 304, 319

Ferreras, I. & Silk, J. 2000, Astrophysical Journal, Letters to the Editor, 541, L37

Filippenko, A. V. 1997, Annual Review of Astronomy and Astrophysics, 35, 309

Filippenko, A. V. et al. 1992, Astrophysical Journal, Letters to the Editor, 384, L15

Fink, M., Hillebrandt, W., & Röpke, F. K. 2007, Astronomy and Astrophysics, 476, 1133

Fink, M., Röpke, F. K., Hillebrandt, W., Seitenzahl, I. R., Sim, S. A., & Kromer, M. 2010, Astronomy and Astrophysics, 514, A53

Fioc, M. & Rocca-Volmerange, B. 1997, Astronomy and Astrophysics, 326, 950

— 1999, ArXiv Astrophysics e-prints

Fisher, R. & Jumper, K. 2015, Astrophysical Journal, 805, 150

Foley, R. J. et al. 2012, Astronomical Journal, 143, 113

Frieman, J. A. et al. 2008, Astronomical Journal, 135, 338

Fukugita, M., Ichikawa, T., Gunn, J. E., Doi, M., Shimasaku, K., & Schneider, D. P. 1996, Astronomical Journal, 111, 1748

Gao, Y. & Pritchet, C. 2013, Astronomical Journal, 145, 83

González-Gaitán, S. et al. 2014, Astrophysical Journal, 795, 142

Graur, O. & Maoz, D. 2013, Monthly Notices of the RAS, 430, 1746

Graur, O. et al. 2014, Astrophysical Journal, 783, 28

Graves, G. J., Faber, S. M., & Schiavon, R. P. 2009, Astrophysical Journal, 693, 486

Greggio, L. 2005, Astronomy and Astrophysics, 441, 1055

Guy, J. et al. 2007, Astronomy and Astrophysics, 466, 11

Hachisu, I., Kato, M., & Nomoto, K. 1999, Astrophysical Journal, 522, 487

— 2010, Astrophysical Journal, Letters to the Editor, 724, L212

Hachisu, I., Kato, M., & Saio, H. 1989, Astrophysical Journal, Letters to the Editor, 342, L19

Hamuy, M., Phillips, M. M., Maza, J., Suntzeff, N. B., Schommer, R. A., & Aviles, R. 1995, Astronomical Journal, 109, 1

Han, Z. & Podsiadlowski, P. 2004, Monthly Notices of the RAS, 350, 1301

Harrison, E. R. 1964, Proceedings of the Physical Society, 84, 213

Hatton, S., Devriendt, J. E. G., Ninin, S., Bouchet, F. R., Guiderdoni, B., & Vibert, D. 2003, Monthly Notices of the RAS, 343, 75

Hayden, B. T. et al. 2010a, Astrophysical Journal, 722, 1691

— 2010b, Astrophysical Journal, 712, 350

Heger, A., Fryer, C. L., Woosley, S. E., Langer, N., & Hartmann, D. H. 2003, Astrophysical Journal, 591, 288

Hogg, D. W. et al. 2004, Astrophysical Journal, Letters to the Editor, 601, L29

Howell, D. A. 2011, Nature Communications, 2, 350

Howell, D. A. et al. 2006, Nature, 443, 308

Hoyle, F. & Fowler, W. A. 1960, Astrophysical Journal, 132, 565

Hsiao, Y. C. E. 2009, PhD thesis, University of Victoria, Canada

Ilkov, M. & Soker, N. 2012, Monthly Notices of the RAS, 419, 1695

— 2013, Monthly Notices of the RAS, 428, 579

Itoh, N. 1970, Progress of Theoretical Physics, 44, 291

Iwamoto, K. & Kunugise, T. 2006, in American Institute of Physics Conference Series, Vol. 847, Origin of Matter and Evolution of Galaxies, ed. S. Kubono, W. Aoki, T. Kajino, T. Motobayashi, & K. Nomoto, 406–408

Janka, H.-T. 2012, Annual Review of Nuclear and Particle Science, 62, 407

Jimenez, R., Bernardi, M., Haiman, Z., Panter, B., & Heavens, A. F. 2007, Astrophysical Journal, 669, 947

Kasen, D. 2010, Astrophysical Journal, 708, 1025

Kashi, A. & Soker, N. 2011, Monthly Notices of the RAS, 417, 1466

Kaviraj, S. et al. 2007, Astrophysical Journal, Supplement Series, 173, 619

Kerzendorf, W. E. et al. 2013, Astrophysical Journal, 774, 99

Kroupa, P. 2001, Monthly Notices of the RAS, 322, 231

Kutsuna, M. & Shigeyama, T. 2015, ArXiv e-prints

Lampeitl, H. et al. 2010, Astrophysical Journal, 722, 566

Langer, N., Deutschmann, A., Wellstein, S., & Höflich, P. 2000, Astronomy and Astrophysics, 362, 1046

Le Borgne, D., Rocca-Volmerange, B., Prugniel, P., Lançon, A., Fioc, M., & Soubiran, C. 2004, Astronomy and Astrophysics, 425, 881

Lejeune, T., Cuisinier, F., & Buser, R. 1997, VizieR Online Data Catalog, 412, 50229

— 1998, Astronomy and Astrophysics, Supplement Series, 130, 65

Leonard, D. C. 2007, Astrophysical Journal, 670, 1275

Li, C., de Grijs, R., & Deng, L. 2014, Nature, 516, 367

Li, W. et al. 2003, Publications of the ASP, 115, 453

— 2011, Monthly Notices of the RAS, 412, 1441

Liu, Z. W., Pakmor, R., Röpke, F. K., Edelmann, P., Wang, B., Kromer, M., Hillebrandt, W., & Han, Z. W. 2012, Astronomy and Astrophysics, 548, A2

Livio, M. & Riess, A. G. 2003, Astrophysical Journal, Letters to the Editor, 594, L93

Lorén-Aguilar, P., Isern, J., & García-Berro, E. 2010, Monthly Notices of the RAS, 406, 2749

Lu, F. J., Wang, Q. D., Ge, M. Y., Qu, J. L., Yang, X. J., Zheng, S. J., & Chen, Y. 2011, Astrophysical Journal, 732, 11

Lundqvist, P. et al. 2015, Astronomy and Astrophysics, 577, A39

Mackey, A. D., Broby Nielsen, P., Ferguson, A. M. N., & Richardson, J. C. 2008, Astrophysical Journal, Letters to the Editor, 681, L17

Maeda, K., Kawabata, K., Li, W., Tanaka, M., Mazzali, P. A., Hattori, T., Nomoto, K., & Filippenko, A. V. 2009, Astrophysical Journal, 690, 1745

Maoz, D., Mannucci, F., & Brandt, T. D. 2012, Monthly Notices of the RAS, 426, 3282

Maoz, D., Mannucci, F., Li, W., Filippenko, A. V., Della Valle, M., & Panagia, N. 2011, Monthly Notices of the RAS, 412, 1508

Maoz, D., Mannucci, F., & Nelemans, G. 2014, Annual Review of Astronomy and Astrophysics, 52, 107

Maoz, D., Sharon, K., & Gal-Yam, A. 2010, Astrophysical Journal, 722, 1879

Marigo, P. & Girardi, L. 2007, Astronomy and Astrophysics, 469, 239

Marigo, P., Girardi, L., Bressan, A., Groenewegen, M. A. T., Silva, L., & Granato, G. L. 2008, Astronomy and Astrophysics, 482, 883

Martin, D. C. et al. 2005, Astrophysical Journal, Letters to the Editor, 619, L1

Mazzali, P. A., Nomoto, K., Cappellaro, E., Nakamura, T., Umeda, H., & Iwamoto, K. 2001, Astrophysical Journal, 547, 988

Mennekens, N., Vanbeveren, D., De Greve, J. P., & De Donder, E. 2010, Astronomy and Astrophysics, 515, A89

Milne, P. A., Brown, P. J., Roming, P. W. A., Bufano, F., & Gehrels, N. 2013, Astrophysical Journal, 779, 23

Milone, A. P., Bedin, L. R., Piotto, G., & Anderson, J. 2009, Astronomy and Astrophysics, 497, 755

Moe, M. & Di Stefano, R. 2015, Astrophysical Journal, 801, 113

Neill, J. D. et al. 2009, Astrophysical Journal, 707, 1449

Nomoto, K. 1982a, Astrophysical Journal, 257, 780

— 1982b, Astrophysical Journal, 253, 798

Nomoto, K. 2014, in IAU Symposium, Vol. 296, IAU Symposium, ed. A. Ray & R. A. McCray, 27–36

Nomoto, K., Umeda, H., Kobayashi, C., Hachisu, I., Kato, M., & Tsujimoto, T. 2000, in American Institute of Physics Conference Series, Vol. 522, American Institute of Physics Conference Series, ed. S. S. Holt & W. W. Zhang, 35–52

Nugent, P. E. et al. 2011, Nature, 480, 344

Oke, J. B. & Gunn, J. E. 1983, Astrophysical Journal, 266, 713

Ouyed, R., Koning, N., Leahy, D., Staff, J. E., & Cassidy, D. T. 2014, Research in Astronomy and Astrophysics, 14, 497

Pakmor, R., Kromer, M., Taubenberger, S., Sim, S. A., Röpke, F. K., & Hillebrandt, W. 2012, Astrophysical Journal, Letters to the Editor, 747, L10

Patat, F. et al. 2008, The Messenger, 131, 30

Paxton, B., Bildsten, L., Dotter, A., Herwig, F., Lesaffre, P., & Timmes, F. 2010, MESA: Modules for Experiments in Stellar Astrophysics, Astrophysics Source Code Library

Perlmutter, S. et al. 1997, in Bulletin of the American Astronomical Society, Vol. 29, American Astronomical Society Meeting Abstracts, 1351

Perlmutter, S. et al. 1999, Astrophysical Journal, 517, 565

Petty, S. M. et al. 2013, Astronomical Journal, 146, 77

Phillips, M. M. 1993, Astrophysical Journal, Letters to the Editor, 413, L105

Phillips, M. M., Wells, L. A., Suntzeff, N. B., Hamuy, M., Leibundgut, B., Kirshner, R. P., & Foltz, C. B. 1992, Astronomical Journal, 103, 1632

Pietrinferni, A., Cassisi, S., Salaris, M., & Castelli, F. 2004, Astrophysical Journal, 612, 168

Pimbblet, K. A., Smail, I., Kodama, T., Couch, W. J., Edge, A. C., Zabludoff, A. I., & O'Hely, E. 2002, Monthly Notices of the RAS, 331, 333

Pinto, P. A. & Eastman, R. G. 1996, ArXiv Astrophysics e-prints

Planck Collaboration et al. 2014, Astronomy and Astrophysics, 571, A16

Podsiadlowski, P. 2013, in Planets, Stars and Stellar Systems, ed. T. Oswalt & M. Barstow (Springer Netherlands), 693–733

Poelarends, A. J. T., Herwig, F., Langer, N., & Heger, A. 2008, Astrophysical Journal, 675, 614

Pritchet, C. J., Howell, D. A., & Sullivan, M. 2008, Astrophysical Journal, Letters to the Editor, 683, L25

Ree, C. H., Jeong, H., Oh, K., Chung, C., Lee, J. H., Kim, S. C., & Kyeong, J. 2012, Astrophysical Journal, Letters to the Editor, 744, L10

Ree, C. H. et al. 2007, Astrophysical Journal, Supplement Series, 173, 607

Riess, A. G. et al. 1998, Astronomical Journal, 116, 1009

Riess, A. G., Press, W. H., & Kirshner, R. P. 1996, Astrophysical Journal, 473, 88

Rigault, M. et al. 2015, Astrophysical Journal, 802, 20

Ruiter, A. J., Belczynski, K., & Fryer, C. 2009, Astrophysical Journal, 699, 2026

Ruiter, A. J., Belczynski, K., Sim, S. A., Hillebrandt, W., Fryer, C. L., Fink, M., & Kromer, M. 2011, Monthly Notices of the RAS, 417, 408

Ruiz-Lapuente, P. 2012, Nature, 481, 149

Ruiz-Lapuente, P. et al. 2004, Nature, 431, 1069

Salpeter, E. E. 1955, Astrophysical Journal, 121, 161

Salpeter, E. E. & van Horn, H. M. 1969, Astrophysical Journal, 155, 183

Sand, D. J. et al. 2011, Astrophysical Journal, 729, 142

— 2012, Astrophysical Journal, 746, 163

Schawinski, K. 2009, Monthly Notices of the RAS, 397, 717

Schawinski, K. et al. 2007a, Astrophysical Journal, Supplement Series, 173, 512

Schawinski, K., Thomas, D., Sarzi, M., Maraston, C., Kaviraj, S., Joo, S.-J., Yi, S. K., & Silk, J. 2007b, Monthly Notices of the RAS, 382, 1415

Schlegel, D. J., Finkbeiner, D. P., & Davis, M. 1998, Astrophysical Journal, 500, 525

Shen, K. J., Bildsten, L., Kasen, D., & Quataert, E. 2012, Astrophysical Journal, 748, 35

Shen, K. J., Guillochon, J., & Foley, R. J. 2013, Astrophysical Journal, Letters to the Editor, 770, L35

Smartt, S. J. 2009, Annual Review of Astronomy and Astrophysics, 47, 63

Smartt, S. J., Eldridge, J. J., Crockett, R. M., & Maund, J. R. 2009, Monthly Notices of the RAS, 395, 1409

Smith, M. et al. 2012, Astrophysical Journal, 755, 61

Starrfield, S., Truran, J. W., Sparks, W. M., & Kutter, G. S. 1972, Astrophysical Journal, 176, 169

Strateva, I. et al. 2001, Astronomical Journal, 122, 1861

Sullivan, M. et al. 2011, Astrophysical Journal, 737, 102

— 2006, Astrophysical Journal, 648, 868

Tanaka, M. et al. 2010, Astrophysical Journal, 714, 1209

Totani, T., Morokuma, T., Oda, T., Doi, M., & Yasuda, N. 2008, Publications of the ASJ, 60, 1327

Trager, S. C., Faber, S. M., & Dressler, A. 2008, Monthly Notices of the RAS, 386, 715

Tripp, R. 1998, Astronomy and Astrophysics, 331, 815

Turatto, M. 2003, in Lecture Notes in Physics, Berlin Springer Verlag, Vol. 598, Supernovae and Gamma-Ray Bursters, ed. K. Weiler, 21–36

Tutukov, A. V. & Yungelson, L. R. 1981, Nauchnye Informatsii, 49, 3

van den Heuvel, E. P. J., Bhattacharya, D., Nomoto, K., & Rappaport, S. A. 1992, Astronomy and Astrophysics, 262, 97

van Dokkum, P. G. & Conroy, C. 2010, Nature, 468, 940

van Kerkwijk, M. H., Chang, P., & Justham, S. 2010, Astrophysical Journal, Letters to the Editor, 722, L157

Wang, B., Li, X.-D., & Han, Z.-W. 2010, Monthly Notices of the RAS, 401, 2729

Wang, B., Meng, X., Chen, X., & Han, Z. 2009, Monthly Notices of the RAS, 395, 847

Weiler, K. W. & Sramek, R. A. 1988, Annual Review of Astronomy and Astrophysics, 26, 295

Westera, P., Lejeune, T., Buser, R., Cuisinier, F., & Bruzual, G. 2002, Astronomy and Astrophysics, 381, 524

Whelan, J. & Iben, Jr., I. 1973, Astrophysical Journal, 186, 1007

Wiersma, R. P. C., Schaye, J., & Theuns, T. 2011, Monthly Notices of the RAS, 415, 353

Wyder, T. K. et al. 2007, Astrophysical Journal, Supplement Series, 173, 293

Yi, S. K. et al. 2005, Astrophysical Journal, Letters to the Editor, 619, L111

York, D. G. et al. 2000, Astronomical Journal, 120, 1579

Yuan, H. B., Liu, X. W., & Xiang, M. S. 2013, Monthly Notices of the RAS, 430, 2188

Yungelson, L. R. 2010, Astronomy Letters, 36, 780